Unraveling the Role of TET3 in regulating EndMT in Cardiac Fibrosis

Dissertation
for the award of the degree
"Doctor rerum naturalium" (Dr.rer.nat)
of the Georg-August-Universität Göttingen

within the doctoral program *(Cardiovascular Science)*
of the Georg-August University School of Science (GAUSS)

submitted by
Sabine Maamari

from Tripoli, Lebanon
Göttingen, 2022

Members of the thesis committee

Prof. Dr. med. Elisabeth M. Zeisberg (1st Referee)
Department of Cardiology and Pneumology
University Medical Center Göttingen

PD Dr. Laura Zelarayan (2nd Referee)
Institute of Pharmacology and Toxicology
University Medical Center Göttingen

Prof. Dr. med. Dörthe Katschinski
Institute of Cardiovascular Physiology
University Medical Center, Göttingen

Members of the examination board

Prof. Dr. med. Ralf Dressel
Institute of Cellular and Molecular Immunology
University Medical Center, Göttingen

Prof. Dr. Bernd Wollnik
Institute of Human Genetics
University Medical Center, Göttingen

Prof. Dr. Argyris Papantonis
Institute of Pathology
University Medical Center, Göttingen

I-Affidavit

I hereby declare that my doctoral thesis entitled “Unraveling the Role of TET3 in regulating EndMT in Cardiac Fibrosis” has been written independently with no other sources or aids than quoted.

Sabine Maamari
Göttingen, November 2022

Dedicated to my Family

Fawaz, Najia, Judy, Carine, and Fouad

II-Acknowledgments

I would like to acknowledge and give my warmest thanks to my supervisor Prof. Dr. med Elisabeth Zeisberg, who made this work possible. I am grateful for the trust you have put in me and for giving me the opportunity to share my ideas in an open and safe environment. Your guidance and advice carried me through all the stages of my PhD, as well as my future career choices.

I would also like to thank my thesis committee members Prof. Dr.med Dörthe Katschinski and PD Dr. Laura Zelarayan for their insightful and constructive comments which helped me support and validate my research hypothesis. I am thankful for the IRTG1816 program and for the support we received from Dr. Christina Würtz and Mrs. Fulya Ören.

I would also like to thank all the members from AG Zeisberg who became like a family to me in the last four years. My sincere thanks to Prof. Dr. med Michael Zeisberg, who provided me with valuable feedback and guidance on my project. I am especially grateful to PD Dr. Xingbo Xu and Dr. Gunsmaa Nyamsuren for having my back and guiding me with all technical aspects throughout my project. To all my colleagues and students: Dr. Xiaoying Tan, Afifa, Tousif, Berenice, Carina, Tim, Vishalini, Tony, Rocket, Xin, Max, and Leon, you have made my PhD journey enjoyable, and I am forever grateful for all of you. Finally, this work would not have been possible without the help of our technicians Katrin Schwarze, Annika Erdmann, and Anika Hausdörfer.

Göttingen has become my second home, where I have built friendships that will carry on my whole life. I am extremely grateful to my best friend Alfiia Latfullina, who has always been there for me since day one. I would also like to mention Surahbi, Milica, Misa, and Eduardo for their constant support and faith. To the love of my life Ahmed, I am forever grateful for your kindness, generosity, endless love, and unmatched support every single day for the past two years.

Finally, to my family, and where do I begin? I am blessed to have been surrounded by role models throughout my lifetime: Judy, Sami, Carine, and Fouad. Being the youngest in the family, I was lucky enough to receive immense support from my siblings and parents, regardless of the decision I made. To my dad, Fawaz, thank you for your love and support. I will never forget our hour-long conversations about my research and career choices. Thank you for always pushing me to be the best version of myself. To my mom, Najia, thank you for always checking up on me and having the time to talk to me at any time of the day.

Table of Contents

List of Figures

List of Tables

Abbreviations

Abbreviation	Definition
°C	Degree Celsius
5hmC	5-hydroxymethyl-cytosine
5mC	5-methyl-cytosine
AAV	Adeno-associated virus
ALK5	Activin A receptor type II-like kinase
AngII	Angiotensin II
BMP	Bone morphogenic protein
BPM	Beats per minute
BW	Body weight
Cas9	CRISPR associated protein 9
CD-144	Vascular endothelial cadherin
CD-31	Platelet endothelial cell adhesion molecule
Cdh5	Cadherin 5
cDNA	Complementary DNA
CEBPα	CCAAT/enhancer-binding protein alpha
CF	Cardiac fibroblast
CMV	Cytomegalovirus
Col1A1	Collagen type 1 alpha one
CpG	5'—C—phosphate—G—3
CRISPR	Clustered Regularly Interspaced Short Palindromic Repeats/
CVD	Cardiovascular disease
DAPI	4',6-diamidino-2-phenylindole
ddH_2O	Double-distilled water
dHFCas9	Catalytically dead high-fidelity Cas9
DMEM	Dulbecco's Modified Eagle Medium
DMSO	Dimethyl Sulfoxide
DNA	Deoxyribonucleic acid
DNMT	DNA methyl transferase
DRIP	DNA-RNA immunoprecipitation
DSBH	Double-stranded β-helix domain
DTT	Dithiothreitol
ECM	Extracellular matrix
EDHF	Endothelium derived hyperpolarizing factor
EDTA	Ethylenediaminetetraacetic acid
EF	Ejection fraction
EMSA	Electrophoretic mobility shift assay
EMT	Epithelial to mesenchymal transition
EndMA	Transient endothelial to mesenchymal activation
EndMT	Endothelial to mesenchymal transition
ET-1	Endothelin 1

EtOH	Ethanol
FBS	Fetal Bovine Serum
FLP	Flippase
FRT	Flippase recognition target
FS	Fractional shortening
FSC	Forward Scatter
GADD45g	Growth arrest and DNA-damage-inducible protein gamma
GAP	GTPase activating proteins
GDP	Guanosine diphosphate
GFP	Green Fluorescence Protein
GTP	Guanosine Triphosphate
H3K9ac	Acetylation of lysine 9 on histone H3 protein subunit
HCl	Hydrochloric acid
HDAC	Histone de-acetylase
HE	Hematoxylin and eosin
HEK293	Human embryonic kidney cells 293
HF	High-fidelity
HR	Heart rate
HRP	Horseradish peroxidase
HW	Heart weight
IF	Immunofluorescence
IgG	Immunoglobulin G
IHC	Immunohistochemistry
IP	Immunoprecipitation
kb	Kilobase
KCl	Potassium chloride
kDa	Kilodalton
lncRNA	Long non-coding RNA
loxP	locus of x-over, P1
LVID,d	Left ventricular internal diameter end diastole
LVID,s	Left ventricular internal diameter end systole
LVPW,d	Left ventricular posterior wall thickness at diastole
MAPK4	Mitogen-activated protein kinase kinase kinase kinase
MCEC	Mouse cardiac endothelial cells
MCF	Mouse cardiac fibroblasts
MeCP2	Methyl-CpG binding protein 2
MeDIP	Methylated DNA immunoprecipitation
$MgCl_2$	Magnesium chloride
miRNA	Micro RNA
mRNA	Messenger Ribonucleic acid
MTS	Masson's trichrome stain
MYH6	Myosin Heavy Chain 6
MYH7	Myosin Heavy Chain 7

ncRNA	Non-coding RNA
nM	Nanomolar
NPPA	Natriuretic Peptide A
NPPB	Natriuretic Peptide B
OE	Overexpression
PBS	Phosphate buffered saline
PCR	Polymerase chain reaction
PEG	Polyethylene glycol
PEI	Polyethyleneimine
PGI2	Prostacyclin
piRNAs	Piwi-interacting RNAs
PVDF	Polyvinylidene fluoride
qRT-PCR	Real-Time Quantitative Reverse Transcription PCR
RASAL1	RAS Protein Activator Like 1
RIP	RNA immunoprecipitation
RISC	RNA-induced silencing complex
RNA	Ribonucleic acid
rRNA	Ribosomal RNA
RWT	Relative wall thickness
shRNA	Short hairpin RNA
siRNA	Small interfering RNA
SMAD	Suppressor of Mothers against Decapentaplegic
SSC	Side scatter
TAE	Tris-acetate-EDTA
TARID	TCF21 Antisense RNA Inducing Promoter Demethylation
TAVI	Transcatheter aortic valve implantation
TCF21	Transcription Factor 21
TET	Ten eleven translocation methylcytosine dioxygenase
TGF-b	Transforming growth factor beta
TNF-α	Tumor necrosis factor alpha
tRNA	Transfer ribonucleic acid
TSS	Transcription start site
TXA-2	Thromboxane
UTR	Untranslated region
UUO	Unilateral Ureteral Obstruction
WHO	World health organization
αSMA	Alpha smooth muscle actin
µg	Micrograms
µl	Microliter

Abstract

DNA methylation and subsequent silencing of gene expression is associated with disease states including tumorigenesis and fibrosis. Although DNA methylation is a dynamic and reversible process, the mechanisms of and requirements for reactivation of gene expression via demethylation are relatively unknown. We have previously identified endothelial to mesenchymal transition (EndMT) as an important contributor to cardiac fibrosis, and TET3 as an enzyme capable of rescuing the expression of fibrosis suppressor genes such as *Rasal1*, in kidney and cardiac fibrosis via reversing aberrant promoter methylation. In this thesis, we used a newly generated endothelial *Tet3* knockout mouse model and demonstrate both elevated EndMT markers expression and increased cardiac fibrosis in these mice. We further provide evidence that TET3 is an upstream regulator of the cardioprotective miRNA, *miR-30d*, which inhibits the EndMT transcription factor *Snail*. Moreover, employing *Rasal1* as a model gene to decipher the mechanism of site-specific demethylation, we here identified that a novel lncRNA termed *Gm15749* located at the promoter of *Rasal1* forms an R-loop and thereby mediates specific recruitment of the active demethylation complex involving TET3 and GADD45G to *Rasal1*. In summary, our results demonstrate several independent antifibrotic mechanisms of TET3 on a molecular level, proposing induction of TET3 and/or induction of its downstream targets as potential new therapeutic options to treat cardiac fibrosis.

1 Introduction

1.1 Cardiac fibrosis

Cardiovascular diseases (CVD) remain the leading cause of death worldwide, comprising up to 30% of mortality (World Health Organization (WHO), 2020). With the huge estimated annual costs that burden global healthcare systems, an urgent need arises to tackle and develop advanced diagnostic tools as well as therapeutic approaches in the cardiovascular field (Gheorghe et al., 2018; Yancy et al., 2013). Studies have shown that patients presenting with ischemic heart disease and myocardial fibrosis are most at risk of progressing into end-stage heart failure (Croft et al., 1999; Lloyd-Jones et al., 2009; Webber et al., 2020). Moreover, a recent study has revealed the direct correlation between myocardial fibrosis and mortality in patients after transcatheter aortic valve implantation (TAVI). The investigators in the study have concluded that myocardial fibrosis above the median was an independent predictor of long-term cardiovascular mortality after TAVI (Puls et al., 2020).

Fibrosis is a process of pathological remodeling of the extracellular matrix (ECM) in response to tissue injury and is considered an important phase of tissue repair (Wynn, 2004). Once fibroblasts are activated, they increase their contractility and start excreting extracellular matrix proteins such as collagen and fibronectin, to kick-start the wound healing process (Dees et al., 2021) (Figure 1). Initially, ECM regulation in response to injury is protective and beneficial. However, excessive and deregulated deposition of collagen can contribute to impaired tissue function. Cardiac ECM consists of a complex network of fibrillar collagens, proteoglycans, fibronectins, laminins, and glycoproteins that perform functions related to structural support and response to signaling molecules. Collagen type I comprises approximately 85% of the total collagen in the heart, followed by collagen type 3 (approximately 11%) (Silva et al., 2021). In physiological conditions, cardiac fibroblasts provide structural support and regulate the release of collagen, which is important for the contractile function of the heart. As a result of injury or disease, cardiac fibroblasts undergo a phenotypic switch and become activated myofibroblasts as the body's first repair response to injury (Figure 1). In turn, this transition leads to pathological changes in heart structure, such as chamber dilation and hypertrophy. In particular, with more collagen and matrix protein deposition, fibrotic scars pose a higher risk of developing diastolic or systolic dysfunction and

arrhythmias (Souders et al., 2009).To better understand the pathological processes in the heart, many studies have identified the composition of the cardiac muscle at even a single-cell resolution. However, there is still insufficient information regarding the mechanisms involved in the interaction between extracellular and cellular components of the heart (Pinto et al., 2016; Zhou & Pu, 2016).

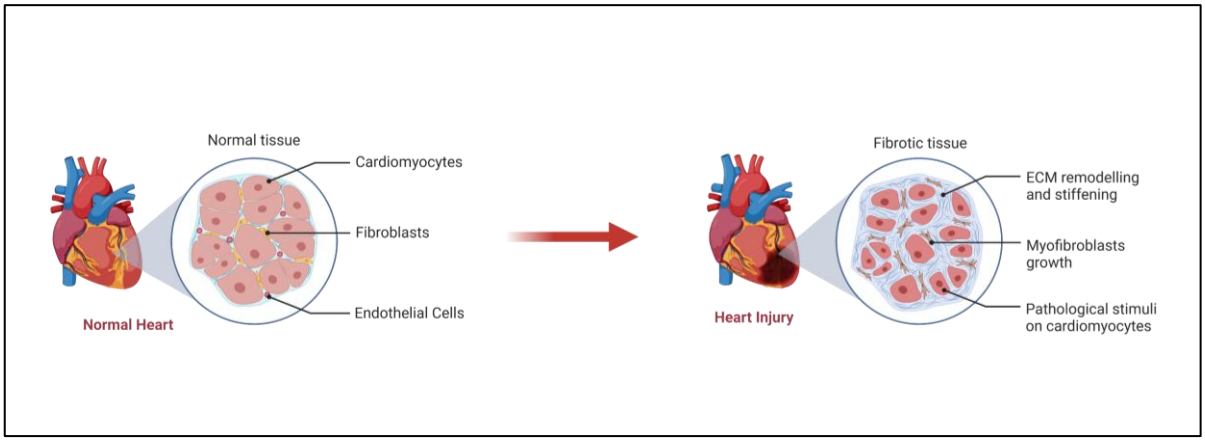

Figure 1: Fibroblast-to-myofibroblast transition after heart injury. In normal conditions, fibroblasts and endothelial cells play a vital role in maintaining homeostasis and providing structural support to the cardiomyocytes. However, upon heart injury, fibroblasts are activated and start secreting ECM proteins, such as collagen, which contributes to the pathological remodeling and stiffening of the heart. Image prepared by biorender.com

1.2 Main cellular composition of the heart

The major cell types of the heart are: cardiomyocytes (atrial and ventricular), endothelial cells, fibroblasts, immune cells, pericytes, smooth muscle cells, adipocytes, mesothelial cells and neuronal cells (Litviňuková et al., 2020). Although the proportion of cells remains controversial, recent single-cell sequencing data have enhanced our understanding of different cell populations in the heart under physiological and pathological conditions. Cardiomyocytes make up approximately 25–35% of the cells in the heart (Tucker et al., 2020; Zhou & Pu, 2016). However, the consensus still lacks concerning how prevalent endothelial cells are. A study in 2016 suggested that endothelial cells account for the major cell population of non-myocytes (around 60%) (Pinto et al., 2016) in the heart. Recent single cell and nuclei RNA sequencing data contradicts this finding and suggests that the endothelial cell population accounts for only 20% and fibroblasts make up around 30% of the heart population

(Litviňuková et al., 2020). These findings together highlight the importance of revisiting the cellular composition of the heart as a key to further understanding cell-to-cell interactions, as well as changes that occur during pathogenesis.

Cardiomyocytes, the main functional cells of the heart, are responsible for generating the contractile force required for adequate pumping and perfusion of the blood to the various organs and tissues. The contractility of each cardiomyocyte is regulated by orchestrated cycles of contraction and relaxation. This is achieved via different ion channels, which regulate the uptake and release of calcium ions ($Ca^{2+)}$ in and out of the cell as well as in the sarcoplasmic reticulum (Woodcock & Matkovich, 2005). Cardiomyocytes depend on their crosstalk with fibroblasts and endothelial cells for mechanical and chemical support to ensure proper cardiomyocyte organization and survival (Hall et al., 2021; Hsieh et al., 2006).

Cardiac fibroblasts (CFs) are derived from mesenchymal cells and spread throughout the heart in strands between cardiac muscle to help support cardiac tissue. They are flat spindle-like cells that lack a basement membrane (Souders et al., 2009). Their main function is to regulate ECM components by mediating the secretion and degradation of collagen through matrix metalloproteinases to maintain homeostasis and the structural and functional integrity of the heart. Moreover, CFs are involved in cell-cell communication with cardiomyocytes and play a role in cardiomyocyte hypertrophy and angiogenesis (Fan et al., 2012). They secrete cytokines and growth factors which can impact cellular processes in other CFs, endothelial cells, and smooth muscle cells. Molecules secreted by cardiac fibroblasts include cytokines (such as TGF-β and TNF-α), peptides (such as angiotensin II and endothelin 1), and growth factors.

During heart injury or disease, cardiac fibroblasts undergo a transition to activated myofibroblasts. Differentiation into the activated form is mainly mediated by TGF-β, cytokines, and other growth factors (Holmes et al., 2005; Weber, 2004). Myofibroblasts are larger in size and have highly active endoplasmic reticulum as well as abundant stress fibers. They are identified by the expression of alpha smooth muscle actin (α-SMA), which is not typically present in resident cardiac fibroblasts. Although myofibroblast formation is the primary response to tissue injury and initiation of repair, the continuous presence of these cells

causes a shift in the ECM balance due to excessive collagen production. This can eventually interrupt myocyte-myocyte interactions, culminating in further impairment of the heart function (Fan et al., 2012; Hinderer & Schenke-Layland, 2019; Weber, 2004).

Endothelial cells line all blood and lymphatic vessels in a single semipermeable layer of cells to form an interface between the circulating blood and the surrounding tissue (Gimbrone, 1987; Krüger-Genge et al., 2019). The main function of endothelial cells is to regulate the flow of substances and vascular permeability of tissues. In the heart, endothelial cells are vital for the proper functioning of the endocardium and myocardial capillaries, where they are in direct contact with cardiomyocytes (Bassenge, 1996; Bassenge & Heusch, 1990; Davies, 1995). Moreover, they regulate the vascular tone by secreting several vasoconstrictive molecules such as thromboxane (TXA2) and endothelin-1 (ET-1) and vasodilatory molecules such as nitric oxide (NO), prostacyclin (PGI2), and endothelium-derived hyperpolarizing factor (EDHF) (Sandoo et al., 2015).

Cardiovascular risk factors, such as smoking, aging, diabetes, and hypertension are all mediators of endothelial dysfunction. Alterations in endothelial function include loss of proper vasodilatory properties along with increased constriction of blood vessels and oxidative stress, and accumulation of prothrombotic products. Consequently, this chronic inflammatory process further increases the risk of cardiovascular events (Marti et al., 2012; Zuchi et al., 2020).

1.3 Cardiac fibroblast to myofibroblast transdifferentiation

Cells that contribute to the myofibroblast population include resident fibroblasts, endothelial cells through the process of endothelial-to-mesenchymal transition (EndMT), and epithelial cells through the process of epithelial-to-mesenchymal transition (Pardali et al., 2017). Endothelial to mesenchymal transition is a cellular process whereby the endothelial cells lose endothelial markers such as CD-31 and VE Cadherin and instead start expressing mesenchymal markers such as α-SMA transitioning to a fibrotic phenotype (Figure 2). EndMT was originally identified during cardiac development, where endocardial endothelial cells undergo a transition to form the cardiac valves and septum (Lagendijk et al., 2013; Markwald et al., 1975). Studies have shown that EndMT also occurs in the adult heart in response to

injury as endothelial cells attain a fibroblast-like phenotype, contributing as a result to cardiac fibrosis (Xu et al., 2016; Zeisberg, Tarnavski, et al., 2007; Zhang et al., 2018). In response to extracellular stimuli (such as inflammation and hypoxia), cytokines such as TGF-β are transcribed and secreted by cells to trigger a number of biological processes. For instance, TGF-β1 binds to the TGF-β type II receptor, which in turn activates the type 1 TGF-β receptor activin A receptor type II-like kinase (ALK5). ALK5 then recruits and phosphorylates both SMAD2 and SMAD3 transcription factors which form a complex with SMAD4. The complex then translocates to the nucleus and induces the expression of EndMT transcription factors, such as *Snail*, *Slug*, and *Twist* (Goumans et al., 2009) (Figure 2). As a result, these transcription factors induce mesenchymal gene expression and repress endothelial gene expression.

It has been previously reported that EndMT-derived fibroblasts account for <1% of the total number of cells in normal condition. However, upon ischemic heart injury, the number expands to >25% of total isolated cells (Aisagbonhi et al., 2011). Recently, single cell sequencing data has demonstrated that endothelial cells do acquire a fibroblast like phenotype, however, this transition is rather reversible, and the investigators have renamed the process as EndMA (endothelial to mesenchymal activation) (Tombor et al., 2021).This suggests the need to further decipher this process to understand the contribution of endothelial cells to pathological fibrosis.

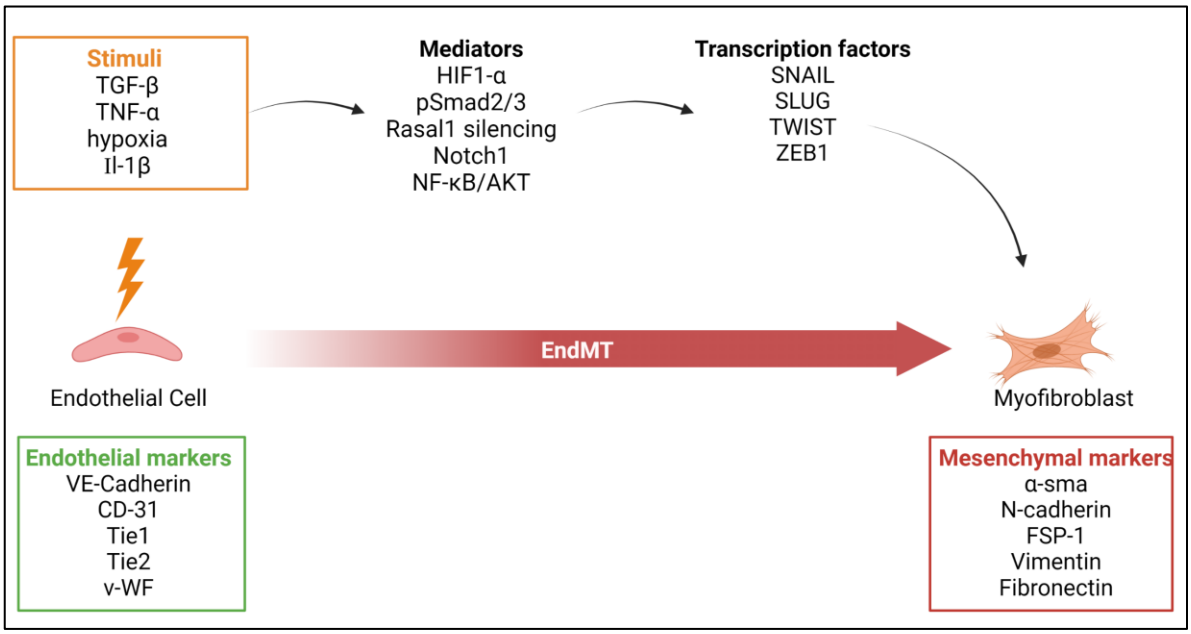

Figure 2: Endothelial-to-mesenchymal transition. Schematic depicting the factors involved in EndMT. Under pathological conditions, endothelial cells are activated in response to various stimuli,

such as TGF-β and TNF-α, which results in the loss of endothelial markers and gain of mesenchymal markers. The transition to mesenchymal cells (myofibroblasts), accompanied by morphological changes from a cuboidal to a spindle shape, is mainly attributed to the activation of EndMT transcription factors such as Snail, Slug, and Twist. Image prepared by biorender.com

1.4 Epigenetics

1.4.1 Epigenetic modifications

The term epigenetics was coined in 1942 by the biologist Conrad Waddington in an attempt to explain alterations that occur in the phenotype which are not due to changes in the genotype itself (DNA sequence) (Waddington, 1942, 2011). The well-known epigenetic landscape introduced by Waddington was the hallmark of understanding the complex and dynamic interaction between the environment and the genome to produce a certain phenotype(Jr & Waddington, 1943). Molecular epigenetics has become a crucial field for understanding gene regulation during development and pathological conditions. Epigenetic modifications occur both at the chromatin and DNA levels. These modifications incur changes to the chromatin structure itself between an active state where the DNA is accessible and an inactive state where the chromatin is condensed making the DNA inaccessible (Egger et al., 2004). Key modifications include histone modifications, DNA methylation, and non-coding RNA regulation.

1.4.2 Histone modifications

The nucleosome consists of 147 DNA base pairs and is wrapped around an octamer of histone proteins (McGhee & Felsenfeld, 1980). Each octamer consists of two copies of histone proteins H2A, H2B, H3, and H4, which are required to compact the DNA (Kornberg, 1974). Histones are regulated by a number of post translational modifications, such as acetylation, methylation, phosphorylation, and ubiquitination via histone modification enzymes (Bannister & Kouzarides, 2011). For instance, single acetylation of Lys-9 (H3K9ac) and Lys-14 (H3K14ac) is associated with transcriptionally active chromatin regions. In addition, trimethylated (me3) Lys-4 (H3K4me3) is enriched at active promoter regions near transcription start sites (TSS) (Barski et al., 2007; Bernstein et al., 2005; Ernst et al., 2011). The histone acetyltransferase P300, which acetylates H3 at the lysine residue 27 (H3K27ac) is an important modifier during heart development. It binds to the promoter regions of essential

heart transcription factors such as Mefc2, Nkx2-5, and Gata4, thereby mediating transcription activation (Sun et al., 2010; Takaya et al., 2008; Trivedi et al., 2010). Studies have shown that mice carrying a point mutation in the P300 gene have both atrial and ventricular septal defects (Shikama et al., 2003).

1.4.3 Non-coding RNAs

Noncoding RNAs (ncRNAs) are a group of RNA molecules that are not translated into proteins. Scientists have argued about the biological functions of ncRNAas, which were initially termed as junk, but now have reached a consensus regarding their importance (Mattick, 2004; Struhl, 2007). ncRNAs are generally categorized into housekeeping ncRNAs and regulatory RNAs. Regulatory RNAs are divided according to size, where long non-coding RNAs (lncRNAs) are usually larger than 200 bp and short ncRNAs include miRNAs microRNAs (miRNAs), small interfering RNAs (siRNAs), and Piwi-interacting RNAs (piRNAs).

1.4.4 DNA methylation

DNA methylation involves the addition of a (CH3) group to the 5'-carbon of the cytosine nucleotide. The reaction is catalyzed by DNA methyltransferase enzymes (DNMTs), resulting in the formation of 5-methylcytosine (5mC). The methylation generally occurs at cytosine residues that are followed by guanosine (also known as CpG sites) in the DNA sequence which are prevalent at the promoter regions of genes. As a protective mechanism, the mammalian genome, which consists of approximately 45% transposable and viral elements, is silenced by DNA methylation (Schulz et al., 2006). With the formation of 5mC, transcription of target genes can be repressed either by blocking the specific binding of transcription factors to the recognition site in the promoter region or by direct binding of transcriptional repressor proteins such as methyl CpG binding protein 2 (MECP2) to the methylated DNA, coupled by the recruitment of histone-modifying enzymes that induce a closed chromatin structure (Curradi et al., 2002). Promoter methylation was first reported in the field of cancer with the effect observed on tumor suppressor genes, which were aberrantly silenced due to DNA methylation, contributing further to tumor development and progression (Das & Singal, 2004).

1.4.5 TET mediated active DNA demethylation

Ten-eleven translocation (TET) methylcytosine dioxygenase proteins consist of TET1, TET2, and TET3 enzymes, respectively. They are α-ketoglutarate and Fe^{2+}-dependent dioxygenases that initiate DNA demethylation (Pastor et al., 2013). TET enzymes of mammalian origin are usually large, between 180 and 230 kDa, and consist of several functional domains. They all share a Cys-rich catalytic domain located on the C-terminus with a double-stranded b-helix (DSBH) fold, which forms the binding sites required for the cofactors α-ketoglutarate and Fe2+. The DSBH domain also includes a large low-complexity insert that varies in size among the three paralogs (Figure 3). At their N-terminal, both TET1 and TET3 possess a CXXC-zin-finger domain required for DNA binding at the CpG islands. Due to chromosomal inversion, the CXXC domain of TET2 is separately encoded by the gene *CXXC4*, which is transcribed in the opposite direction. The CXXC4 protein also known as IDAX, is responsible for the recruitment of TET2 to CpG islands (L. Hu et al., 2015; Wu & Zhang, 2017).

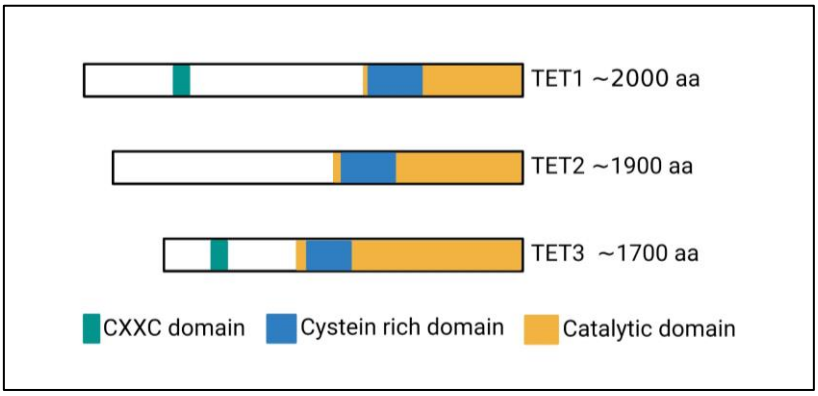

Figure 3: Ten-eleven translocation methylcytosine dioxygenase enzymes family. The mammalian genome (in this figure, mice) encodes three TET enzymes with varying amino acid lengths. The diagram depicts the main functional domain structures, including the CXXC DNA-binding domain, chromatin-targeting cysteine-rich domain, and dioxygenase catalytic domain. Image prepared by biorender.com

1.4.6 TET proteins enzymatic mode of action

TET enzymes catalyze the oxidation of 5mC by the incorporation of an oxygen atom to form 5-hydroxymethylcytosine (5hmC), 5-formylcytosine (5fC), and 5-carboxylcytosine (5caC) (Kriaucionis & Heintz, 2009; Tahiliani et al., 2009). After TET-mediated oxidation leads to the formation of 5fC and 5caC, bases are further excised by thymine DNA glycosylase to form

an unmodified cytosine residue (Kohli & Zhang, 2013). Although the CXXC DNA-binding motif of TET enzymes has been well characterized, not much is known about how TET enzymes are recruited to gene promoters. Recently, the stress response proteins GADD45 (growth arrest DNA damage protein 45) have been shown to promote locus-specific DNA demethylation by anchoring and acting as adaptors for TET/TDG mediated demethylation (Z. Li et al., 2015; Schüle et al., 2019).

1.4.7 TET enzyme expression

TET enzymes are involved in a several processes including development and stem cell differentiation. In general, TET3 is the major TET enzyme expressed in oocytes and fertilized zygotes, and TET1 and TET2 enzymes are expressed later during early development (Tan & Shi, 2012). TET enzymes have also been detected in several adult tissues, with differential isoform domination. For example, the short isoform of TET1, that lacks the N-terminal, has been shown to be the dominant TET1 in differentiated tissues, even though it has reduced chromatin binding capacity. Moreover, the number of TET3 isoforms expressed in oocytes is different than that expressed in neurons due to alternative splicing. Although TET2 is encoded by a single transcript, differential regulatory sequences modulate its expression in cell-specific contexts. In mouse embryonic stem cells, *Tet2* attains a distally located intragenic enhancer, which is reduced in differentiated cells. Meanwhile, in differentiated cells, *Tet2* expression is achieved via interaction with cell-specific regulatory sequences such as CCAAT enhancer-binding protein alpha (CEBPα), which drives pre-cell differentiation into macrophages. Loss of TET enzyme expression or activity has been associated with poor cancer prognosis and prevalence of malignancies (Lemonnier et al., 2012; Odejide et al., 2014; Quivoron et al., 2011). To elucidate the roles of TET enzymes, several knockout models have been generated, including single, double, and triple knockout mouse models. The models included both constitutive and conditional cell-type specific knockouts, and the main findings highlighted different spatiotemporal functions which will be discussed below.

1.4.8 TET knockout mouse models

Studies investigating the functional roles of TET enzymes using genetic knockout (KO) mouse models have revealed the physiological relevance of TET proteins in development. For

instance, constitutive knockout of *Tet3* is associated with neonatal lethality with 100% penetrance (Gu et al., 2011; Kang et al., 2015), whereas deletions of either *Tet1* or *Tet2* do not result in alterations in development (Dawlaty et al., 2011; Moran-Crusio et al., 2011). This implies the hierarchical importance of TET3 during the early stages of embryogenesis compared to TET1 and TET2. Moreover, combined deletion of *Tet1* and *Tet2* resulted in a heterogeneous phenotype with some mice surviving and a gross majority of the litter dying perinatally and exhibiting a wide array of defects including growth retardation and exencephaly (Dawlaty et al., 2013). In adult mice, deletion of *Tet3* in adult postmitotic neurons resulted in increased anxiety-like behavior, which investigators found was due to the involvement of *Tet3* in the molecular mechanisms that regulate hippocampal functions (Antunes et al., 2021). Recently, Fang et al. generated a cardiomyocyte-specific *Tet2/Tet3* conditional knockout mouse model and reported embryonic lethality caused by ventricular noncompaction cardiomyopathy (Fang et al., 2019). Although a lot of research has highlighted the important roles of TET enzymes in development, hematopoiesis, and neurological processes, it is crucial to further decipher the epigenetic regulatory mechanisms that alter cardiac remodeling.

1.4.9 Role of TET enzymes in heart development and disease

The alterations of epigenetic marks occurring at the DNA level have emerged as key regulators of cardiac development and disease (Greco et al., 2016; Han et al., 2011; Papait et al., 2013). Whole-genome bisulfite sequencing of DNA methylation in the cardiac genome has revealed it to be a dynamic process that is important for regulating the postnatal growth of cardiomyocytes as well as their adaptation to pathological stress (Gilsbach et al., 2014). Further, mounting evidence has supports the involvement of DNA methylation in cardiac dysfunction (Baccarelli et al., 2010; Friso et al., 2008; Khyzha et al., 2017; Rau & Vondriska, 2017; Zhuang et al., 2017). Previous studies have revealed that changes in the methylation status is a contributor to several processes underlying cardiovascular diseases, such as hypertension, atherosclerosis, and inflammation.

1.4.10 Role of TET3 enzymes in fibrosis

Previous research by our group has highlighted the protective role of TET3 in both kidney and cardiac fibrosis models (Tampe et al., 2014, 2015; Xu et al., 2018). Specifically, they demonstrated that hypermethylation and subsequent silencing of the fibrosis-suppressor gene *Rasal1* were concomitant with decreased *Tet3* expression (Tampe et al., 2014). The silencing of *Rasal1* is associated with increased EndMT and contributes to an aggravated fibrosis phenotype (Xu et al., 2015). Moreover, Tampe et al. showed that BMP7 can induce *Tet3* expression, which in turn reverses the hypermethylation of *Rasal1* and rescues its expression, resulting in attenuation of fibrosis. Recently, Xu et al., developed a gene-specific hydroxymethylation system by employing the TET3 catalytic domain (TET3CD) fused to an endonuclease deactivated high fidelity Cas9 (dHFCas9) to target specific genes which are methylated during fibrosis (Xu et al., 2018). Altogether, these data highlight the important role played by TET3 in the regulation of fibrosis. However, a deeper understanding of the mechanisms involved in the recruitment of TET3 to gene promoters should be sought. In addition, further investigation regarding the involvement of TET3 in the EndMT process and cardiac remodeling should be examined.

1.5 Emerging genetic and epigenetic regulators

1.5.1 Role of miRNAs in the heart

miRNAs are small endogenous non-coding RNAs (approximately 18-22 nucleotides in length) that play an important role in regulating post-transcriptional gene expression (Ambros, 2004; Bartel, 2004). In most cases, these act by binding to the 3'-UTR of the target gene mRNA via base pairing and regulate its expression by inhibiting the translation process and promoting mRNA degradation (Huntzinger & Izaurralde, 2011). Most miRNAs are transcribed from DNA sequences located in intergenic or intronic loci by RNA polymerase II as long primary miRNA transcripts (pri-miRNAs). The pri-miRNA is then cleaved by the endoribonuclease Drosha to form the pre-miRNA, which has a 70-nucleotide long hairpin structure. Pre-miRNA is then exported outside the nucleus by exportin 5 and RanGTP, and further processed by Dicer in the cytoplasm (RNase enzyme III) to form a 22 nucleotide miRNA:miRNA duplex. Usually, a single strand from the duplex (either 5p or 3p, i.e., 5' or 3' of pre-miRNA) is incorporated

into the microRNA-induced silencing complex (miRISC), and the other passenger strand is then degraded (Rana, 2007).

Since their discovery 20 years ago, miRNAs have been shown to regulate gene expression in key physiological and pathological cardiac processes(Colpaert & Calore, 2019) . Investigators have found that inhibition of miR-92a in the heart protects against ischemia/reperfusion in a porcine model by exerting proangiogenic and anti-inflammatory effects (Hinkel et al., 2013). These findings resulted in the development of the first miRNA therapy against cardiovascular diseases in humans with preliminary trials showing a positive effect on heart function with increased angiogenesis and blood circulation (Abplanalp et al., 2020).

1.5.2 The protective role of miR-30d in the heart

miR-30d has recently emerged as a new cardioprotective biomarker, highlighting its potential as a therapeutic target. Translational studies have shown that higher circulating levels of miR-30d is associated with a more favorable response to cardiac resynchronization treatment (Melman et al., 2015). It has also been identified as a novel prognostic biomarker that can predict the survival of patients with acute heart failure (Xiao et al., 2017). Further mechanistic studies have revealed that miR-30d can target several genes involved in cardiac hypertrophy. In cardiomyocytes, miR-30d prevents cardiac dysfunction and cardiomyocyte apoptosis by targeting the mitogen-activated protein kinase 4 (MAP4K4). Further, investigators have shown that *miR-30d* can also target integrin alpha 5 (ITGA5) in cardiac fibroblasts to regulate fibroblast activation (J. Li et al., 2021). *miR-30d* was primarily described in cancer research, where investigators highlighted its role in regulation of cell proliferation, migration, and invasiveness (Cui & Bian, 2021; Xu et al., 2021; Ye et al., 2015; Zhu et al., 2018). Specifically, investigators reported that the protective role *miR-30d* to control tumor progression involved targeting EMT markers, such as *Snail* and *Slug* (Xu et al., 2021; Ye et al., 2016). Interestingly, one study has suggested that *miR-30d* is a downstream target of Tet3 and can contribute to the suppression of EMT in ovarian cancer cells (Ye et al., 2016).

Since all the studies on the heart highlighted the role of miR-30d in fibroblasts and cardiomyocytes only, it would be useful to explore its role in cardiac endothelial cells and EndMT in light of the previous knowledge acquired from cancer research.

1.5.3 Role of R loops in facilitating DNA demethylation

R-loops are a three-stranded nucleic acid structures comprising a DNA:RNA hybrid (Figure 4). They were first discovered in 1976 when Davis et al. demonstrated the capability of R-loop formation in the presence of yeast DNA, bacteriophage λ DNA, and a 26S rRNA complementary to the yeast DNA (Thomas et al., 1976). The initial observation revealed immense stability of the three-stranded nucleic acid structure that could only be resolved via degradation of the RNA strand. Although not much light has been shed on the biological function of these R-loop structures, research over the last decade has revolutionized our understanding of the regulatory role of R-loops. Most importantly, scientists have identified the important role of R-loops in immunoglobulin class switching (Dickerson et al., 2003; Sohail et al., 2003). Additionally, R-loops have emerged as a new potential epigenetic regulatory mechanism at the interface of several nuclear processes, including transcription, RNA processing, DNA demethylation, DNA damage, and chromatin regulation (Crossley et al., 2019; Gan et al., 2011; García-Muse & Aguilera, 2019; Niehrs & Luke, 2020; Ribeiro de Almeida et al., 2018).

Recently, lncRNAs have been shown to form R-loops that can interact with and recruit different chromatin modifiers at gene promoters to regulate gene expression (Beckedorff et al., 2013; Boque-Sastre et al., 2015; Gibbons et al., 2018). LncRNA-based R-loops can form in both *cis* and *trans* directions and are enriched at CpG islands making them top candidates for site-specific gene regulation (Ginno et al., 2012). For instance, the lncRNA *TARID* (TCF 21, antisense RNA inducing demethylation), which is transcribed in the *cis* orientation of the TCF-21 gene, forms an R-loop at the promoter of TCF-21 thereby activating its expression by inducing promoter demethylation (Arab et al., 2014, 2019) . The investigators in this study revealed that TARID facilitates the binding of GADD45α, which then physically interacts and recruits TET1 to induce site specific demethylation and reactivation of the tumor suppressor gene TCF21 (Arab et al., 2019; Kienhöfer et al., 2015).

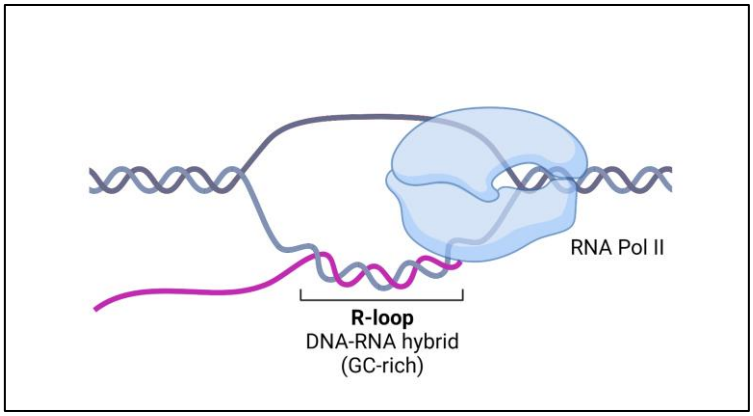

Figure 4: R-loop structure. Schematic depicting R-loops which are three-stranded nucleic acid structures consisting of a DNA: RNA hybrid and a displaced strand of DNA. R-loops can form in cis when an RNA strand anneals to the DNA template behind RNA polymerase II during transcription. Schematic was created by Biorender.com

2 Scope of the thesis

In this thesis, we investigate the role TET3 plays in endothelial cells and its effect on the cardiac remodeling process. As such, we explore the impact and underlying mechanisms behind the loss of TET3 in endothelial cells on the cardiac function and EndMT process.

The objectives are as follows:

1. Generate and validate an endothelial specific *Tet3* knockout mouse model
2. Evaluate the effect of loss of Tet3 on cardiac remodeling and fibrosis
3. Evaluate differential gene expression and identify new targets of *Tet3* in relation to EndMT

Next, we utilized our previous knowledge regarding the protective role TET3 plays in rescuing the expression of the fibrosis-suppressor gene *Rasal1* in both kidney and cardiac fibrosis models (Tampe et al., 2014, 2015; Xu et al., 2018). During fibrosis, TET3 protein and mRNA expression is reduced, and the remnant TET3 alone is not capable of restoring *Rasal1* expression. As such, we sought to further understand how demethylation enzymes are recruited to specific genomic loci. In line with these ideas, the present study aims to:

1. Identify the mechanism required for site-specific demethylation
2. Identify key proteins which interact with TET3 to aid in the demethylation process
3. Unravel the demethylation complex required for site-specific demethylation of *Rasal1*

3 Materials

3.1 Biological Material

Cell lines used are listed in Table 1.

Cells	Manufacturer
Hek293 Human embryonic kidney 293 cells	ATCC
MCF Mouse cardiac fibroblasts	ScienCell
MCEC mouse cardiac endothelial cells	Cedarlane

3.2 Chemicals

Chemicals used in the experiments are listed in Table 2

Chemical	Manufacturer	Catalog Nr.
1kb DNA Ladder	Promega, USA	G1881
4x Nupage LDS sample buffer	Invitrogen	NP0007
20x Nupage transfer buffer	Life technologies	NP0006
40% Polyethylene glycol PEG	Amresco	0159-2.5KG
20X LumiGLO substrate A	Cell Signaling Technology	7003S
20X Peroxide substrate B	Cell Signaling Technology	7003S
6x Blue/Orange loading dye	Promega, USA	G190-A
100% Ethanol	ROTH	9065.2
Albumin Fraction V	ROTH	8076.3
Angiotensin II	Sigma Aldrich	A9525-50MG
Angiotensin II minipump 4 weeks	Alzet	1004
Benzonase nuclease	Sigma-Aldrich	E1014-25KU
Biozym LE Agarose	Biozym	840004
cDNA synthesis Reagents: • dNTP mix • 0.1mM DTT • 5x FS (first strand) Buffer	Invitrogen, GER	18080-093

• RNaseOUT • SuperscriptII Reverse transcriptase • Stop Buffer (Sigma) • DNase • 10x Reaction Buffer		
cOmplete Tablets, Mini EASYpack	Roche	04693124001
Chloroform	J.T. Baker	67-66-3
Citrate buffer 10x pH 6	Dako	S2369
Direct Red 80	Sigma-Aldrich	365548-5G
Dimethyl sulfoxide (DMSO)	Sigma-Aldrich	D8418
DNA Retardation Gels (6%), 1.0 mm	Thermo Fisher	EC6365BOX
Fast SYBR Green Master Mix	Applied Biosystems	4385612
Fetal Bovine Serum	Gibco, GER	10270-106
Glycogen, molecular biology grade	Thermo Fisher	R0561
HEPES (1 M)	Thermo Fisher Scientific	15630080
Hydrogen peroxide 30%	ROTH	8070.4
dPBS (- $CaCl_2$, $MgCl_2$)	Gibco, GER	14190250
Immu-Mount	Epredia	9990402
Isopropanol	ROTH	6752.2
Lipofectamine 2000	Invitrogen	11668-019
Lipofectamine 3000	Thermo Fisher Scientific	L3000008
$MgCl_2$	Sigma Aldrich	M1028-100ML
MTS Staining Chemicals • Phosphotungstic acid • Phosphomolybdic acid • Biebrich scarlet-acid fuchsin • Weigert´s iron hematoxylin A • Weigert´s iron hematoxylin B	Sigma Aldrich	 HT152 HT153 HT151 HT107 HT109

NP40 Lysis Buffer 10x	Invitrogen	FNN0021
Nylone Membrane	Thermo Fisher Scientific	77016
Picric Acid		P6744
Penicillin/Streptomycin	Sigma-Aldrich	P4333-100ml
Phusion PCR Reagents: • 5x Phusion Buffer • dNTP mix • DMSO • Phusion Polymerase	New England Biolabs	M0530S
Phosphatase Inhibitor Cocktail	Sigma Aldrich	P5726
Powdered milk	ROTH	T145.2
Polyethyleneimine PEI	Sigma-Aldrich	408727
PrimeSTAR GXL DNA Polymerase	Takara	R050A
Proteinase K	Thermo Fisher Scientific	AM2546
Protein G Sepharose™ 4 Fast Flow	GE Healthcare	17-0618-01
PVDF membrane filter paper sandwich	Life Technologies	LC2002
Rapid ligation buffer	Promega	C761b
Recombinant GADD45g protein	Lsbio	LS-G26114
Restore™ Western Blot Stripping Buffer	Thermo Fisher Scientific	20159
RNase Zap	Ambion	AM9782
Rotiphorese® 10x TAE Buffer	ROTH	T854.2
Sodium Chloride	Sigma-Aldrich	S6191-500G
SYBR®Safe DNA Gel Stain	Applied Biosystems	4385612
Taq DNA polymerase	Takara	R004A
TGF-ß1	R&D systems	7666-MB-005
Trypsin-EDTA solution 0.25%, phenol red	Sigma-Aldrich	T4049-100mL
TRIzol	Ambion	15596-026
Tween20	Roth	9127.2

UltraPure™ TBE Buffer, 10X	Thermo Fisher Scientific	15581044
Zeocin	Invivogen	Ant-zn-05

3.3 Enzymes

Enzymes used are listed in Table 3

Enzymes	**Manufacturer**	**Catalog No.**
Amplitaq 360 DNA polymerase	Applied Biosystems	4398881
AsisI	New England Biolabs	R0630L
BamHI-HF	New England Biolabs	R3136L
Cut Smart Buffer	New England Biolabs	B7204S
HindIII-HF	New England Biolabs	R3104L
MIuI-HF	New England Biolabs	R3198L
RNase H, recombinant	New England Biolabs	M0297S
T4 DNA ligase	Promega	M180A

3.4 Primary Antibodies

Primary antibodies used are listed in Table 4

1° Antibody	**Assay**	**Manufacturer**	**Catalog Nr.**
5mC Antibody	DB	Active motif	39649
αSMA	IF	Sigma-Aldrich	A5228
Alexa Fluor® 647 Rat Anti-Mouse CD144	FACS	BD Biosciences	562242
CD-31	IF	Dianova	DIA-310
DDK-tag	WB	Origene	TA50011-100
GADD45g	IF, Co-IP, WB, ChIP	Abcam	ab196774
GAPDH	WB	Santacruz	sc-32233
IgG	Co-IP	Active motif	53017
Myc-Tag	WB	Cell Signaling	2276S

Normal mouse IgG	DRIP	Santacruz	sc-2025
Phalloidin-488	IF	Abcam	ab176753
S9.6	DRIP	Kerafast	ENH001
Snail	WB	Origene	OTI10D7
TET3	IHC	Genetex	GTX02579
TET3	IF,Co-IP, WB	Genetex	GTX121453

3.5 Secondary Antibodies

Secondary antibodies used are listed in Table 5

2° Antibody	**Manufacturer**	**Catalog Nr.**
Anti-mouse HRP	Dako	P0447
Anti-Rabbit HRP	Dako	P0448
Alexa Fluor 488 Anti Rat	Dianova	112-545-003
Alexa Fluor 488 anti-Rabbit	Thermo Fisher Scientific	A-11008
Alexa Fluor 488 anti-mouse	Thermo Fisher Scientific	A-11001
Alexa Fluor 594 anti-Rabbit	Thermo Fisher Scientific	A-11012
Alexa Fluor 488 anti-mouse	Thermo Fisher Scientific	A-11005

3.6 Kits

Kits used in the experiments are listed in Table 6

Kits	**Manufacturer**	**Catalog Nr**
CpG Methylase (M. SssI)	Zymo Research	E2010
DNA Clean & Concentrator-5	Zymo Research	D4003
DNeasy Bloods & Tissue Kit	Qiagen	69506
Hispeed Plasmid Midi Kit	Qiagen	12643
Immunoprecipitation Kit Protein G	Roche	11719386001
LightShift Chemiluminescent RNA EMSA Kit	Thermo Fisher Scientific	20158
Luc-Pair Luciferase Assay Kit 2.0	Biocat	LF001-GC
MEGAscript™ T7 Transcription Kit	Thermo Fisher Scientific	AM1333
miRCURY LNA SYBR Green PCR Kit	Qiagen	339346

Methylamp Methylated DNA capture (MeDIP) kit	Epigenetik	P-1015-48
Phusion High-Fidelity PCR Kit	NewEngland Biolabs	M0530S
Pierce BCA Protein Assay Kit	Thermo Fisher Scientific	23225
Pierce™ RNA 3' End Biotinylation Kit	Thermo Fisher Scientific	20160
Pure Link RNA Mini Kit	Ambion	12183025
QIAquick Gel Extraction Kit	Qiagen	28704
Vectastain elite abc universal kit	VECTOR Laboratories	PK-6200
Zippy Plasmid Miniprep Kit	Zymo Research	D4037

3.7 Instruments

Instruments used in the experiments are listed in Table 7

Instrument	Provider
AF 80 Flake Ice Maker	Scotsman-Ice, Illinois, USA
Autoclave LGAK0027	Teenomara, Fernwald, Germany
Bacterial Incubator	Thermo Scientific, USA
Bacterial Shaker	Thermo Scientific, USA
BioDoc Analyze Gel imaging	Biometra
ChemiDoc MP System	Bio-Rad, Munich, Germany
FluoView FV100	Olympus, Shinjuku, Tokyo, Japan
Mastercycler X50s	Eppendorf, Hamburg, Germany
Microtome Leica RM2165	Leica Microsystems, Wetzlar, Germany
Microscope BX43 Brightfield	Olympus, Shinjuku, Tokyo, Japan
MiniSpin Centrifuge 5452	Eppendorf, Hamburg, Germany
NanoDrop 2000	Thermo Fisher Scientific, Massachusetts, USA
Nitrogen Tank APOLLO	Messer, Griesheim, Germany
Paraffin embedding Leica 1120 H	Leica Microsystems, Wetzlar, Germany
PerfectSpin P	Peqlab Biotechnology, Erlangen, Germany
PHOmo Microplate Reader	Autobio, China
Pipetus	Hirschmann, Eberstadt, Germany
Protein Transfer Fastblot B44	Biometra, Goettingen, Germany
Rotamax 120	Heidolph, Schwabach, Germany
Steam cooker 3216	BRAUN GmbH, Kronberg, Germany

StepOnePlus Real-Time PCR System	Applied BiosystemsMassachusetts, USA
Synergy HTX Multimode Reader	Biotek, Vermont, USA
Thermomixer comfort	Eppendorf, Hamburg, Germany
TissueLyser LT	Qiagen, Hilden, Germany
Top Loading Balances TE2101	Sartorius, Goettingen, Germany
Tube Roller Mixer SRT6	Bibby Scientific, Stuart, Staffordshire, UK
Ultrasonic Liquid Processors S-400	Misonix Sonicators, Newtown, Connecticut
Vortex Genie 2	Bender & Hobein AG, Zurich, Switzerland

3.8 qRT-PCR primers

Primer sequences used in qRT-PCR assay are listed in Table 8

Primer		**Sequence**
Gapdh	Sense	TGTAGACCATGTAGTTGAGGTCA
	Antisense	AGGTCGGTGTGAACGGATTTG
Tet3	Sense	CTCCCCTGCTGTCTTCAGA
	Antisense	CCTGAGGCTCTGTGGAAGTA
Myh6	Sense	ATGTGCCGGACCTTGGAA
	Antisense	CCTCGGGTTAGCTGAGAGATCA
Myh7	Sense	GCCCAGTACCTCCGAAAGTC
	Antisense	ATCAGGCACGAAGCACTCC
Nppa	Sense	TTCTTCCTCGTCTTGGCCTTT
	Antisense	GACCTCATCTTCTACCGGCATCT
Nppb	Sense	TCCTAGCCAGTCTCCAGAGCAA
	Antisense	GGTCCTTCAAGAGCTGTCTCTG
Col1a1	Sense	CCTCAGGGTATTGCTGGACAA
	Antisense	CAGAAGGACCTTGTTTGCCAG
Acta2	Sense	GTCCCAGACATCAGGGAGTAA
	Antisense	TCGGATACTTCAGCGTCAGGA
Gm15749	Sense	CGTGACATTTAAGGCACACC
	Antisense	AACCTCTCTGTTCCTCGGTTT
Gadd45a	Sense	CCTGGAGGAAGTGCTCAGCAAG
	Antisense	GTCGTCTTCGTCAGCAGCCAG
Gadd45b	Sense	GGAGACATTGGGCACAACCGAA
	Antisense	CTGCTCTCTTCACAGTAACTGGC
Gadd45g	Sense	GGGAAAGCACTGCACGAACT
	Antisense	AGCACGCAAAAGGTCACATTG
Rasal1	Sense	GTCTGTGGGCGCTCAGTCT
	Antisense	AGGCCAGGTGGTGGAAGT
Pecam-1	Sense	CCAAAGCCAGTAGCATCATGGTC
	Antisense	GGATGGTGAAGTTGGCTACAGG
Snai1	Sense	CTGCTTCGAGCCATAGAACTAAAG

	Antisense	GAGGGGAACTATTGCATAGTCTGT
Snai2	Sense	TCTGTGGCAAGGCTTTCTCCAG
	Antisense	TGCAGATGTGCCCTCAGGTTTG
Tet3 3-4	Sense	GGACACACCGGCCAAGAAG
	Antisense	GCCAGATCCCAGGTGAGTG
Tet3 5-6	Sense	GGCAAGGAGGGGAAGAGTTC
	Antisense	ACAATCACGGCGTTCTGACA
Tet3 7-8	Sense	GCATGTACTTCAACGGCTGC
	Antisense	GAGGGGAGCAACTTCAGTGG
AAV-Cre	Sense	GTCCCTGGTGATGAGGAGAA
	Antisense	TGGTCAAAGTCAGTGCGTTC
Unisp6	Sequence	CUAGUCCGAUCUAAGUCUUCGA
miR-30d-MeDIP	Sense	TTTGGCGGGGAAATGCAC
	Antisense	AAGGGCTCGGGACACTTC
miR-30d-5p	Sequence	UGUAAACAUCCCCGACUGGAAG
U6 Snrna	Sequence	GUGCUCGCUUCGGCAGCACAUAUACUAAAAUUGGAA CGAUACAGAGAAGAUUAGCAUGGCCCCUGCGCAAGG AUGACACGCAAAUUCGUGAAGCGUUCCAUAUUUUU

3.9 Genotyping PCR primers

Primer sequences used in genotyping PCR assay are listed in Table 9

Primer		Sequence
Tet3 I-II	Sense	TCAGCAGGAAAGCACCACAAG
	Antisense	CACTAGACCCCAGATCAACCCA
Tet3 III-IV	Sense	TGGGGATGAGACTGAACTCGG
	Antisense	GGTACAAAGGCTGGCATGGTTA
Tet3 P1-P2	Sense	ATGGGCCTTCATCTTTCTCC
	Antisense	CCATGGAGCTGATTCCTTTC
Tet3 P5-P6	Sense	GCTTTCCTACAGTGTTGCTTG
	Antisense	AGCCATAACTCAGACTTTTCCT
Tet3 P7-P8	Sense	AAGGTCTTGCATCCAACCCA
	Antisense	GATATCGTCAACACCCTGTCCC
Cre	Sense	GCGGTCTGGCAGTAAAAACTATC
	Antisense	GTGAAACAGCATTGCTGTCACTT
Internal Control	Sense	CTAGGCCACAGAATTGAAAGATCT
	Antisense	GTAGGTGGAAATTCTAGCATCATCC

3.10 Vectors

Vectors purchased for cloning purposes are listed in Table 10

Vector	Manufacturer	Catalog number
miR-30d-5p mimic	Qiagen	YM00470778
miRNA negative control	Qiagen	YM00479902
pAAV-Cre	Cellbiolabs	AAV-401
pcDNA-Flag-Tet3	Addgene	60940
pCMV-6 entry	Origene	PS100001
pCpGfree-Basic	Invivogen	pcpgf-baslc
pEZX-MT06 Snai1 3'UTR	GeneCopoeia	MmiT095079
pLKO.1-TRC	Addgene	10878

3.11 PCR Amplification primers

Primer sequences used in cloning assay are listed in Table 11

Primer		Sequence
Gadd45g OE	Sense	TTAAGCGATCGCATGACTCTGGAAGAAGTCC
	Antisense	TTAAACGCGTCTCGGGAAGGGTGATGCT
Gadd45g methylation	Sense	TTAAGGATCCCAGTCTCCCAGGCTTCACTC
	Antisense	TTAAAAGCTTTGACACAGCCTCAAATCTGC
mir30d promoter	Sense	TTAAGGATCCCACACACAGGAAAAGAACTCATG
	Antisense	TTAAAAGCTTGAGTGTTTAACGTGCATGCC

3.12 Buffers and media

Buffer and media recipes prepared are listed in Table 12

Buffers	Components	Final Concentration
Nuclear preparation buffer	NaCl EDTA (pH 8) Tris (pH 7) NP-40 (v/v) Triton X-100 NaF ddH_2O	0.15 M 0.02 M 0.05 M 0.5% 1% 0.02M
Sonication buffer 1	EDTA (pH 8) Tris-HCl (pH 8) SDS ddH_2O	0.01 M 0.05M 1%
Sonication buffer 2	NaCl EDTA (pH 8) Tris-HCl (pH 8) NP-40 (v/v)	0.15 M 0.02 M 0.05 M 1%

	NaF ddH_2O	0.02 M
Dilution buffer	NaCl EDTA (pH 8) Tris-HCl (pH 8) NP-40 (v/v) NaF Sodium deoxycholate(w/v) ddH_2O	0.15 M 0.02 M 0.05 M 1% 0.02 M 0.5%
IP buffer	NaCl EDTA (pH 8) Tris-HCl (pH 8) NP-40 (v/v) NaF Sodium deoxycholate(w/v) SDS ddH_2O	0.15 M 0.02 M 0.05 M 1% 0.02 M 0.5% 0.1%
ChIP wash buffer	LiCl EDTA (pH 8) Tris-HCl (pH 8) NP-40 (v/v) NaF Sodium deoxycholate (w/v) ddH_2O	0.5 M 0.02 M 0.1 M 1% 0.02 M 1%
TE buffer	Tris-HCl (pH 8) EDTA (pH 8) ddH_2O	0.01 M 0.001 M
Mouse cardiac fibroblasts medium	DMEM (1g/L) glucose 10%FCS 1% P/S	
Primary mouse cardiac fibroblasts DMEM	DMEM (4.5g/L) glucose 20%FCS 1% P/S	
Mouse cardiac endothelial cell medium	DMEM (4.5g/L) glucose 5%FCS 1% P/S 10 mmol/L Hepes	

4 Methods

4.1 Cell culture

Human Embryonic Kidney cells (HEK293) (ATCC Manassas, Virginia, United States) and Mouse cardiac fibroblasts (MCF) (ScienCell Carlsbad, California, USA) were maintained in Dulbecco's modified eagle's medium (DMEM 1g/L glucose) supplemented with 10% fetal calf serum (FCS), penicillin (100 units/ml), and streptomycin (0.1 mg/ml).

Mouse cardiac endothelial cells were obtained from Cedarlane (Burlington, Ontario, Canada) and maintained in DMEM medium (4.5 g/L glucose, 0.584 g/L glutamine, 3.7 g/L sodium bicarbonate without sodium pyruvate) supplemented with 5% FCS, HEPES (10mmol/L), penicillin (100 units/ml), and streptomycin (0.1 mg/ml).

4.2 TGF-β1 treatment

Prior to TGF-β1 treatment, MCF and MCEC were maintained at a maximum of 90% confluency. 25,000 cells were plated in 6-well plates and starved in their respective medium (without FCS). Next day, TGF-β1 (10 ng/ml) was added, and medium was changed every two days with fresh TGF-β1. Cells were monitored for morphological changes (spindle shape/activation) as a positive control to confirm the functionality of TGF-β1.

4.3 Isolation of mouse cardiac fibroblasts

Hearts of 10–12-week-old *Tet3*$^{fl/fl}$ mice were harvested and briefly washed with ice-cold phosphate buffered saline (PBS). Hearts were cut into small pieces, resuspended in digestion buffer, and incubated for 45 min at 37°C with constant shaking. Digested tissue was then filtered through a 70 μm cell strainer followed by low-speed centrifugation (300 g, 2 min) to remove any remaining undigested tissue. The cell suspension was plated in 10 cm dishes in DMEM medium (4.5 g/L glucose) supplemented with 20% FCS and placed in a cell culture incubator at 37°C and 5% CO_2. The cells were allowed to grow to 80% confluency prior to splitting them for further use in the experiments.

4.4 AAV packaging

One day prior to virus transduction, 2.5 x 10^7 HEK293T cells were plated in a 15cm culture dish with high glucose DMEM medium supplemented with FCS and penicillin/streptomycin. Next day, cells were supplemented with high glucose DMEM medium containing only FCS at least three hours before virus transduction. For virus transduction, 7µg of AAV-DJ or AAV9 SLRSPPS plasmid, 7µg of Cre transgene plasmid, along with 20µg of helper plasmid (CB helper) were subsequently transfected using 170µl of Polyethyleneimine and 1.8 ml of OptiMEM per plate. The following day, cells were incubated in high glucose DMEM medium containing only P/S overnight. 48 hours later, the cells were harvested, and the cell pellet and medium were separated and centrifuged at 3,000 rpm. The cell pellet was then treated with cell lysis buffer and the medium was treated with 40% PEG and NaCl overnight at 4°C. The next day, the samples containing the pellet and medium were combined in a single tube and MgCl2 and benzonase were added. The samples underwent three series of freeze (80°C for 20 minutes) and thaw (37°C for 20 minutes) followed by centrifugation at 3000 rpm at 4°C and the supernatant containing the viral lysate was collected and stored at -80°C.

4.5 Virus Titer

To determine virus titer, viral genome extraction was performed by treating the viral stock with DNase I and 10x DNase buffer followed by heat treatment in a thermocycler at 37°C for 30 minutes and 95°C for 10 minutes. Then, proteinase K and DNase I were added to the tubes followed by another heat treatment in the thermocycler for an additional 15 minutes at 37°C and 10 minutes at 95°C to release the vector DNA from the AAV capsid. AAV titration was performed by quantitative real-time PCR with the primer pair listed in (Table-8). Four serial dilutions of the midi prep - plasmid DNA (10^3, 10^4, 10^5,10^6) were used to generate a standard curve for absolute quantification of viral samples. The viral vector DNA samples were tested in duplicates, and measurements were standardized to midi prep - plasmid DNA standard curve equation.

4.6 Cloning

4.6.1 Methylation reporter assay

To confirm that the methylation of the promoter downregulates the target gene expression, we employed the so called "CpG-free luciferase reporter vector". This vector is devoid of any CpG dinucleotides, and so, is optimal to study the effect of CpG promoter methylation *in vitro* (Klug & Rehli, 2006). Mouse Gadd45g and miR-30d promoter sequence were amplified by the primers listed in Table 11 using the high fidelity phusion polymerase enzyme. The primers were designed with BamHI and HindIII restriction sites in the forward and reverse strands, respectively. The thermal cycler was programmed according to standard protocols as below:

The PCR product (insert) was extracted from an agarose gel using the QIAquick Gel Extraction Kit according to the manufacturer's protocol. The pCpGfree-Lucia vector along with the extracted insert were digested with BamHI/HindIII restriction enzymes at 37°C for 3 hours (New England Biolabs, Ipswich, MA, USA). The digested products were then ligated overnight using T4 DNA ligase (Sigma-Aldrich, St. Louis, MO, USA) at 16°C. The ligated constructs were transformed via One Shot™ PIR1 chemically competent E. coli (Invitrogen, Carlsbad, CA, USA). Miniprep was performed using the Zippy Plasmid Miniprep Kit (Zymo Research, Irvine, CA, USA) following the manufacturer's protocol and confirmed via sequencing (Seq Lab UMG, Göttingen, Germany). For enhanced plasmid isolation and concentration, the Hispeed Plasmid Midi Kit (Qiagen, Hilden, Germany) was used according to the manufacturer's protocol. (Invitrogen, Carlsbad, CA, USA).

4.6.2 Overexpression of Tet3 and Gadd45g

In order to overexpress a target gene of interest, we have cloned the open reading frame of *Gadd45g* in the pCMV-6 entry mammalian expression vector (Origene). Gene specific primers were used to amplify the open reading frame of *Gadd45g* using the high fidelity phusion polymerase enzyme. The amplified PCR product contained restriction sites at the 5'- and 3'- end for the restriction enzymes AsisI and MIuI (New England Biolabs, Ipswich, MA, USA) respectively. Both pCMV-6 entry vector and the amplified inserts were digested with the mentioned restriction enzymes at 37°C for 3 hours. Ligation was performed overnight with T4 DNA ligase (Sigma-Aldrich, St. Louis, MO, USA) at 4°C. The ligated product was transformed via One Shot™ TOP10 chemically competent E. coli. To confirm correct

insertion of the respective ORFs of *Gadd45g* Miniprep, sequencing, and plasmid isolation via Midiprep were performed as previously described.

4.6.3 shRNA mediated Gm15479 gene knockdown

The shRNA construct used to knockdown *Gm15749* was previously constructed by Dr.Xingbo Xu with the use of the pLKO.1 vector (Addgene).Two shRNA oligos targeting *Gm15749* were designed with at least three single-nucleotide mismatches to unrelated genes to minimize off-target degradation.

4.7 RNA Electrophoretic mobility shift assay (EMSA)

4.7.1 RNA *in vitro* transcription

In vitro transcription of *Gm15749* was performed using the MEGAscript® Kit (Thermo fisher) according to manufacturer's protocol. Briefly, PCR amplified DNA template of *Gm15749* with T7 sequence upstream of the template was transcribed as follows:

Reaction Component	Volume
Nuclease free water	Up to 20 µl
ATP	2 µl
CTP	2 µl
GTP	2 µl
UTP	2 µl
10x reaction buffer	2 µl
PCR template	0.2 µg
Enzyme Mix	0.25 µl

Table 13: Reaction setup for RNA in vitro transcription

The reaction was incubated for 4 hours at 37°C, and RNA was purified by lithium chloride precipitation. RNA yield was assessed using a nanodrop with 1 A_{260} unit corresponding to 40 µg/ml RNA.

4.7.2 RNA Biotinylation

We have labelled the RNA by utilizing the Pierce™ RNA 3'-End Biotinylation Kit (Thermo Fisher), which adds a biotinylated cytidine (bis)phosphate nucleotide at the 3'- end of the RNA using T4 RNA ligase. Briefly, the RNA was heated at 85°C for 5 minutes, and the ligation reaction was prepared according to manufacturer's protocol. The reaction was incubated

overnight at 16°C and labelled RNA was then purified using chloroform: isoamyl alcohol, followed by sodium chloride precipitation. Labelling efficiency was determined by diluting the biotinylated RNA into a series of two-fold dilutions and testing the intensity of each by dot blot using chemiluminescence.

4.7.3 RNA EMSA

To detect RNA/protein interactions, RNA electrophoretic mobility shift assay is one the methods of choice. We have utilized the LightShift Chemiluminescent RNA EMSA kit (Thermo Fisher) to detect interaction between *Gm15749* and GADD45G, following manufacturer's protocol. First, a pre-run of the DNA retardation gel (6%) was performed in 0.5x TBE buffer solution in the electrophoresis apparatus for 60 minutes at 100V. After several optimization experiments, the binding reactions were prepared in the order below:

Component	**Final Amount**	**Reaction**			
		1	**2**	**3**	**4**
Ultrapure Water	Up to 20 µL	-	-	-	-
10X Binding Buffer (µL)	1x	2 µL	2 µL	2 µL	2 µL
50% Glycerol	5%	2 µL	2 µL	2 µL	2 µL
500mM DTT	25mM	1 µL	1 µL	1 µL	1 µL
2M KCL	0.1M	1 µL	1 µL	1 µL	1 µL
1M MgCl2	0.05M	1 µL	1 µL	1 µL	1 µL
tRNA (10mg/mL)	5 µg	1 µL	1 µL	1 µL	1 µL
Unlabeled *Gm15749*	1 µM	----	----	2 µL	2 µL
GADD45g protein	4 µg	----	4 µg	4 µg	4 µg
Biotin labelled *Gm15749*	2-4nM	2nM	2nM	4nM	2nM

Table 14: Reaction setup for EMSA assay

The reaction was incubated for 30 mins at room temperature, followed by addition of 5x loading buffer. The samples were loaded onto the DNA retardation gel and electrophoresed for 45 minutes at 100V. This was followed by transfer on a presoaked nylon membrane (in 0.5X TBE) at 400 mA for 30 minutes. The membrane was then cross-linked using a UV-light bulb for 60 seconds on each side and blocked with the nucleic-acid blocking buffer. To visualize biotin-labelled RNA, the conjugate solution containing stabilized streptavidin-horseradish peroxidase was added to the membrane and incubated at room temperature for 15

minutes with gentle shaking. The membrane was then further washed and incubated with the substrate working solution for 5 minutes to allow the visualization of the chemiluminescent signal. The membrane was visualized using the ChemiDoc MP imagine system.

4.8 RNA Immunoprecipitation (RIP)

To confirm binding of RNA to a specific target protein, we used the RNA immunoprecipitation kit Magna Rip (Sigma Aldrich) following manufacturer's protocol. Briefly MCFs were lysed using the RIP lysis buffer, and antibody (GADD45g) along with magnetic beads were added to the lysate and incubated at 4°C overnight with rotation. The next day, RNA was purified with magnetic beads using a magnetic separator and multiple steps of washing using RIP wash buffer. Immunoprecipitated RNA was then analyzed by qRT-PCR to detect presence of interacting RNAs with specific primers (*Gm15749*).

4.9 DNA RNA Immunoprecipitation (DRIP)

DNA RNA immunoprecipitation was utilized to confirm the formation of R-loops at certain regions of interest. The method utilizes s9.6 antibody which pertains high specificity and sensitivity to bind to DNA: RNA hybrid structures in their native chromosomal context (Z. Hu et al., 2006). In brief, cells were briefly washed in ice cold PBS and then fixed with 1% formaldehyde. The samples were quenched with 1.25M glycine and then lysed using the nuclear preparation buffer listed in Table 12. For target validation of R-loops, control samples were treated with RNaseH at 37°C for 20 mins. The samples were then sonicated for 15 minutes at 50 Amplitude (30 sec on/off). The samples were incubated overnight with s9.6 or mouse IgG antibody in IP buffer containing protein G sepharose beads at 4°C. The next day, the samples were washed using the wash buffers listed in Table 12. The collected samples were treated with proteinase K (20 ng, 15 mins, 56°C) and DNA was purified and analyzed by qRT-PCR.

4.10 Co-immunoprecipitation (Co-IP)

Co-IP is the standard method used to confirm the interaction between two target proteins. The assay is based on the use of protein-specific antibodies to "pull-down" and indirectly identify the possible interacting proteins. Co-IP was performed using the Immunoprecipitation Kit protein G (Roche) following the manufacturers protocol. Briefly, cells were lysed with 1 ml

of lysis buffer/wash buffer-1 supplemented with protease (Roche) and phosphatase (Sigma) inhibitors for 1 hour on ice with regular vortexing. The lysate was then centrifuged at 12,000xg for 10 mins at 4°C and the supernatant was collected and incubated with Protein A/G agarose beads as a preclearing step for 1 hour at 4°C. After preclearing, the lysates were incubated with the antibodies against TET3, GADD45G, and IgG listed in Table 4. The next day, the complex was washed with wash buffer 2 and 3, and the pellet was collected and mixed with 2x Nupage LDS protein loading dye (Thermofischer). The captured proteins were then denatured at 95°C for 5 mins prior to SDS-polyacrylamide gel electrophoresis.

4.11 Western Blot

Cells were lysed with RIPA buffer supplemented with protease (Roche, Switzerland) and phosphatase inhibitors (Sigma-Aldrich, USA) and incubated on ice for 60 mins with frequent vortexing. This was followed by sonication (40 Amp, 15 sec on/off) and centrifugation (13,000 rpm for 15 min at 4°C). The supernatant was collected and mixed with NuPAGE LDS buffer. Protein samples were loaded on a NuPAGE 4-12% Bis/Tris Gel (Novex, Newbedford, USA), together with the Novex Sharp Pre-stained Protein Standard (Invitrogen, USA). Transfer of protein was performed using a PVDF membrane which was briefly activated with methanol. The procedure was carried out at 68 mA for 80 min. The membrane was then blocked with 8% BSA in TBST for 1h at RT followed by incubation with the primary antibody (diluted in 5% BSA in TBST) (listed in table 4) at 4°C overnight. The next day, the membrane was washed 3 times with 1xTBST and a secondary antibody (listed in table 5) was added for 1h at RT. Three additional washing steps with 1xTBST were done to remove unspecific binding along with a single PBS washing step. Proteins were detected using the chemiluminescent substrates 20X LumiGLO and 20X Peroxide in 1:1 ratio (Cell Signaling, Danvers, MA ,USA) were added to the membrane and visualized using the ChemiDoc XRS imager and Image Lab software (Bio-Rad, Hercules, CA, USA).

4.12 Animal Procedures

4.12.1 Animal ethics

All procedures regarding animal handling and experiments were conducted in accordance with German animal protection laws and were approved by the responsible governmental authority

(Niedersächsisches Landesamt für Verbraucherschutz und Lebensmittelsicherheit; animal protocol number 33.9-42502-04-19/3286).

4.12.2 Tet3 flox mouse model

In order to study the role of a gene in a specific cell subtype, the Cre-lox system is the preferred technology of choice. Cre-lox is a site-specific recombinase technology used to delete specific sequences of interest at sites on the DNA level. Lox describes the addition of two loxP sequences (Locus of X over P1 found in bacteriophage) flanking a critical exon of interest. LoxP sites are specifically recognized and cleaved by the Cre recombinase enzyme, which is a tyrosine kinase enzyme derived from bacteriophage P1.

C57BL/6J-Tet3 tm1.1Smoc were purchased from Shanghai Model Organisms. Briefly, loxP sites were inserted in the same orientation flanking exon 4 of the mouse *Tet3* gene (ENSMUST00000089622.10). When crossed with a Cre-recombinase expressing strain, site specific recombination will occur resulting in the deletion of the DNA sequence between the two loxP sites.

4.12.3 Endothelial-specific Cre recombinase

VE-Cadherin-Cre (B6.FVB-Tg(Cdh5-cre)7Mlia/J) was purchased from The Jackson Laborotary. The transgenic mouse line was generated by addition of Cre-recombinase under control of VE-Cadherin promoter (Alva et al., 2006). Once bred with a mouse line containing loxP sites flanking a sequence of interest, site specific Cre-recombination occurs resulting in the deletion of the sequence flanked.

4.12.4 Fluorescence activated sorting of cardiac endothelial cells

In order to confirm specific deletion of *Tet3* in cardiac endothelial cells and assess the knockout efficiency, endothelial cells were isolated from heart tissue samples. Mice were sacrificed as described and the heart samples were collected and placed in ice-cold PBS, followed by DMEM medium. Heart tissue dissociation was performed using the tumor dissociation kit (Miltenyi Biotec, Germany). Briefly, the collected hearts were cut into small pieces of 2-4 mm in size and incubated with the enzymes mix supplied. The tissue was dissociated using the program 37C_Multi_G using the gentleMACS Octo Dissociator. The

cell suspension was then passed through a 70μm strainer and washed with DMEM followed by FACS buffer. The cell pellet was then resuspended with red blood cell lysis buffer to remove remnant blood cells. The cells were then incubated with Alexa 647 CD-144 antibody in FACS buffer (1:100) for 1 hour at 4 °C in the dark. FACS sorting was performed using the FACS atria cell sorter II. The sorted cells were divided into two populations, CD-144+ and CD-144-, and were analyzed for mRNA expression using the aforementioned protocol.

4.12.5 Application of angiotensin II via osmotic minipump implantation.

Preparation of angiotensin II

Around 1.2 mg (per mouse) of lyophilized Angiotensin II (sigma) was dissolved in sterile PBS to yield a concentration of angiotensin application of 1.5mg/kg/day. The angiotensin solution was carefully added to the osmotic minipump, and the pumps were then placed in a falcon containing sterile sodium chloride solution. The stored pumps were kept at 37°C for around 2 days prior to surgery.

Procedure

10–12-week-old mice were subjected to angiotensin II mini-pump implantation via subcutaneous insertion. Briefly, the mice were anesthetized with 2% (vol / vol) isoflurane in oxygen (1 l / min) through a nasal mask. The body temperature was maintained by using a warm pad, and the mice were carefully monitored to confirm proper anesthesia induction by checking response to pain stimulus. The skin was prepped by proper disinfection and hair removal of the surgical site. This was followed by a small incision (around 1 cm) performed over the shoulder blade of the front leg and perpendicular to the mouse tail. A hemostat was then used to make a subcutaneous tunnel and create a pocket for the pump. The pump was then inserted, and the wound was closed using surgical sutures. The mice received carprofen (5mg/kg) during surgery and 3 days following surgery. The mice were also monitored for 3 days for any signs of distress, dehydration, or weight loss.

All the mice analyzed in the experiments in this thesis were sacrificed at around 14-16 weeks of age. Following brief administration of isoflurane, the mice were weighed and then sacrificed by cervical dislocation. The chest was then opened, and the heart was removed from the thoracic cavity, briefly washed with sterile PBS, and weighed. Heparin was added to the blood,

which was collected from the thoracic cavity and placed in an Eppendorf tube. Transverse cuts of the heart were made from the upper and lower parts of the heart to yield a "doughnut-like shape" which was placed in a cassette in 4% paraformaldehyde solution along with the rest of the collected organs. The base section of the heart along with other organs collected were directly snap-frozen in prelabelled cryo-tubes in liquid nitrogen for RNA and protein analysis.

4.12.6 Echocardiography

In order to assess the heart function, echocardiography was performed on the mice prior to surgery (pre-echo) and 1 day before sacrifice (post-echo). Echocardiographic measurements as well as data analysis were kindly performed by the technical staff of the department of Pharmacology and Toxicology in the university medical center as part of service offer. The staff were blinded throughout all the measurements.

4.13 Genomic DNA isolation from heart and tail

Genomic DNA was isolated from tail samples of mice (around 3-4 weeks of age). The tissue was lysed overnight in a thermomixer at 56°C with shaking using the DirectPCR Lysis Reagent (Qiagen). Next day the tissue was incubated at 85°C for 45 minutes, and the obtained DNA from the lysate was then used for genotyping PCR. DNA isolated from DNA was used for the primary genotyping PCR of the newly born mice.

DNA isolation from heart tissue was performed using the Qiagen DNeasy Blood and Tissue isolation kit (Qiagen). Isolated DNA was then quantified using the nanodrop and used for genotyping purposes, which will be described below.

4.14 TET3 floxed allele PCR detection

In order to confirm presence of floxed alleles, primers were designed by shanghai model organisms up and downstream of each lox P site. Presence of loxP is indicated by a larger PCR product (370 bp) than a normal allele (221 bp).

The protocol of the PCR reaction was as follows:

Reaction Component	Volume
Genomic DNA	100 ng
Tet3 Forward primer (10μM)	2.5 μL

Tet3 Reverse primer (10µM)	2.5 µL
dNTP Mix (2.5 mM each)	2.5 µL
DMSO	1.5 µL
MgCl2	2.5 µL
10x Taq Buffer	6.25 µL
Taq Polymerase	0.25 µL
Nuclease free water	Up to 25 µL

Table 15: Reaction setup for Tet3 flox PCR detection reaction

The thermocycler was set with the following cycler conditions

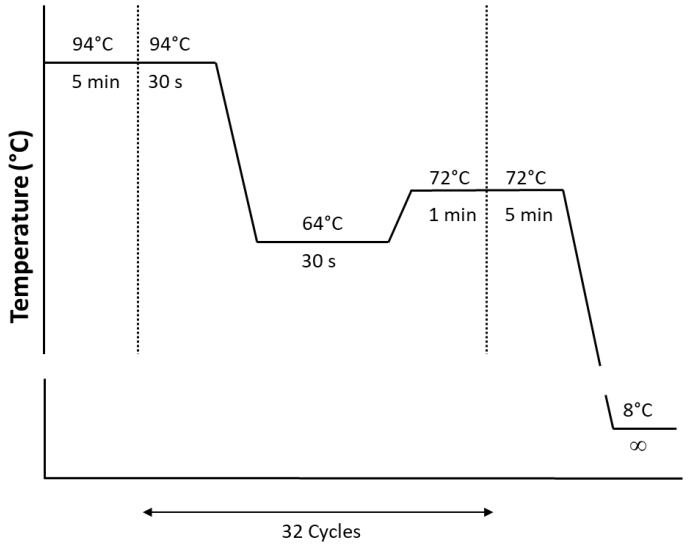

Figure 5: Temperature Cycler conditions during Tet3 genotyping PCR

4.15 Cdh5 Cre PCR detection

To detect the presence of Cre recombinase, we have followed the protocol provided by the Jackson Laboratory (Protocol 22392). The primers listed in Table 9 were used to amplify the *Cre* transgene at 500 bp as well as an internal control product (7338-7339) with the size of 324 bp.

4.16 Homologous Recombination confirmation

DNA from mouse heart was screened by long range PCR to validate successful homologous recombination. Primers provided by shanghai model organisms were designed such that one primer is located outside the homology arm region and the other is unique to the targeting vector used.

The protocol of the PCR reaction was as follows:

Reaction Component	Volume
Genomic DNA	100 ng
5x PrimeStar GXL Buffer	4 µl
2.5 mM dNTP	2 µl
Primer I (10pmol/ul)	0.4 µl
Primer II (10pmol/ul)	0.4 µl
PrimeStar GXL DNA Polymerase	0.8 µl
Nuclease free water	Up to 20 µl

Table 16: Reaction setup for long range PCR homologous recombination

The thermocycler was set with the following cycler conditions:

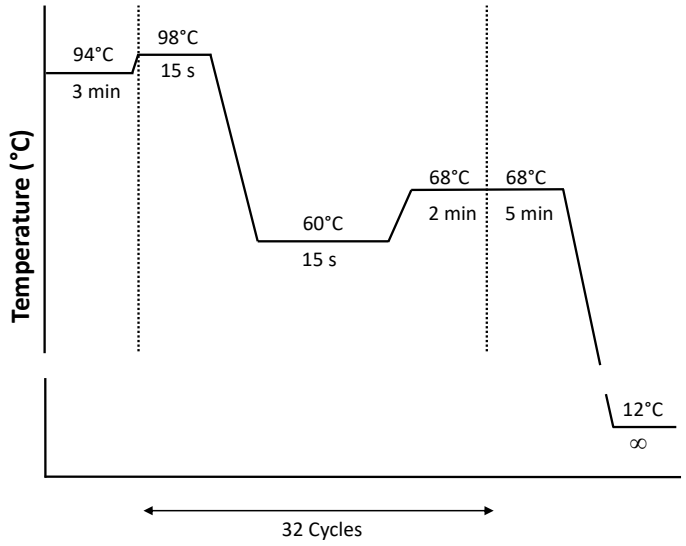

Figure 6: Temperature Cycler conditions during homologous recombination PCR

4.17 Detection of deleted allele

PCR amplification from isolated DNA was performed with primer pair P7-P8 to identify the presence of the knockout band. The expected amplicon sizes were as follows: 1228 bp (floxed allele) and 310 bp (knockout band). The thermocycler conditions were set as depicted in Figure 7. The resulting PCR products were analyzed by gel electrophoresis with 1% agarose DNA gel.

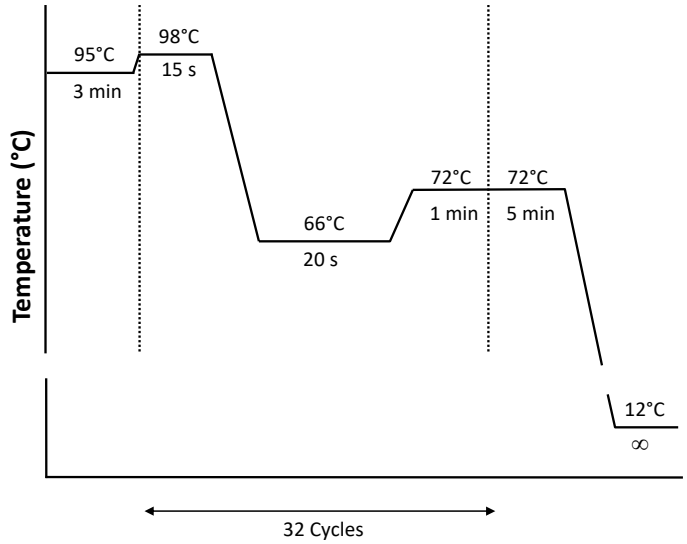

Figure 7: Temperature Cycler conditions during the PCR used to assess gene knockout.

4.18 Histology

4.18.1 Tissue preparation

All tissue preparations procedures were kindly performed by the technical assistance staff of our research group.

After sacrificing the mice, organs were placed in pre-labelled cassettes in 4% aqueous formaldehyde solution for around 5 days. Next, the samples were thoroughly washed with running tap water to remove any remnant formaldehyde solution. The samples were then placed in the Leica tissue infiltration system to be dehydrated via increasing ethanol gradient concentrations (1.5 h: 1 x 50%, 1 x 70%, 1 x 80%, 2 x 95%, 2 x 100%). The tissue was then placed in xylene twice for 1 hour each time. Finally, tissue was embedded with melted paraffin wax (3x 1h each), and the tissue block was then allowed to cool down on a cooling plate for at least 24 hours before use.

4.18.2 Sectioning and deparaffinization

Paraffin blocks were cut into 5 µm thick slices using a rotary microtome. Heart sections were obtained by cutting the tissue into 5 levels (deep) for fibrosis analysis. The sections were mounted on SuperFrost slides and placed in a 37°C oven overnight to allow the tissue to dry prior to staining. All tissue sections were deparaffinized prior to any histological staining.

Deparaffinization protocol:

- 2 x 10 mins Xylol
- 2x 5 mins 100% ethanol
- 1x 5 mins 95% ethanol
- 1x 5 mins 80% ethanol
- 1x 5 mins 70% ethanol
- 1x 5 mins 50% ethanol
- 1x 5 mins 30% ethanol
- 1x 5 mins distilled H_2O

4.18.3 Picrosirius Red Staining

Picrosirius red staining is a common histological assay to visualize collagen in paraffin-embedded tissue sections and quantify fibrosis (Junqueira et al., 1979). Following deparaffinization, the tissue sections were placed in picrosirius red solution for 45 minutes. The slides were then washed with diluted acetic acid solution for 2 minutes. This was followed by dehydration of the slides in EtOH 96%, EtOH 100%, and xylene. The slides were then mounted with entellan and a coverslip and allowed to dry overnight before visualization.

4.18.4 Acquisition of pictures

5 tissue sections were analyzed per heart sample (different levels), and at least 10 representative pictures of the left ventricle were taken per section using the Olympus BX43 light microscope.

4.18.5 Analysis of pictures

Red stained fibrotic area was measured using the Olympus CellSens imaging software.

4.18.6 Hematoxylin and Eosin (HE) Staining

Hematoxylin is the most common nuclear stain which gives the nucleus a distinct shade of purplish blue. The actual staining component is the oxidized form of hematoxylin known as hematein. Eosin Y, which is an acidic dye, stains the acidophilic cellular components such as the cytoplasm pink.

Protocol

After deparaffinization and rehydration of the tissue, the slides were submerged in Mayer's Hemalum solution for 6 minutes. To conserve the blue dye staining, the slides were washed with running tap water for 10 minutes. The tissue sections were then incubated with Eosin Y (pH 5) for 2 minutes, followed by 3 washings with distilled water. The histological sections were then dehydrated with 96% ethanol and 100 % ethanol and xylol. The slides were then mounted with entellan and allowed to dry overnight.

4.18.7 Immunofluorescence

Immunofluorescence (Cells)

Actin filaments were stained in cells cultured in 4-well chamber slides using the Phalloidin iFluor 488 reagent (Abcam, United Kingdom) according to the manufacturer's protocol. Briefly, medium was was aspirated from the cells, followed by washing the cells in PBS. The cells were then fixed with 4% formalin solution for 30 minutes and permeabilized with 0.1% Triton-X-100 in PBS for 5 minutes at room temperature. 100 µl of 1x phalloidin conjugate was added to the cells for 1 hour at room temperature. DAPI stain was then added (1:500 in PBS) and the cells were gently rinsed prior to adding mounting media (Immu-Mount, Epredia).

Immunofluorescence (Tissue)

The tissue was first deparaffinized as explained before and slides were submerged with target retrieval citrate buffer solution (Dako, Germany) using a rice cooker steamer for 45 minutes. The slides were allowed to cool on ice and then washed with PBS. The tissue was then blocked with 1% BSA in PBS for 30 minutes at room temperature. The slides were then incubated with the primary antibody listed in Table 4 overnight in a humidified dark chamber at 4°C. The next day, slides were washed with PBS and then incubated with species specific conjugated secondary antibody listed in Table 5 for 45 minutes at room temperature. The nucleus was stained using DAPI (1:500) solution for 10 minutes at room temperature, and the slides were further washed with PBS prior to adding mounting media (Immu-Mount, Epredia). and covering the slides with a coverslip.

Stained slides were left in a dark chamber for two days at 4°C prior to imaging analysis.

4.19 miRNA and RNA isolation

miRNA and RNA isolation from cells and heart tissue was performed using the miRNeasy kit (Qiagen) or the PureLink RNA isolation kit (Invitrogen, USA) according to the manufacturer's protocol. Briefly, 5 mg tissue from left ventricle was weighed and excised. 700 µl of QIAzol lysis reagent was added into a prechilled 2 ml Eppendorf tube containing a metallic bead. The samples were placed in a tissue, lysed, and homogenized for 5 minutes. 140 µl of chloroform was added to the samples prior to centrifugation at 13,000 rpm for 15 minutes at 4°C. RNA was collected from the upper aqueous phase and mixed with 100% absolute ethanol and then placed in the RNeasy mini spin column and centrifuged at 10,000 rpm for 15 seconds. The samples in the column were washed in the provided wash buffers in the kit and purified RNA was eluted in 14 µl of RNase free water.

4.20 miRNA polyadenylation and reverse transcription

Reverse transcription was performed using the miRCURY LNA Sybr Green PCR Kit (Qiagen, Germany) according to manufacturer's protocol. Polyadenylation and reverse transcription of miRNA is achieved by the poly(A) polymerase enzyme oligo-dT primers, respectively. The UniSp6 spike-in control is used as an internal control for proper cDNA synthesis. A 10 µl total reaction was set up as the following:

Component	Volume
5x miRCURY SYBR Green RT Reaction Buffer	2 µl
RNase free water	4.5 µl
10x miRCURY RT Enzyme Mix	1 µl
UniSp6 RNA spike-in	0.5 µl
RNA (5ng/µl)	2 µl

Table 17: Reaction setup for miRNA reverse transcription reaction

The samples were mixed thoroughly and incubated for 60 minutes at 42°C followed by incubation for 5 minutes at 95°C to heat inactivate reverse transcriptase enzyme. The reaction was immediately cooled at 4°C before proceeding with real-time PCR.

4.21 Real time PCR

4.21.1 miRNA Gene expression analysis

The reaction setup to detect miRNA expression followed the manufacturer's protocol:

Component	Volume
2x miRCURY SYBR Green RT Master Mix	5 µl
RNase free water	0.5 µl
Primer mix	1 µl
cDNA template (1:60)	3 µl
ROX Reference Dye	0.5 µl

Table 18: miRNA qRT-PCR reaction setup

The cycler conditions to detect miRNA expression were as follows:

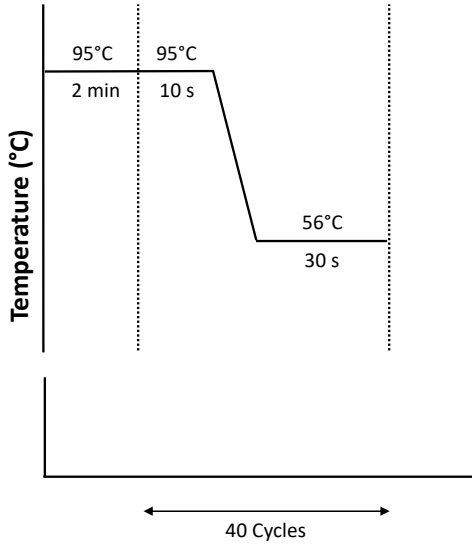

Figure 8: Temperature Cycler conditions to assess miRNA gene expression

4.21.2 mRNA Gene expression analysis

For mRNA gene expression analysis, the qRT-PCR setup involved an initial denaturation step at 95°C for 10 mins, followed by 40 cycles of denaturation at 95°C for 15 sec, and annealing/extension at 60°C for 30 sec. The setup was performed on a StepOne Plus real time PCR system machine (Life Technologies) with a final volume of 20 µl. The measurements were standardized to GAPDH using ΔΔCt methods.

4.22 Statistical Analysis

Statistical analysis was conducted using GraphPad Prism software (Version 8.0.2). All data are presented as mean ± SEM and represent a minimum of three independent experiments. Statistical analysis was performed using an unpaired t-test or one-way analysis of variance (ANOVA), followed by Tukey's post-hoc analysis for multiple comparisons. Differences between groups were considered significant when the p-value was <0.05.

Results

5 Endothelial *Tet3* regulates EndMT by demethylating miR-30d precursor gene

5.1 Generation of endothelial-specific knockout of *Tet3*

5.1.1 Generation and validation of *Tet3* flox strategy

The transgenic mice purchased from Shanghai Model Organisms possess loxP sites flanking exon 4 of the *Tet3* gene (ENSMUST00000089622.10). The mouse line was developed using a targeting vector designed to contain a single loxP site upstream of exon 4 and a loxP-flanked neomycin resistance cassette downstream of exon 4 of *Tet3*. The company provided C57BL/6J Smoc-Tet3tm1.1Smoc ($Tet3^{fl/fl}$) cryopreserved embryos (Figure 9-A). After implantation of the cryopreserved embryos into surrogate pseudo-pregnant C57BL/6J female mice, offspring born were genotyped for the presence of the floxed allele using the primer pair (P5-P6) supplied by the company that can amplify the 3'loxP site of exon 4 (Figure 9-B). PCR amplification using this primer pair produced a larger band (370 bp) for the floxed allele and a smaller band (221 bp) for the wild-type allele. One band at 221 bp indicates that the mice carry no floxed allele (Wildype: $Tet3^{+/+}$), and two bands indicate that the mice are heterozygous flox ($Tet3^{flox/+}$). One band at 370 bp indicates that both *Tet3* alleles are flanked by loxP sites (Homozygous: $Tet3^{fl/fl}$) (Figure 9-B). The resulting $Tet3^{fl/fl}$ mice were bred with C57BL/6J for at least 10 generations prior to use in the experiments. Moreover, we isolated DNA from the mouse tail and heart tissues and performed Sanger sequencing analysis (Microsynth) using the primer pair (P7-P8), which was designed to amplify the sequence flanked by both loxP sites. Sequencing analysis confirmed the presence of two loxP sequences flanking exon 4 of *Tet3* (Figure 9-C). Taken together, these results confirmed the correct placement of the loxP sequence flanking exon 4 of the *Tet3* gene.

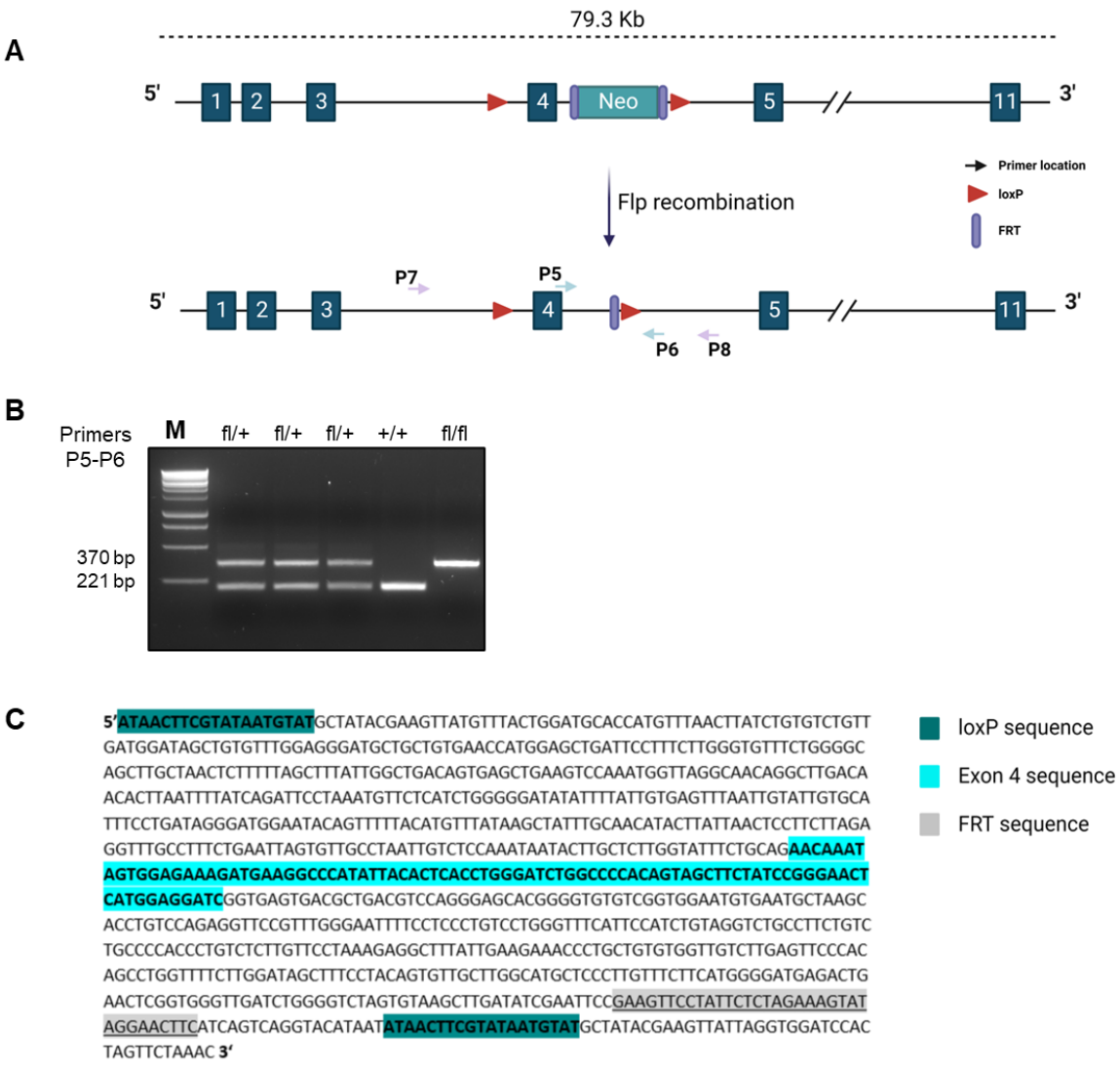

Figure 9: Genotyping PCR to validate the *Tet3*$^{fl/fl}$ mouse model. (A) Schematic diagram of the exons of *Tet3* gene showing the strategy used to insert loxP sequences flanking exon 4. A targeting vector composed of a neomycin resistance cassette flanked by the FRT and loxP sequences was electroporated into embryonic stem cells to introduce loxP sites specifically to the *Tet3* allele. Upon addition of flippase recombinase (FLP), site-specific recombination occurs, resulting in the removal of the neomycin resistance cassette to produce the C57BL/6JSmoc-Tet3tm1.1Smoc mouse model. Arrows indicate primer location and orientation, the red triangle indicates the loxP sites, and the purple segment represents FRT sites. **(B)** 2% agarose gel of the genotyping PCR amplicons of the DNA isolated from mouse tail tissue using the primer pair P5-P6 that produces a product of 370 bp for the floxed allele and 221 bp for the wild-type allele**.** The two-band pattern identifies a heterozygous mouse (lanes 1,2.3). A single-band pattern at 221 bp indicates a wild-type mouse (lane 4), and a single-band pattern at 370 bp identified a homozygous floxed mouse (lane 5). **(C)** Sanger sequencing results validating the presence of loxP sequences at both the 5' and 3' sites flanking exon 4 of the *Tet3* gene. M, DNA molecular size marker. The schematic was created using Biorender.com.

5.1.2 Validation of homologous recombination

To validate the correct homologous recombination and site-specific integration of the targeting vector into the *Tet3* locus, we performed long-range PCR with primer pairs (I-II) and (III-IV) (Figure 10-A). The targeting vector contained both 5' and 3' homology arms for the *Tet3* gene to ensure site specific recombination as well as proper orientation. The primer pairs were designed in such a way that they would both yield both a smaller PCR amplicon size after correct recombination and integration of the targeting vector (5.2 kb and 4.3 kb respectively) in comparison to a wild type allele (9.4 kb and 9.2 kb respectively) (Figure 10-B).

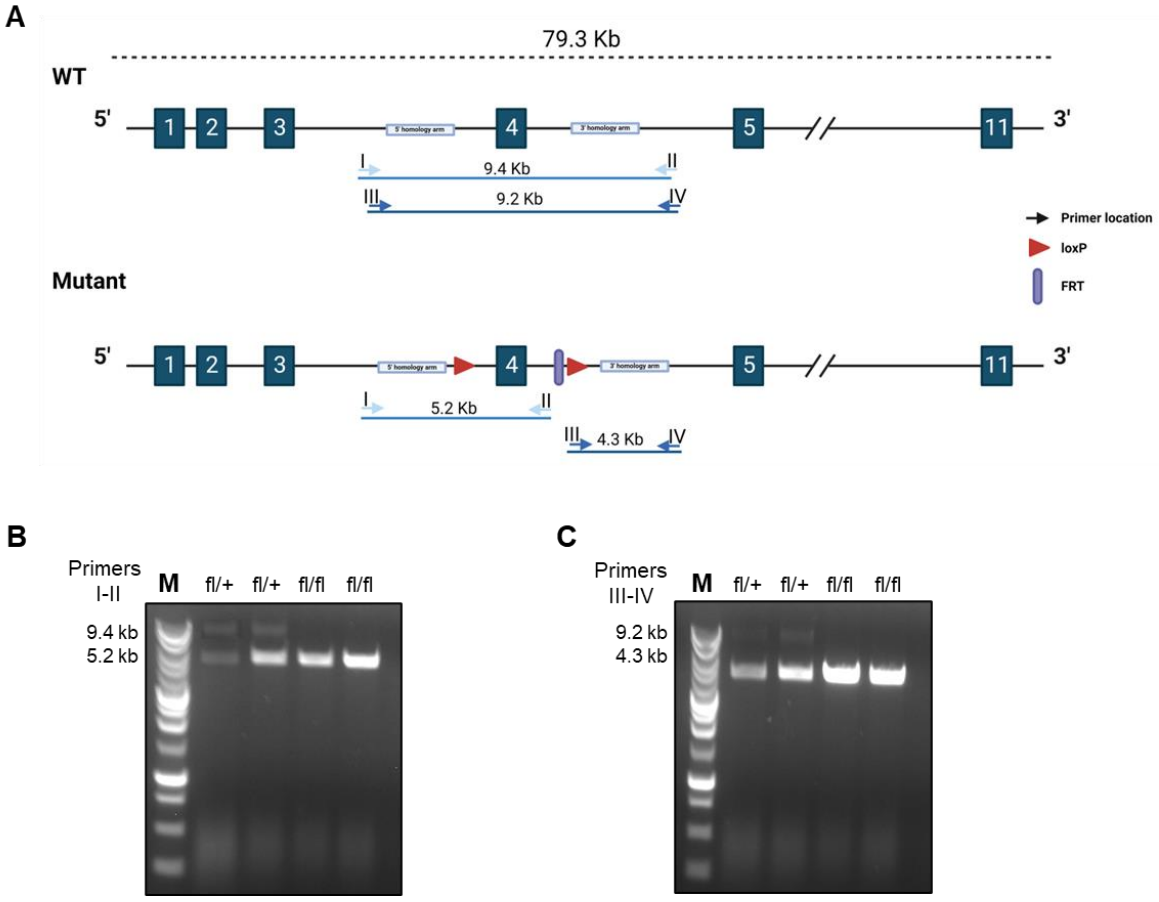

Figure 10: Long range PCR to confirm proper homologous recombination. (A) Schematic drawings of the wild-type and targeted loci of the *Tet3* allele. Arrows indicate primer location and orientation, and the red triangle indicates the loxP site. **(B-C)** Long range PCR analysis for correct homologous recombination of isolated genomic DNA from $Tet3^{fl/fl}$ and $Tet3^{flox/+}$ mice with primer pairs (I-II) and (III-IV). Amplicon products of 9.4 kb and 9.2 kb generated from PCR amplification using primers (I-II) and (III-IV), respectively, indicating a wild-type allele. The expected amplicon products of 5.2 kb and 4.3kb generated from PCR amplification using primers (I-II) and (III-IV),

respectively, confirm correct homologous recombination in the *Tet3* locus. M, DNA molecular size marker. The schematic was created using Biorender.com

5.1.3 Validation of *Tet3* knockout *in vitro*

Since the *Tet3*$^{fl/fl}$ mouse model has not been used and characterized yet, we wanted to confirm whether the addition of Cre recombinase would result in the site-specific recombination of the loxP sequence and splicing of the flanked region. As such, we opted to first utilize an *in vitro* model whereby we isolated cardiac fibroblasts from *Tet3*$^{fl/fl}$ mice using a well-established protocol, as described in section 4.3. The isolated fibroblasts were transduced with a plasmid, which expresses Cre recombinase under the CMV promoter packaged into AAV virus as explained in section 4.4 (Figure 11-A). To ensure proper transduction efficiency, we utilized either AAV-DJ serotype known for its high transduction efficiency in hard-to-transduce cell lines or AAV-SLRSPPS, a modified AAV-9 serotype known to transduce fibroblasts and endothelial cells efficiently (Varadi et al., 2012). 48 hours post transduction, genomic DNA was isolated from the cells and a PCR reaction was prepared using the primer pairs (P7-P8) which can amplify the region including both loxP sites along with exon 4 of *Tet3* gene (Figure 11-A). Deletion of exon 4 would result in a smaller amplicon size of around 310 bp. AAV-transduced cells revealed two bands consisting of a 1228 bp amplicon (floxed allele) and a 310 bp excised band (Figure 11-B), indicating successful Cre recombination and deletion of exon 4 in comparison with untransduced cells, which showed only one band at 1228 bp (Figure 11-C).

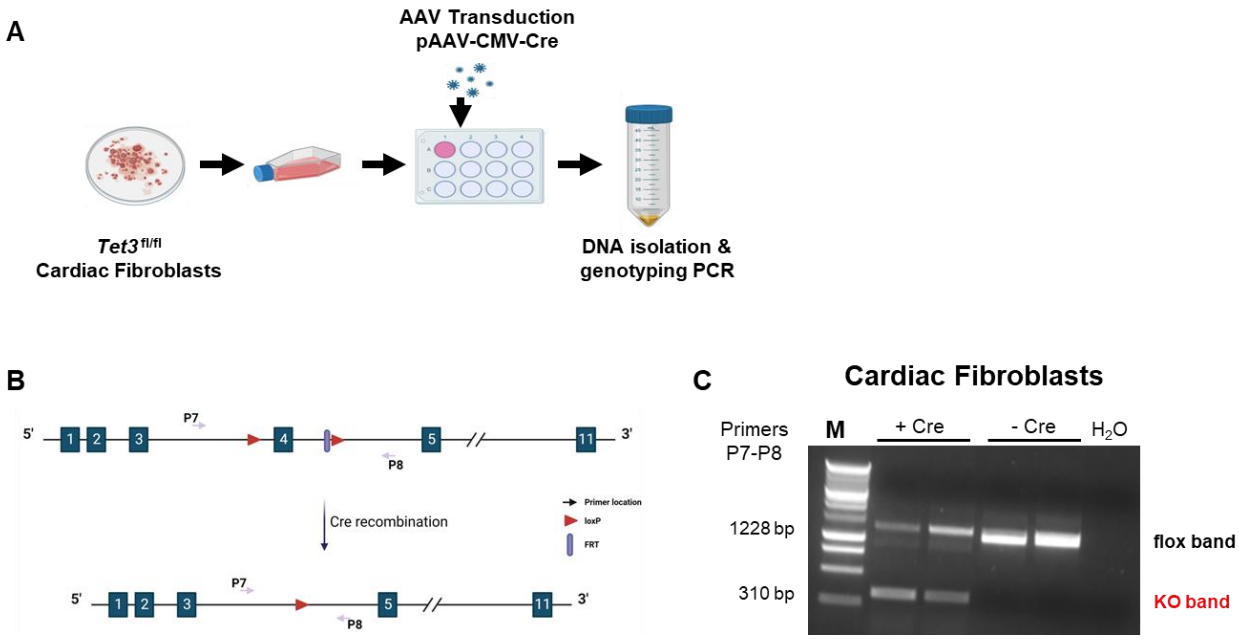

Figure 11: *In vitro* validation of *Tet3* knockout (A) Schematic showing the experimental overview of the model used to validate *Tet3* knockout. Fresh heart tissue was used to isolate cardiac fibroblasts from *Tet3* $^{fl/fl}$ mice. The cells were allowed to grow, and once confluent, were plated in a 6- well plate for virus transduction. The cells were transduced with 100,000 MOI dose of AAV (either AAV-DJ or AAV-SLRSPPS serotype) containing pAAV-CMV-Cre. 48 hours after transduction, the cells were collected, and DNA was isolated for genotyping PCR. **(B)** Schematic representation of *Tet3* floxed allele with loxP sites flanking exon 4 and primers P7-P8 are designated in the graphic. In the case of Cre recombination, the sequence between the two loxP sites (red triangles) is deleted, yielding a delta allele that can be detected by PCR using primers 7 and 8. **(C)** 2% agarose gel from the PCR amplification of either AAV-transduced or untransduced cells. Cells transduced with AAV-DJ (first lane) or AAV-SLRSPPS revealed two bands on the agarose gel, corresponding to the floxed allele at 1228 bp and the knockout band at 310 bp. Non-transduced cells showed a single intense band corresponding to the floxed allele. Water was run in parallel as an internal negative control for the PCR reaction. M, DNA molecular size marker. The schematic was created using Biorender.com

5.1.4 Generation of endothelial specific *Tet3* knockout mouse line

Previous studies have highlighted the protective role of TET3 in fibrosis (Tampe et al., 2014, 2015). In the heart, TET3 is primarily expressed in endothelial cells and fibroblasts (Thul et al., 2017). Due to the contribution of endothelial cells to the myofibroblast population by EndMT in pathological conditions, we generated an endothelial specific *Tet3* knockout mouse model to further understand the role of TET3 in this cell population and its possible regulatory effects on EndMT and cardiac remodeling. As such, we crossed *Tet3*$^{fl/fl}$ mice with a commercially available transgenic mouse line (Jackson Laboratories) that expresses Cre recombinase under the control of the *Cdh5* promoter (VE-Cadherin; Vascular endothelial

cadherin), as mentioned in section 4.11.3. We evaluated the number of offspring generated from each mating to ensure that there was no disruption in the breeding pattern with the use of both transgenic mouse lines. Mating of *Tet3*$^{fl/fl}$ mice with *Cdh5*$^{Cre+}$ mice produced a total of 46 offspring (Figure 12-A). The mice litter produced followed the expected genotype distribution, with almost half of the litter having the *Tet3*$^{fl/+}$*; Cdh5*$^{Cre+}$ genotype and the other half having the *Tet3*$^{fl/+}$*; Cdh5*$^{Cre-}$ genotype (Figure 12-A). Moreover, we observed almost identical sex distribution among the litters produced, with no apparent difference between the sexes with both genotypes produced (Figure 12-B). The F2 generation, which was generated by crossing *Tet3*$^{fl/+}$*; Cdh5*$^{Cre+}$ mice with *Tet3*$^{fl/fl}$ mice, also yielded similar genotype distribution patterns as expected, following the Mendelian inheritance pattern. Of the 68 mouse pups generated, four different genotypes were produced, each comprising almost 25% of the total litter (Figure 12-C).

1. 25% *Tet3*$^{fl/fl}$*; Cdh5*$^{Cre+}$
2. 23% *Tet3*$^{fl/fl}$*; Cdh5*$^{Cre-}$
3. 26% *Tet3*$^{fl/+}$*; Cdh5*$^{Cre+}$
4. 26% *Tet3*$^{fl/-}$*; Cdh5*$^{Cre-}$

All of the matings performed in the project were also closely monitored for any physical abnormalities in collaboration with the European Neuroscience Institute Göttingen (ENI), where the mice were kept until use in experiments.

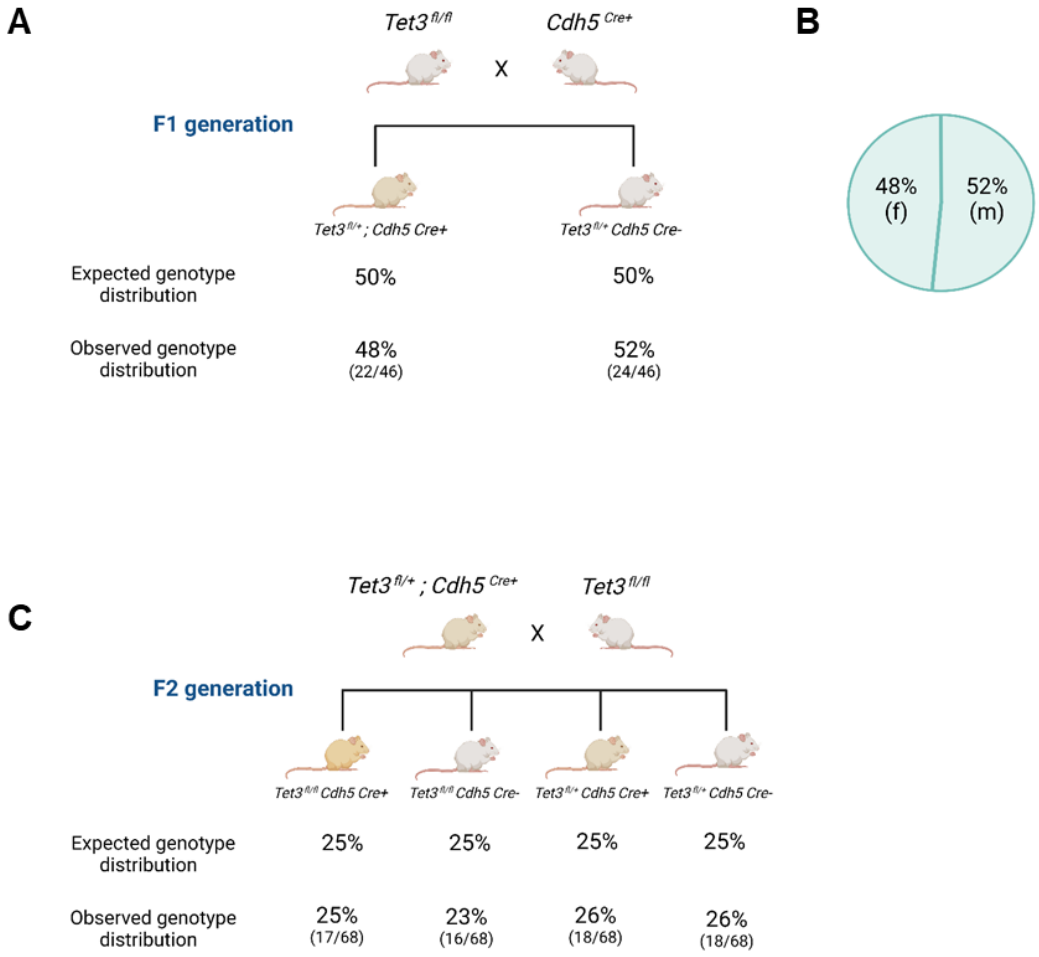

Figure 12: Breeding plan to generate *Tet3$^{fl/fl}$; Cdh5^{Cre+}* transgenic mice. Schematic showing the breeding plan used to generate the transgenic mouse line. **(A)** *Tet3$^{fl/fl}$* mice were bred with *Cdh5^{Cre+}* mice to produce the F1 generation. **(B)** Pie chart showing the sex distribution in the litters produced **(C)** *Tet3$^{fl/+}$; Cdh5^{Cre+}* mice from the F1 generation were bred with *Tet3$^{fl/fl}$* to generate *Tet3$^{fl/fl}$; Cdh5^{Cre+}* which was used in the following experiments. The mouse litter followed the expected genotype distribution according to Mendelian genetics. Schematics were designed with biorender.com

5.1.5 Validation of *Tet3* knockout *in vivo* using genotyping PCR

Following the successful generation of *Tet3$^{fl/fl}$; Cdh5^{Cre+}* mice, we utilized primer pairs P7-P8 to detect the knockout band from DNA isolated from the heart tissue of the mice. As the heart tissue is comprised of several cells other than endothelial cells, we observed two bands on the agarose gel corresponding to the floxed alleles (1228 bp) and the knockout band (310 bp), as described previously (Figure 11-B). The PCR product from *Tet3$^{fl/fl}$; Cdh5^{Cre-}* heart tissue revealed a single band pattern corresponding to floxed alleles (1228 bp) (Figure 13-A).

Additionally, we utilized primers to detect the presence of Cre recombinase, which was provided by Jackson Laboratories, to ensure proper Cre expression in heart tissue. The PCR product from *Tet3*$^{fl/fl}$*; Cdh5*$^{Cre+}$ revealed a band at 500 bp corresponding to the Cre transgene and a band at 324 bp as an internal positive control, whereas *Tet3*$^{fl/fl}$*; Cdh5*$^{Cre-}$ PCR amplification did not produce a band at 500 bp corresponding to the Cre transgene (Figure 13-B).

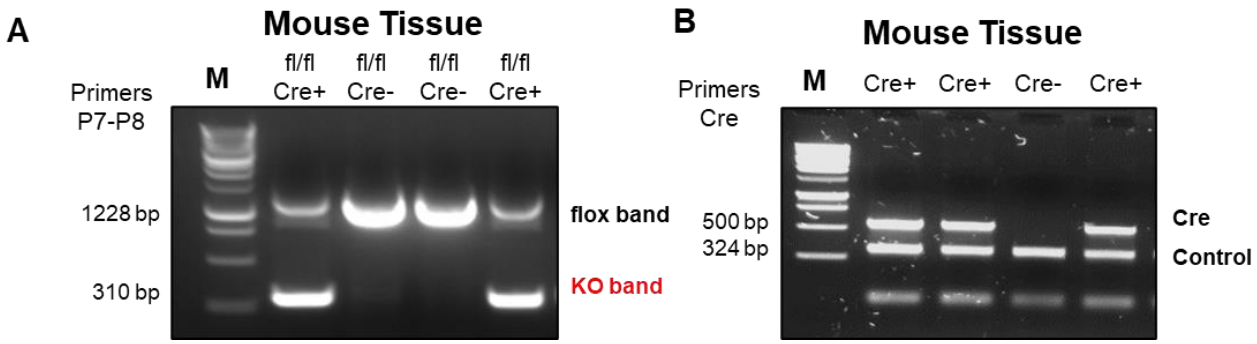

Figure 13: *In vivo* validation of *Tet3* knockout. (A) Representative 1 % agarose gel of the PCR product from DNA isolated from mouse heart tissue using primer pairs P7-P8. Lanes 1 and 4 show a two-band pattern at 1228 bp (floxed allele) and 310 bp (knockout band), respectively, corresponding to the homozygous knockout mouse *Tet3*$^{fl/fl}$*; Cdh5*$^{Cre+}$. Lanes 2-4 correspond to the homozygous floxed mouse without Cre recombination, *Tet3*$^{fl/fl}$*; Cdh5*$^{Cre-}$. **(B)** Representative 2% agarose gel electrophoresis of the PCR product from DNA isolated from mouse heart tissue to detect the presence or absence of Cre. The presence of Cre is indicated by an upper band (500 bp). The lower band (324 bp) was used as an internal positive control band to ensure the quality of the PCR amplification reaction. M, DNA molecular size marker

5.1.6 Validation of endothelial-specific *Tet3* knockout *in vivo*

TET3 protein and mRNA levels were evaluated to ensure proper deletion and loss of TET3 expression in endothelial cells of transgenic knockout mice. Immunohistochemistry and immunofluorescence staining revealed a typical nuclear localization of TET3 in the heart section of *Tet3*$^{fl/fl}$*; Cdh5*$^{Cre-}$, mice with a higher expression in non-cardiomyocytes (endothelial cells and fibroblasts) (Figure 14-A). Endothelial *Tet3* knockout mice showed a loss of TET3 protein expression in the endothelial cell population, as observed with the reduced intensity of staining visualized around vessels and capillaries in the heart tissue section, but not in other cell populations (Figure 14-A). We also monitored Cre expression and found significantly

high levels of Cre in *Tet3*$^{fl/fl}$*; Cdh5*$^{Cre+}$ mice compared to that in *Tet3*$^{fl/fl}$*; Cdh5*$^{Cre-}$ mice (Figure 14-B). Moreover, RNA isolated from the left ventricle revealed a significant reduction in global *Tet3* mRNA expression upon *Tet3* knockout, using primers targeting exons upstream and downstream of exon 4 (Figure 14-C). To further validate the specific knockout of *Tet3* in the endothelial cell population, cells isolated from the heart tissue of *Tet3*$^{fl/fl}$*; Cdh5*$^{Cre-}$ and *Tet3*$^{fl/fl}$*; Cdh5*$^{Cre+}$ mice were sorted by flow cytometry. Endothelial cells were sorted using a fluorescence-conjugated antibody against VE-cadherin (Alexa Fluor 647 Anti-Cdh5, BD Biosciences), and the collected cells were divided into two populations, Cdh5(-) or Cdh5(+) (Figure 14-D). RNA isolated from Cdh5(+) cells showed a significant reduction in *Tet3* mRNA (85% reduction) expression in *Tet3*$^{fl/fl}$*; Cdh5*$^{Cre+}$ mice compared to control mice (Figure 14-E-F). Moreover, the Cdh5(-) population of cells was also evaluated to check for Cre-recombination in non-endothelial cells. The results showed no difference in *Tet3* mRNA expression between the knockout and control transgenic mouse lines in the non-endothelial population (Cdh5-) (Figure 14-G-H). Altogether, these results prove that we successfully generated a model that could efficiently and specifically knockout *Tet3* in endothelial cells *in vivo*.

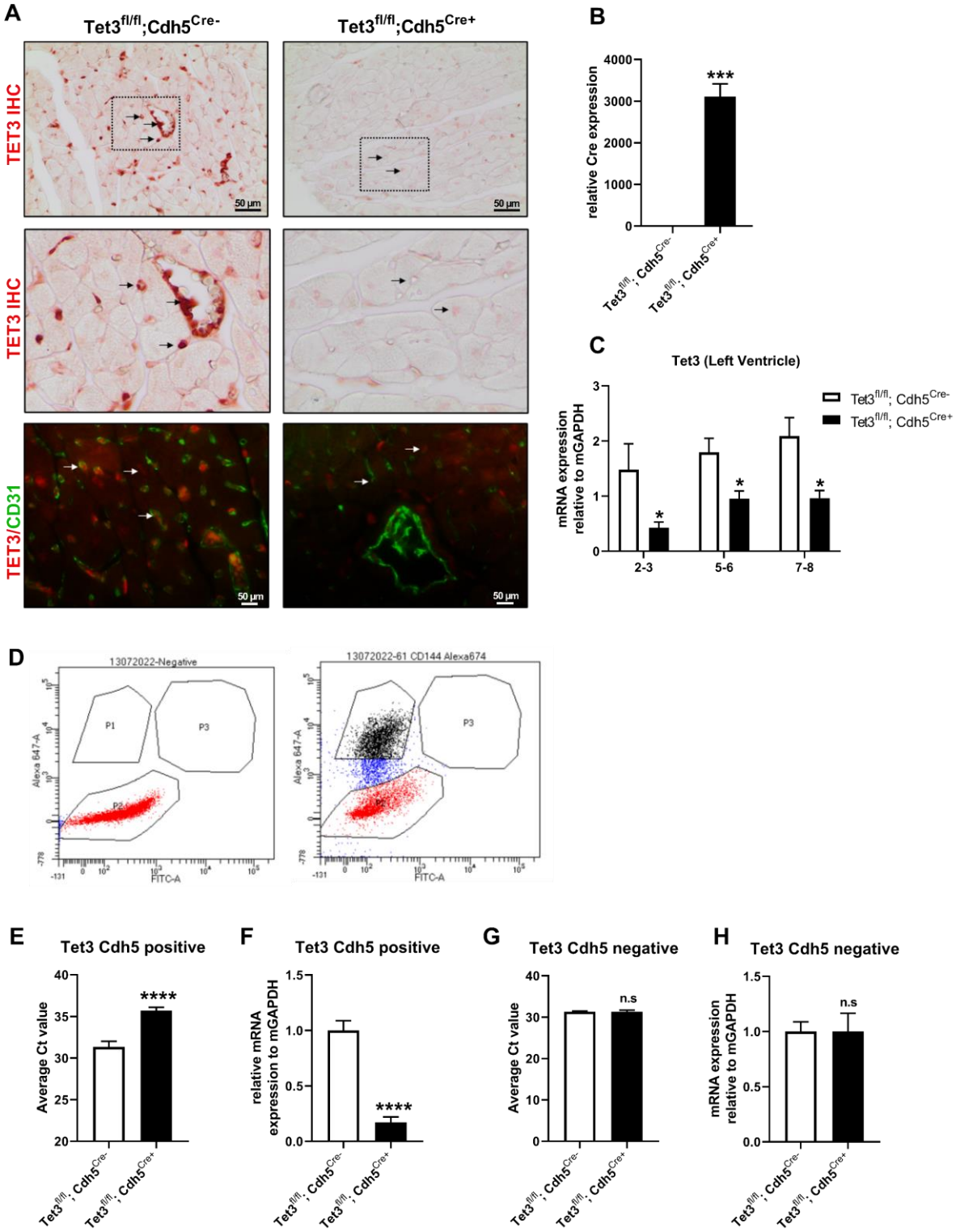

Figure 14: *In vivo* mouse validation of *Tet3* knockout (A) Representative immunohistochemistry and immunofluorescence images of TET3 protein expression in *Tet3$^{fl/fl}$; Cdh5^{Cre-}* and *Tet3$^{fl/fl}$; Cdh5^{Cre+}* mice. Heart sections stained with TET3 antibody revealed lower TET3 protein expression in the endothelial cells of the knockout mice. **(B)** qRT-PCR analysis of the relative mRNA expression of Cre

recombinase showed significantly higher Cre expression in *Tet3* knockout mice than in control mice. **(C)** qRT-PCR analysis of the relative mRNA expression of *Tet3* in the left ventricle heart tissue between $Tet3^{fl/fl}; Cdh5^{Cre-}$ and $Tet3^{fl/fl}; Cdh5^{Cre+}$ mice showed significant reduction in *Tet3* expression in endothelial *Tet3* knockout mice. Primers were designed to amplify regions upstream and downstream of exon 4. (2-3), (5-6), and (7-8) denote the primer exon location. **(D)** Representative flow cytometry histograms of the sorted cells from the isolated heart tissues of either $Tet3^{fl/fl}; Cdh5^{Cre-}$ or $Tet3^{fl/fl}; Cdh5^{Cre+}$ mice. Cells were sequentially gated based on cell size and heterogeneity (forward scatter [FSC] versus side scatter [SSC]). The left plot represents a negative control sample of unlabeled cells. The right plot represents cells labeled with Alexa Fluour-647 conjugated VE-cadherin (Cdh5) antibody and shows an enriched population of Cdh5(+) cells. **(E-H)** qRT-PCR analysis of the relative mRNA expression of *Tet3* in Cdh5 (+) or (-) sorted cell populations. **(E, G)** Graphs representing the raw average Ct value of *Tet3* mRNA expression. Summarized quantitative findings are shown as the mean ±SEM. Statistical significance was calculated using an unpaired two-tailed Student's t-test, and p-values correspond to *$p \leq 0.05$, ***$p \leq 0.001$, ****$p \leq 0.0001$, n.s not significant. Scale bars represent 50 μm (n= 4 per group).

5.2 Evaluation of the phenotype

14 weeks old male and female knockout mice ($Tet3^{fl/fl}; Cdh5^{Cre+}$, **knockout**) were compared to control mice ($Tet3^{fl/fl}; Cdh5^{Cre-}$, **control**) in order to assess phenotypic changes in cardiac function upon endothelial-specific deletion of TET3.

5.2.1 Endothelial *Tet3* knockout mice have an enlarged left ventricle

The generated transgenic mice appeared healthy, with no signs of growth retardation prior to sacrifice. No histological abnormalities were detected in the tissues of the organs collected from knockout or control transgenic mice stained with hematoxylin and eosin (data not shown).

Echo analysis was performed to evaluate changes in cardiac function upon endothelial-specific deletion of *Tet3*. The knockout mice showed a significantly larger left ventricular mass compared to that of the control mice (Figure 15-A). On average, there was no difference in mouse body weight between the two groups (Figure 15-B). In addition, *in vivo* echocardiographic imaging showed no difference in the measured heart rate between the two mice groups (Figure 15-C). Macroscopically, endothelial *Tet3* knockout mouse hearts were larger in size, which was also evident by a larger cross-sectional area from the hematoxylin and eosin staining of the heart (Figure 15-D). Both male and female knockout mice had a significantly higher heart weight to body weight ratio in comparison with that of the control

mice (Figure 15-E-F). Taken together, these results show that endothelial-specific *Tet3* knockout mice have an enlarged heart, as indicated by an increased left ventricular size under baseline conditions.

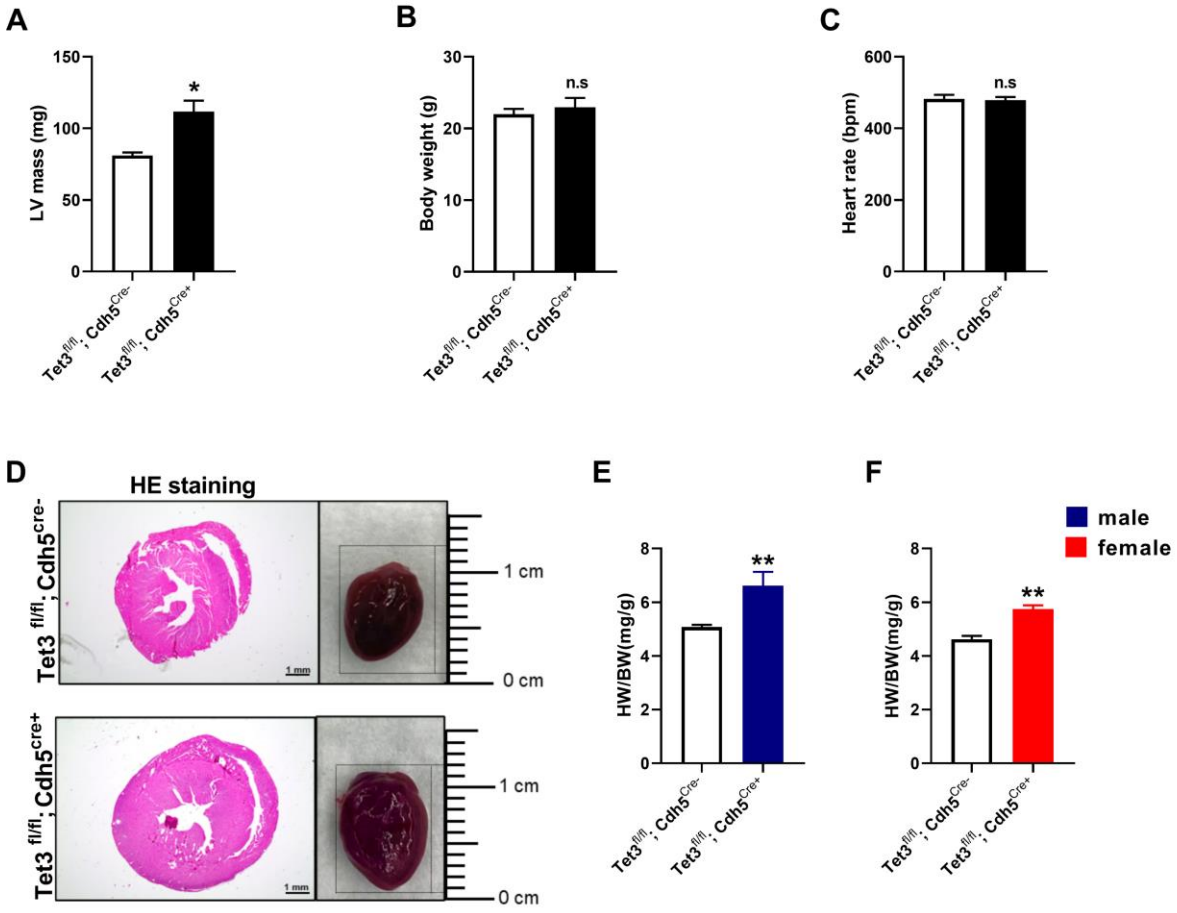

Figure 15: Endothelial-specific deletion of *Tet3* is associated with an enlarged left ventricle. *In vivo* echocardiographic analysis was performed to analyze cardiac function in the mice. **(A)** Knockout mice revealed a larger left ventricular mass compared to control mice. **(B)** Body weights of mice were recorded prior to sacrifice. **(C)** Heart rate measurements showed no significant differences between the groups. **(D)** Upon sacrifice of the mice, images of the hearts were acquired to compare the macroscopic size differences. Representative HE images of $Tet3^{fl/fl}$; $Cdh5^{Cre+}$, KO and $Tet3^{fl/fl}$; $Cdh5^{Cre-}$, WT mice showed that the KO mice have a larger cross-sectional area than control mice. **(E-F)** Heart weight/ body weight ratio was calculated and showed a significantly higher ratio in both male and female knockout mice in comparison with control mice. Summarized quantitative findings are shown as the mean ±SEM. Statistical significance was calculated using an unpaired two-tailed Student's t-test, and p-values correspond to *$p \leq 0.05$, **$p \leq 0.01$, n. s. not significant, n= 6 per group. Scalebars represent 1 mm.

5.2.2 Endothelial *Tet3* knockout is associated with reduced systolic function

Systolic function in mice was assessed using echocardiographic imaging analysis in M-mode. The results showed a significant decrease in both ejection fraction (EF%) and fractional shortening (FS%) in male *Tet3* knockout mice in comparison to control mice (Figure 16-A-B). However, no significant difference in both EF% or FS% was observed in female *Tet3* knockout mice (Figure 16-E-F). In line with the worsened ejection fraction and fractional shortening, we also observed an increase in both left ventricle inner diameter during systole and diastole in male *Tet3* knockout mice compared to control mice (Figure 16-C-D). The female knockout mice also followed the same trend with increased left ventricle inner diameter during systole and diastole but with no significant difference in comparison to control mice (Figure 16-G-H). Taken together, these results suggest possible systolic dysfunction in male mice upon TET3 deletion in endothelial cells under baseline conditions.

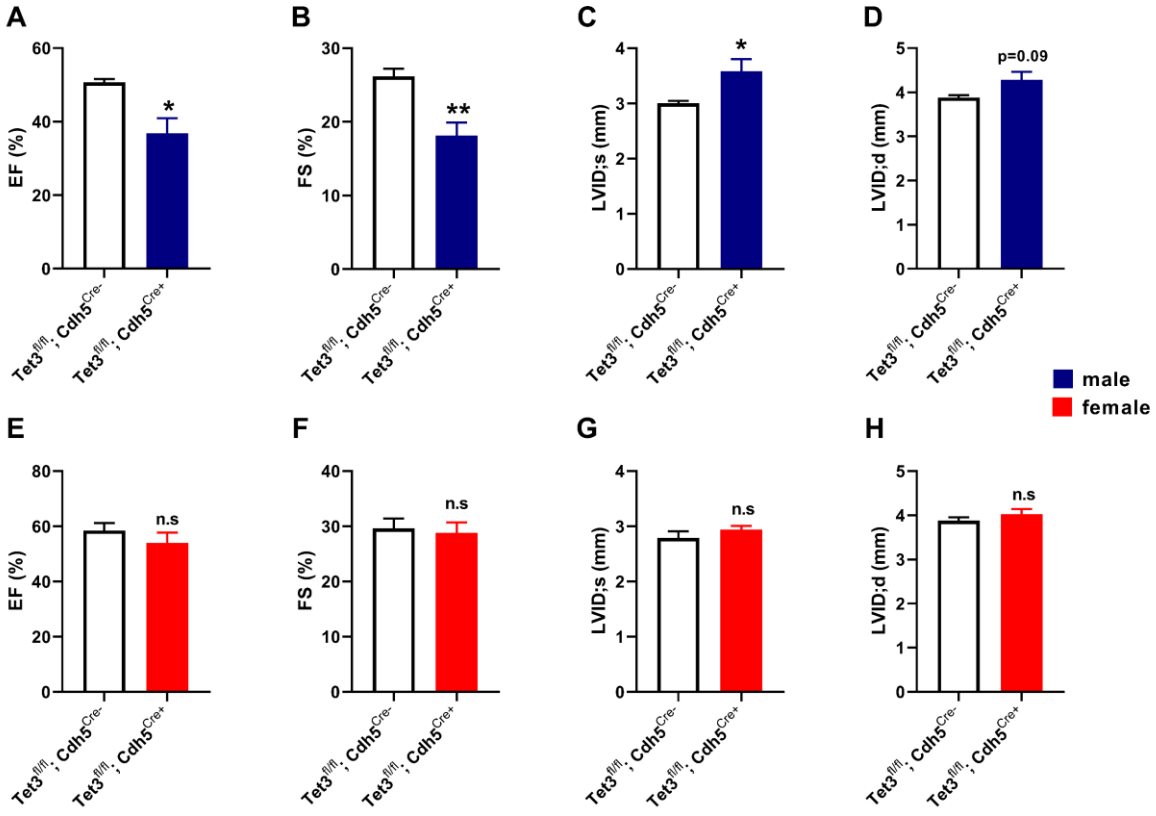

Figure 16: Male endothelial *Tet3* knockout mice have a worsened systolic function. *In vivo* echocardiographic analysis was performed to analyze cardiac function in the mice. **(A, E– B-F)** Ejection fraction (%) and Fractional shortening (%) were measured prior to sacrifice of mice. (C, G – D, H) Left ventricular inner diameter during systole (LVID; s) or diastole (LVID; d) (mm). Blue and red colors represent male and female mice, respectively. Summarized quantitative findings are shown

as the mean ±SEM. Statistical significance was calculated using an unpaired two-tailed Student's t-test, and p-values correspond to *p ≤ 0.05, **p ≤ 0.01, n. s. not significant, n= 6 per group.

5.2.3 Endothelial *Tet3* knockout mice undergo concentric remodeling

We next evaluated parameters related to differentiating possible remodeling processes, as the heart size, left ventricular mass (Figure 15- A, D, E), and end diastolic diameter (Figure 16- D, H) were elevated in knockout mice compared than in control mice. Echocardiographic analysis revealed differences in cardiac remodeling upon *Tet3* knockout in endothelial cells compared than in control mice. Both male and female knockout mice had increased posterior wall thickness compared to control mice (Figure 17- A, B). The average septum wall thickness was also significantly elevated in the knockout mice in comparison to the control mice (Figure 17- C). The relative wall thickness (RWT), which is a marker used to differentiate between concentric and eccentric remodeling, was calculated as follows: (septum thickness + posterior wall thickness) / left ventricular end-diastolic diameter. *Tet3* knockout mice showed a significantly higher RWT as compared to control mice (Figure 17- D). This increase in relative wall thickness in endothelial *Tet3* knockout mice indicated concentric remodeling of the heart compared to that observed in the respective controls.

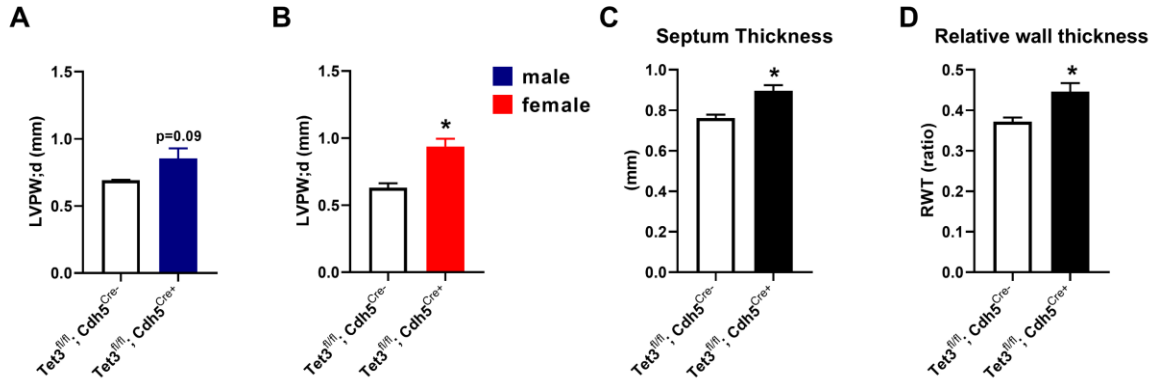

Figure 17: Echocardiographic assessment of cardiac remodeling in mice following *Tet3* knockout in endothelial cells. (A, B) Left ventricular posterior wall thickness at diastole (LVPW;d mm) and **(C)** septum wall thickness (mm) were recorded with echocardiographic analysis. **(D)** Relative wall thickness (RWT) ratio was calculated as previously described. Blue and red colors represent male and female mice, respectively. Summarized quantitative findings are shown as the mean ±SEM. Statistical significance was calculated using an unpaired two-tailed Student's t-test, and p-values correspond to *p ≤ 0.05, n= 6/12 per group.

5.2.4 Endothelial *Tet3* knockout mice display increased fibrosis

We next sought to evaluate the levels of cardiac fibrosis between the two mice groups. Thus, we performed picrosirius red staining as explained in section 4.17.3. Upon image acquisition of the stained tissue sections, we detected an increase in collagen deposition (red) in *Tet3* knockout mice compared to control mice (Figure 18-A), which was further confirmed by quantifying both interstitial and perivascular fibrosis levels. *Tet3* knockout mice showed significantly elevated interstitial fibrosis along with even a more significant increase of perivascular fibrosis in comparison to control mice (Figure 18-B, C). Further evaluation of the tissue sections using immunofluorescence staining for COL1A1 revealed prominent collagen deposition around the vessels and capillaries of *Tet3* endothelial knockout mice compared to control mice (Figure 18-D). In line with this evaluation, collagen deposition intensity was quantified using FIJI imaging software and revealed denser collagen staining around the vessels of *Tet3* knockout mice in comparison to the control mice (Figure 18-D). Co-immunofluorescence staining of α-SMA and COL1A1 confirmed our previous findings and highlighted the distinct increase in collagen I and α-SMA around capillaries and vessel linings in heart tissue sections of *Tet3* knockout mice (Figure 18-E).

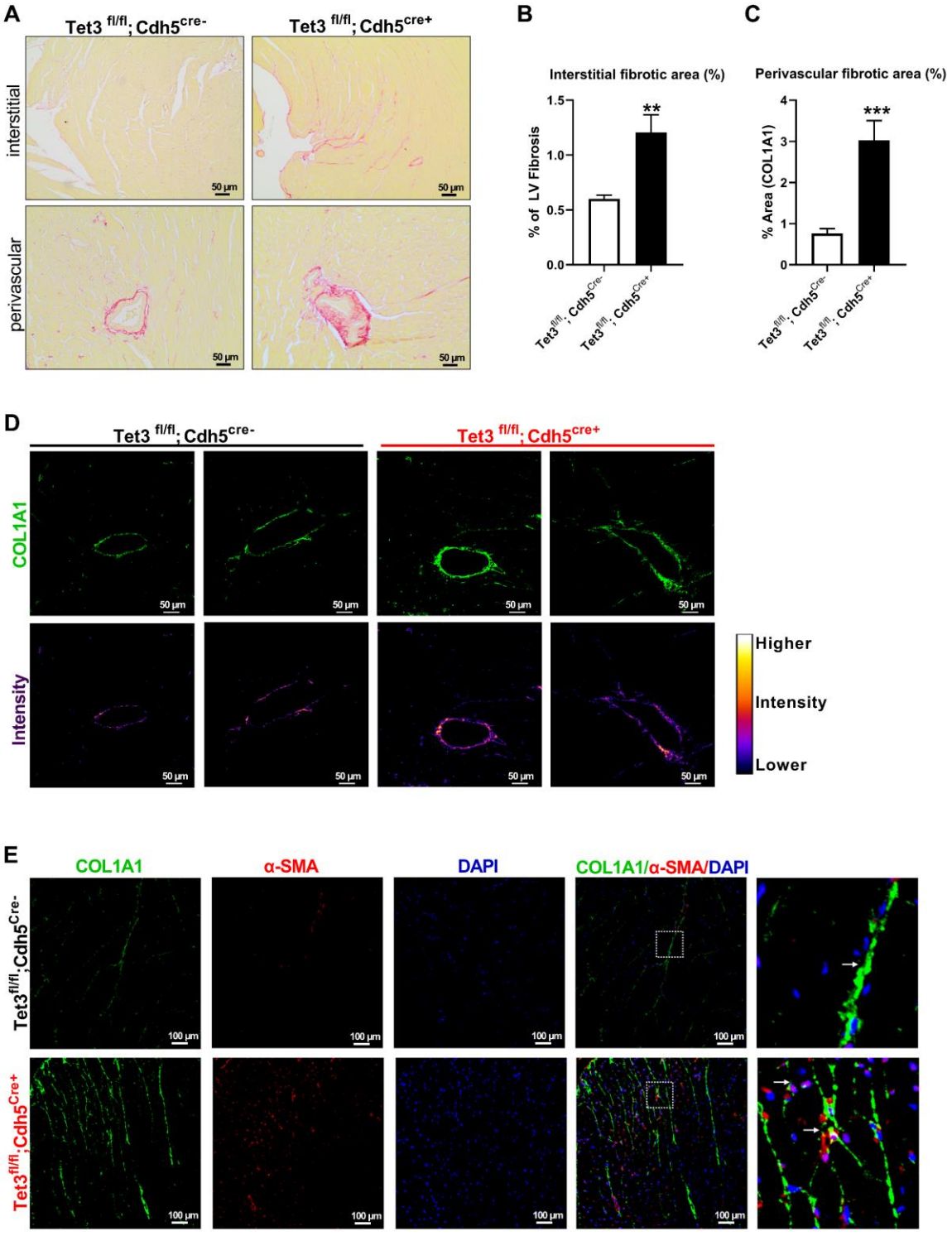

Figure 18: *Tet3* knockout mice show increased fibrosis. (A) Representative images of heart sections stained with picrosirius red, which stains collagen fibers red. **(B, C)** Graphs showing the quantification analysis of both interstitial and perivascular fibrotic areas. **(D)** Collagen immunofluorescence staining of heart vessels (top lane) along with representative relative intensity images of collagen I deposition using the Local thickness plugin from Fiji imaging software. The calibration bar on the right side shows

the relative intensity of collagen deposition. **(E)** Representative confocal images of immunofluorescence staining of heart tissue sections with collagen I and α-SMA, and nuclear staining with DAPI. *Tet3* knockout mice showed increased collagen I and α-SMA levels compared to control mice. Summarized quantitative findings are shown as the mean ±SEM. Statistical significance was calculated using an unpaired two-tailed Student's t-test, and P-values correspond to **p ≤ 0.01, ***p ≤ 0.001. Scale bars represent 50 μm (A, D) and 100 μm.(E) n= 6 per group.

5.3 Endothelial *Tet3* knockout mice show elevated EndMT markers and reduced miR-30d-5p expression

5.3.1 EndMT markers are elevated in endothelial *Tet3* knockout mice

Previous reports revealed that endothelial cells can contribute to the myofibroblast population and fibrosis via EndMT process (Xu et al., 2016; Zeisberg, Tarnavski, et al., 2007; Zhang et al., 2018). Since histological analysis showed an effect of *Tet3* knockout in endothelial cells on overall fibrosis, and specifically on perivascular fibrosis, we sought to further understand the molecular mechanisms underlying the fibrotic phenotype. As such, we performed qRT-PCR analysis of left ventricular heart tissue to analyze the expression of EndMT markers. Our results showed a significant upregulation of *Snail* and *Twist* in endothelial *Tet3* knockout mice compared to control mice (Figure 19-A, C). *Slug* mRNA expression was also slightly elevated (p=0.09) in *Tet3* knockout mice compared to that in control mice (Figure 19-B). Interestingly, among the three EndMT markers, *Snail* upregulation was the most drastic with approximately 3.5-fold higher expression in *Tet3* knockout mice than in control mice (Figure 19-A). We also showed significant upregulation of *Acta2* (α-SMA) mRNA expression in *Tet3* knockout mice (Figure 19-D), which was in line with the previous confocal image analysis showing an abundance of α-SMA protein expression in the knockout mice as compared to the control mice (Figure 19-D).

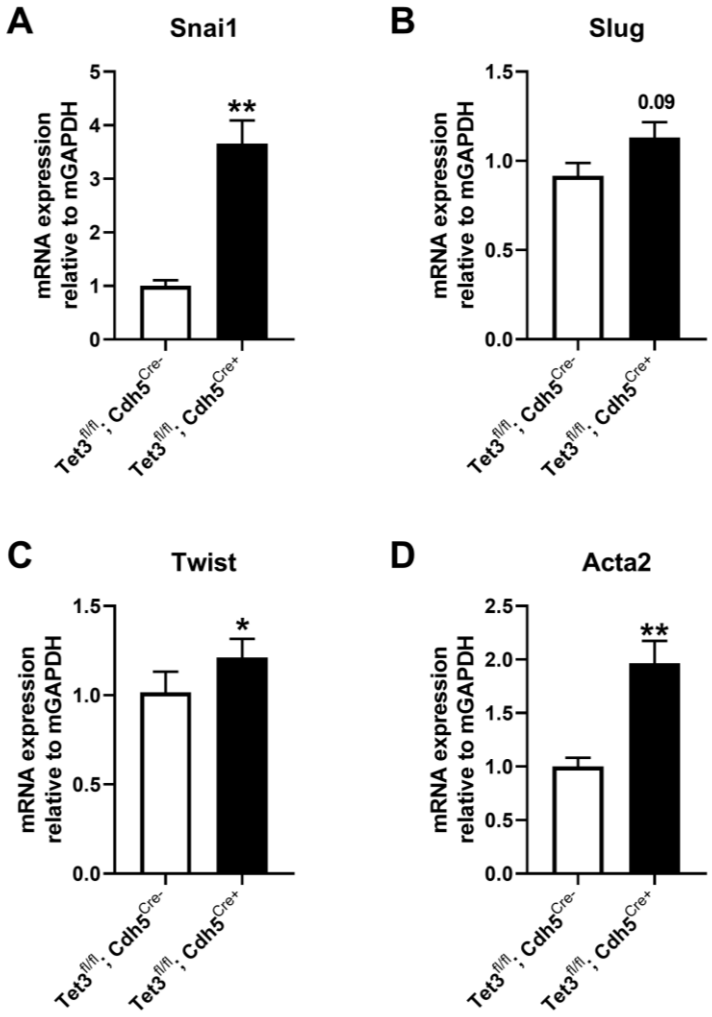

Figure 19: Increased EndMT marker expression in endothelial specific *Tet3* knockout mice. (A-D) qRT-PCR analysis of the mRNA expression of *Snail, Slug, Twist,* and *Acta2* from the left ventricular heart tissue. The results showed significant upregulation of the EndMT markers *Snail* and *Twist* as well as *Acta2* in $Tet3^{fl/fl}$; $Cdh5^{Cre+}$ mice compared to $Tet3^{fl/fl}$; $Cdh5^{Cre-}$ mice. Summarized quantitative findings are shown as the mean ±SEM. Statistical significance was calculated using an unpaired two-tailed Student's t-test, and p-values corresponding to *$p \leq 0.05$, ***$p \leq 0.001$ (n= 6 per group).

5.3.2 miR-30d-5p is reduced upon *Tet3* knockout in endothelial cells

Recently, numerous studies have highlighted the protective role of the miR-30d as a biomarker and therapeutic target in the cardiovascular and cancer fields (Holley et al., 2021; J. Li et al., 2022; Melman et al., 2015; Xu et al., 2021; Zhu et al., 2018). The protective role of miR-30d role has been described to be mediated by several mechanisms including, inhibition of proliferation, invasiveness, and tumor suppression by targeting EMT (Yang et al., 2017). More importantly, researchers have shown that TET3 can activate miR-30d, which acts as an

inhibitor of epithelial-to-mesenchymal transition (EMT) in ovarian cancer by targeting *Snail* (Ye et al., 2015, 2016). Exactly how TET3 exerts a positive regulatory effect on miR-30d expression is not understood. To gain further mechanistic insights and corroborate the induction of *Snail* expression in $Tet3^{fl/fl}$; $Cdh5^{Cre+}$ mice, we analyzed the expression levels of miR-30d-5p in the heart tissue of the mice. qRT-PCR analysis showed a significant downregulation of miR-30d-5p expression in endothelial *Tet3* knockout mice compared to control mice (Figure 20-A-B). These data suggest that *Tet3* may be an upstream regulator of the cardioprotective miR-30d.

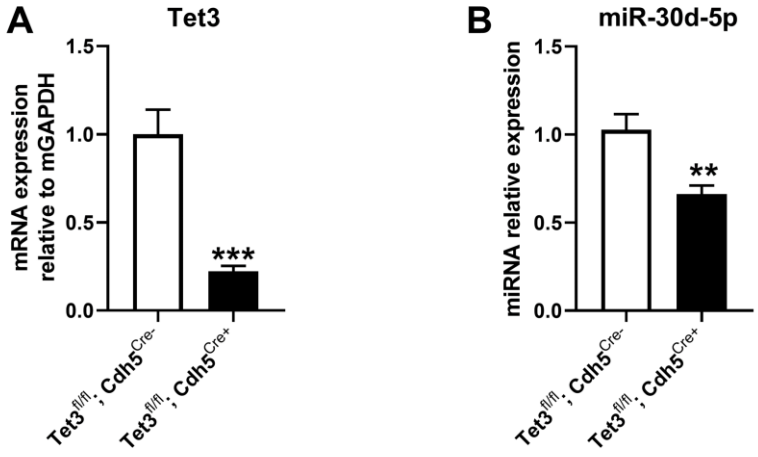

Figure 20: miR-30d expression is reduced in endothelial specific *Tet3* knockout mice. (A, B) qRT-PCR analysis of the mRNA expression of *Tet3* and miRNA expression of miR30d-5p in $Tet3^{fl/fl}$; $Cdh5^{Cre-}$ mice compared to $Tet3^{fl/fl}$; $Cdh5^{Cre+}$ mice. The expression level of miR-30d was normalized to its internal control U6. Summarized quantitative findings are shown as the mean ±SEM. Statistical significance was calculated using an unpaired two-tailed Student's t-test, and p-values corresponding to $^{**}p \leq 0.01$, $^{***}p \leq 0.001$ (n= 6 per group).

5.4 miR-30d-5p is downregulated in fibrotic conditions *in vivo*

To investigate the role of miR-30d in a pathological hypertrophy model *in vivo*, we implanted mice with osmotic minipumps containing angiotensin II at a dose of 1.5mg/kg/day for 4 weeks, as explained in section 4.11.5. Mice treated with angiotensin II showed clear development of fibrosis, as seen by picrosirius red staining, which showed increased collagen deposition (Figure 21-A). The overall left ventricular fibrotic area was significantly higher in mice treated with angiotensin II compared to PBS-treated mice (Figure 21-B). mRNA analysis of hypertrophic markers showed significant upregulation of *Anp*, *Bnp*, and *Myh7* expression in

angiotensin treated mice (Figure 21-C). Moreover, in line with our previous data (Kumar Rath, 2020), TET3 protein and mRNA expression were significantly reduced in angiotensin-treated mice compared with vehicle control mice (Figure 21-D). Finally, angiotensin-treated mice had significantly lower miR-30d-5p expression in comparison with vehicle mice. (Figure 21-E). Collectively, these data suggest that miR-30d loss might be a major mediator of pathological cardiac hypertrophy.

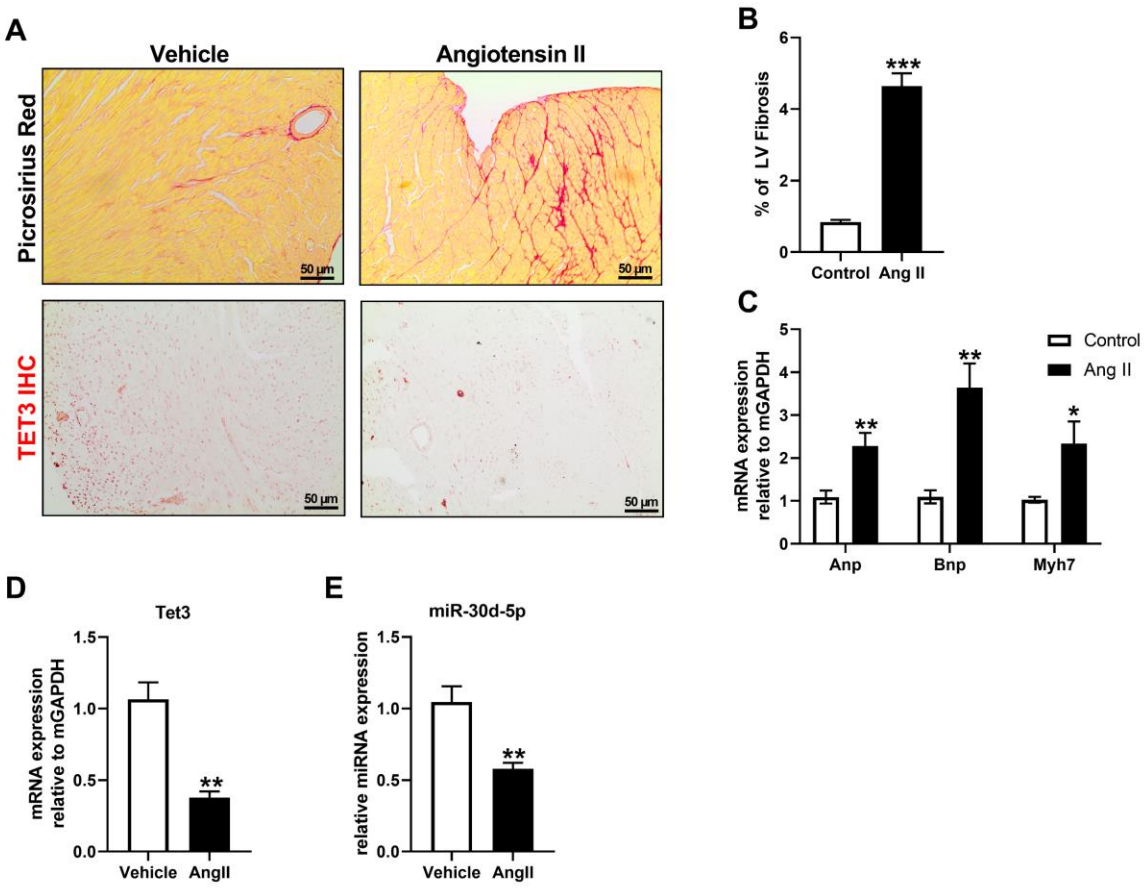

Figure 21: miR-30d is downregulated in a cardiac hypertrophy mouse model. (A) Picrosirius red (PS) staining and TET3 immunohistochemistry (IHC) staining of heart sections from mice treated with Ang II or PBS for 4 weeks**.** PS staining showed increased collagen I deposition in angiotensin II-treated mice, and TET3 IHC showed a significant loss of TET3 protein expression upon angiotensin II treatment. **(B)** Graph of quantification of the overall fibrotic area shows significantly increased fibrosis in angiotensin II treated mice in comparison to PBS treated mice. **(C-D)** qRT-PCR analysis of the mRNA expression of *Anp*, *Bnp*, *Myh7*, and *Tet3* from the left ventricular heart tissue treated with vehicle or angiotensin II. Angiotensin II-treated mice showed significant upregulation of *Anp* and *Bnp*, and *Myh7* expression. *Tet3* mRNA levels were significantly reduced upon angiotensin II treatment. **(E**)

qRT-PCR analysis of the relative miRNA expression of miR-30d-5p showed a significant reduction in miRNA levels upon angiotensin II treatment compared with vehicle-treated mice. The expression level of miR-30d was normalized to its internal control U6. Summarized quantitative findings are shown as the mean ±SEM. Statistical significance was calculated using an unpaired two-tailed Student's t-test, and p-values correspond to **p ≤ 0. 01, ***p ≤ 0. 001, n.s not significant. (n= 6 per group). Scalebars represent 50 μm

5.5 miR-30d-5p is downregulated in TGF-β1 treated cardiac endothelial cells

To mimic EndMT *in vitro*, we treated mouse cardiac endothelial cells (MCEC) with TGF-β1 for 6 days as explained in section 4.2. We monitored the cells for morphological changes upon TGF-β1 treatment and performed phalloidin staining to reveal the transition from a typical cobblestone shape in control cells to a fibroblast like morphology in treated cells with increased F-actin filament intensity (Figure 22-A). In parallel, we analyzed the mRNA expression of fibrotic and EndMT markers. qRT-PCR analysis indicated a marked upregulation in collagen I and *Acta2*, as well as *Snail* and *Slug*, upon exposure to TGF-β1 in comparison with untreated cells (Figure 22-B). These results validate the successful transition of the endothelial cells via EndMT to a fibroblast-like cell after treatment with TGF-β1. In line with our previous research which showed decreased *Tet3* expression in TGF-β1 treated human coronary artery endothelial cells (Xu et al., 2015), our data could also show the significant downregulation of *Tet3* mRNA expression in MCECs 6 days after TGF-β1 treatment *in vitro* (Figure 22-C). Moreover, we investigated the involvement of miR-30d during End-MT by analyzing changes in its expression in MCEC exposed to TGF-β1 for 6 days. qRT-PCR analysis showed a significantly lower miR-30d expression upon TGF-β1 treatment (Figure 22-D). These findings indicate a possible involvement of *miR-30d* in the EndMT process.

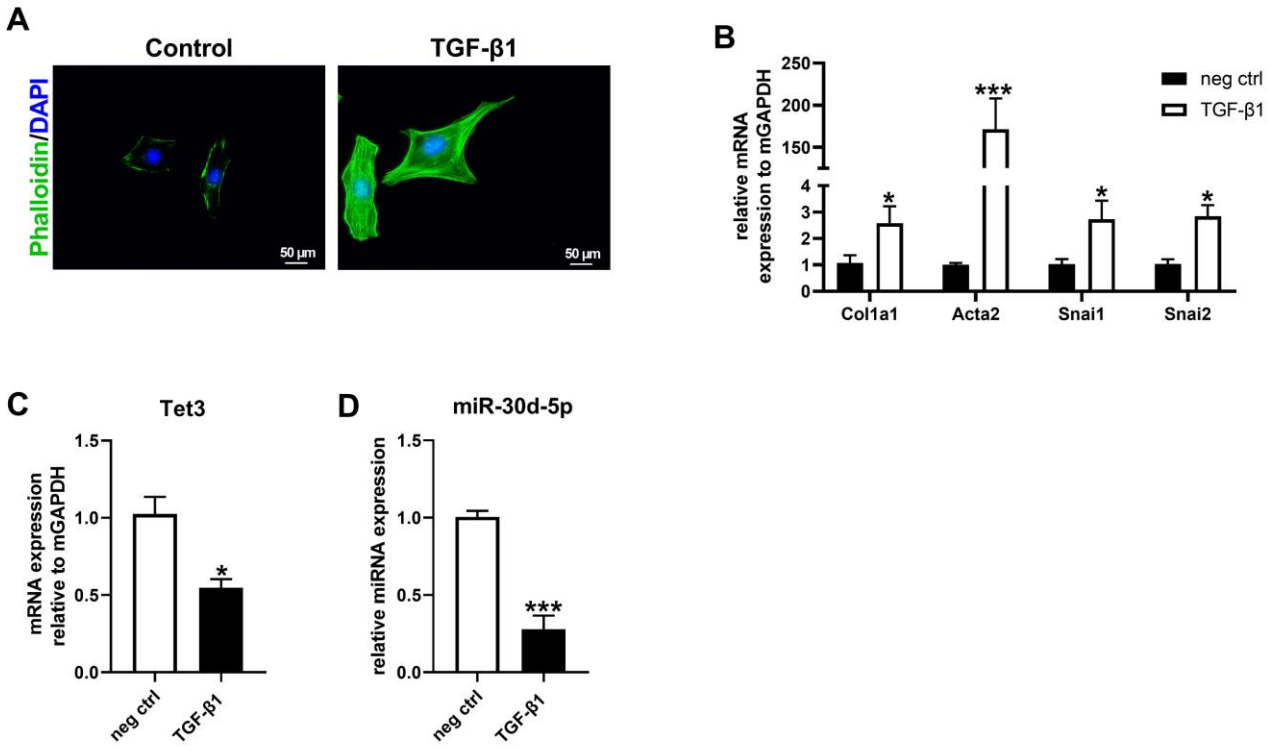

Figure 22: miR-30d is downregulated in fibrotic conditions *in vitro*. (A) Representative images of phalloidin staining of mouse cardiac endothelial cells treated with TGF-β1 for 6 days. TGF-β1 treated cells showed more dense actin filaments in comparison with untreated cells. **(B)** qRT-PCR analysis showed a significant increase in the mRNA levels of the fibrotic markers collagen I and *Acta2*, and EndMT markers *Snail* (Snai1*)* and *Slu*g (Snai2) upon TGF-β1 treatment. **(C-D)** qRT-PCR analysis showing significant reduction of *Tet3* and miR30d-5p in cells exposed to TGF-β1. Scale bars represent 50 µm. Summarized quantitative findings are shown as the mean ±SEM. Statistical significance was calculated using an unpaired two-tailed Student's t-test, and p-values correspond to *p ≤ 0. 05, ***p ≤ 0. 001, ****p ≤ 0. 0001. n= 3 biological replicates.

5.6 Tet3 regulates miR-30d-5p expression by promoter demethylation

5.6.1 miR-30d-5p inhibits TGF-β1 induced Snail expression

To investigate whether miR-30d regulates EndMT, we used bioinformatic analysis to identify potential target genes (TargetScan). The prediction analysis showed that the binding sequence of both human and mouse miR-30d-5p was found in the Snail 3'UTR. This finding is in line with previous evidence, which showed miR-30d targeting of *Snail* is protective against vascular calcification and EMT in ovarian cancer respectively (Ciavarella et al., 2021; Ye et al., 2015).To provide evidence that miR-30d can directly bind to *Snail* 3'UTR and regulate the EndMT process, we transfected MCECs with miR-30d-5p mimic (LNA technology,

Qiagen), which contains the sequence of the respective mature miRNA and evaluated the transfection efficiency in comparison to a negative control template. We preliminary verified the efficient overexpression of miR-30d-5p 48 hours after transfection compared to the negative control (Figure 23-A). Then we performed a luciferase reporter assay whereby we utilized a plasmid which contains the 3'UTR sequence of Snail (downstream of a firefly luciferase reporter gene of (pEZX-MT06 Snai1 3'UTR) (Figure 23-B). We co-transfected MCECs with the reporter plasmid and either miRNA mimic or negative control to assess whether miR-30d-5p binds to the 3'UTR of Snail. 48 hours post transfection, we found that co-transfection of pEZX-MT06 Snai1 3'UTR with miR-30d-5p mimic significantly reduced the luciferase activity by 45% in comparison with the negative control miRNA (Figure 23-C). Furthermore, we assessed if *miR-30d* overexpression can inhibit SNAIL protein expression *in vitro* following TGF-β1 treatment. As such, we treated MCECs with TGF-β1 for 6 days in total and transfected either miR-30d-5p mimic or negative control at day 2 of the treatment. The cells were collected 6 days after TGF-β1 treatment, and we evaluated SNAIL protein expression by western blot. Western blot analysis revealed significant increase in SNAIL following TGF-β1 treatment in the presence of miRNA negative control, which was reduced upon transfection with the miRNA mimic (Figure 23-D, E). These results showed that miR-30d is a negative regulator of EndMT, which acts by inhibiting SNAIL expression via directly binding to its 3'UTR.

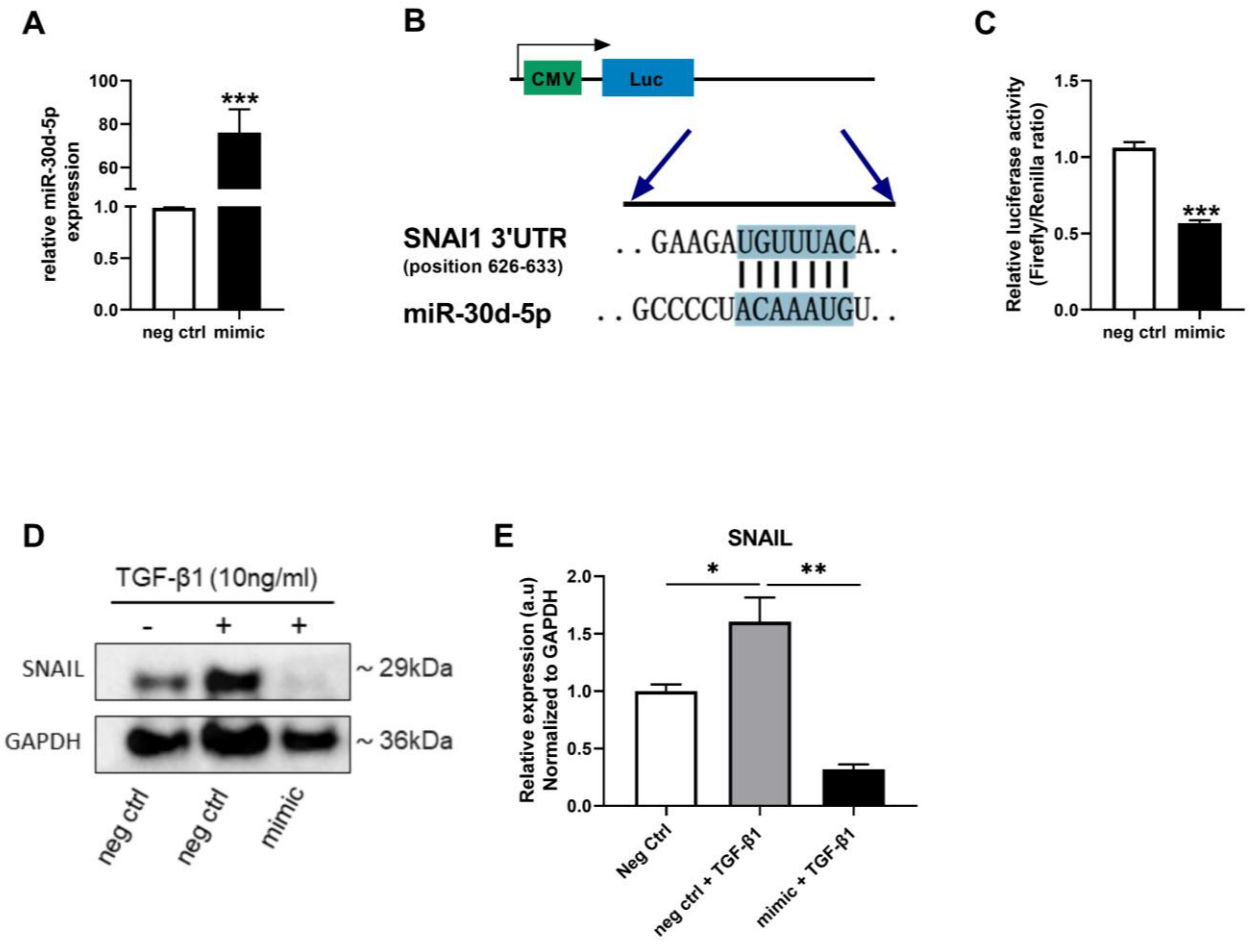

Figure 23: miR-30d targets *Snail* by interacting with its 3'UTR. (A) qRT-PCR analysis showing significant increase in miR-30d-5p expression following two days of transfection of cells with miRNA mimic compared to the negative control. **(B)** Representative schematic of the luciferase reporter plasmid which contains the *Snail* 3'UTR sequence downstream of the firefly luciferase gene. The predicted binding site of miR-30d on Snail 3'UTR depicted in the schematic from Target Scan prediction website. **(C)** Luciferase reporter assay showing the relative luciferase activity (calculated as firefly/renilla ratio) following transfection of the cells with pEZX-MT06 Snai1 3'UTR reporter vector with miRNA mimic or negative control. **(D)** Representative immunoblotting of SNAIL protein levels in TGF-β1 treated MCEC shows significant reduction in Snail expression following overexpression with miR-30d mimic in comparison with negative control **(E)** Graph showing the quantification of the relative SNAIL intensity after normalization with GAPDH. Summarized quantitative findings are shown as the mean ±SEM. Statistical significance was calculated using an unpaired two tailed Student's t-test (A, C) and (E) one-way ANOVA followed by Tukey multiple comparison test. P-values correspond to *p ≤ 0. 05, **p ≤ 0. 01, ***p ≤ 0. 001. n= 3 biological replicates.

5.6.2 miR-30d expression is regulated by promoter methylation

We have previously shown that TET3 overexpression can reverse TGF-β1 induced EndMT *in vitro* (Xu et al., 2015) . Since *Tet3* knockout mice showed significantly reduced levels of miR-30d, we have speculated that Tet3's protective role in controlling EndMT can be mediated by miR-30d and that Tet3 is an upstream regulator of miR-30d expression. Therefore, we hypothesized that the downregulation of miR-30d in fibrotic conditions and upon loss of *Tet3* in endothelial cells could be via the methylation of the promoter of the pre-miR-30d transcript. To explore the possibility of whether the promoter of miR-30d can be methylated, we designed 8 different pairs of methylation-specific primers flanking the region upstream of the pre-miR-30d sequence and performed PCR analysis to ensure amplification of a single specific PCR product at the expected size (Figure 24-A, B). Since all designed primers yielded a single bands as visualized in the agarose gel, we have then performed qRT-PCR analysis with serially diluted mouse genomic DNA to further validate the amplification efficiency of the primers. After plotting the threshold cycle versus the primer dilution factor, we fit the data to a straight line and picked primer 7 which showed a correlation coefficient (R^2) of above 0.99 (Figure 24-C). To explore whether the promoter of *miR-30d* was methylated, we performed methylated DNA immunoprecipitation assay (MeDIP) with genomic DNA from MCECs. We observed a significantly higher methylation of the promoter of miR-30d in cells treated with TGF-β1 in comparison to untreated cells (Figure 24-D). To directly analyze the effect of miR-30d promoter methylation on miRNA expression, we used a luciferase reporter assay. The miR-30d promoter region was amplified and cloned upstream of the firefly luciferase into pCpGL vector, which is devoid of any CpG dinucleotides (Section 4.6.1). MCEC cells were transfected with the pCpGL vector and collected 48 hours post transfection. The putative miR-30d promoter significantly enhanced the luciferase activity (53-fold) compared to the empty vector. *In vitro* methylation of the miR-30d promoter using the CpG methylase kit (Zymo Research) significantly reduced the luciferase activity 48 hours post transfection (Figure 24-E). These findings further support our hypothesis that promoter methylation regulated miR-30d expression.

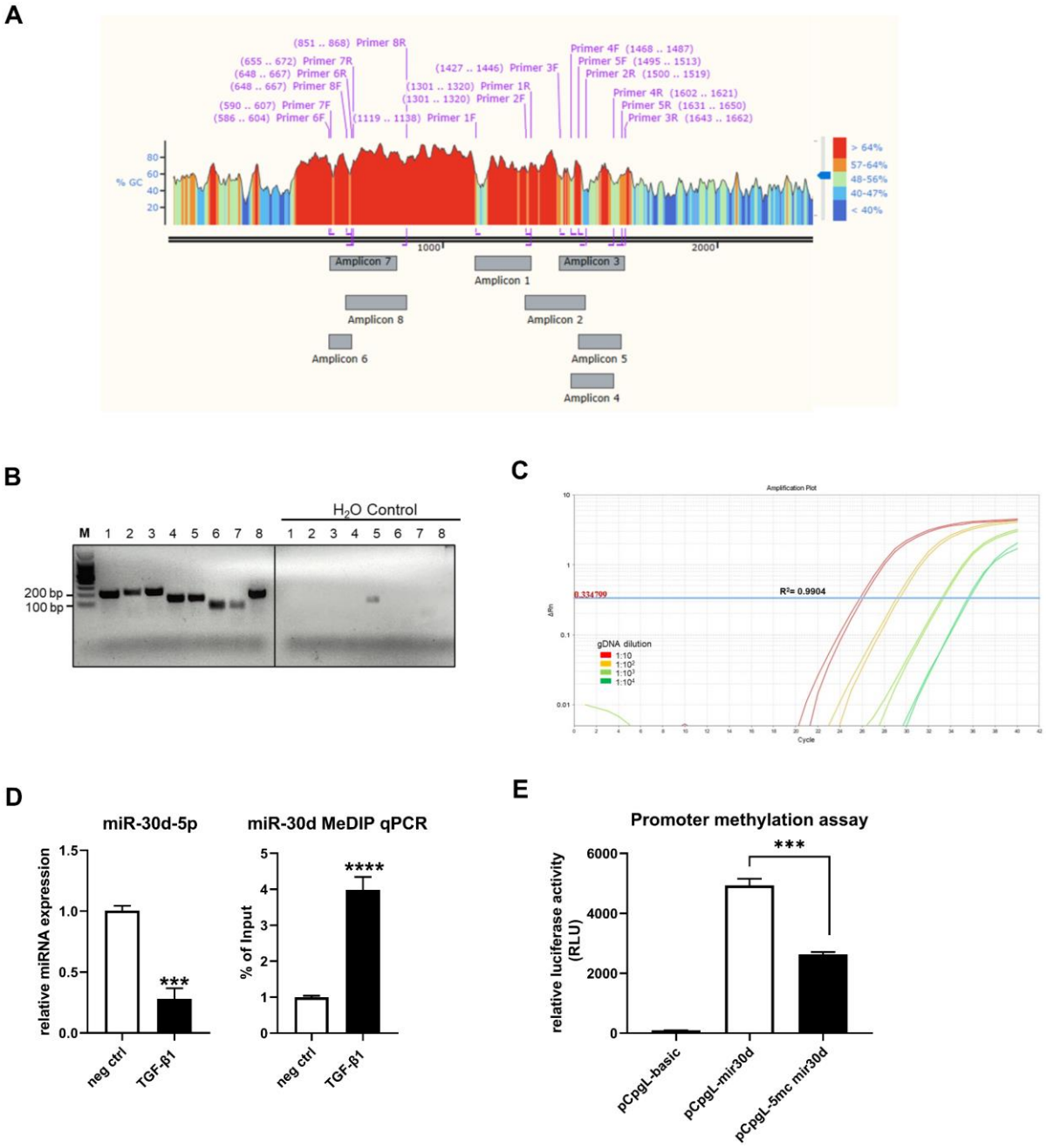

Figure 24: miR-30d promoter is methylated in fibrotic conditions. (A) Snapshot image of the identified promoter region (with high GC %) of miR-30d along with the location of the primer designed for methylation specific PCR. **(B)** 2% agarose gel of the PCR amplification of mouse gDNA with 8 primer pairs along with water control. **(C)** Snapshot image of qRT-PCR amplification plot of primer #7 tested with 10-fold dilutions of genomic DNA template for linearity of amplification. **(D)** (left) qRT-PCR analysis showing reduced miR-30d-5p expression 6 days after TGF-β1 treatment in MCEC cells. (right) Methylate DNA immunoprecipitation assay (MeDIP) of genomic DNA isolated from either treated or untreated cells showing significantly increased methylation of miR-30d promoter upon exposure to TGF-β1. **(E)** Luciferase promoter methylation assay showing increased luciferase activity upon transfection of cells with pCpGL-miR-30d promoter vector and significant reduction in luciferase

activity in MCEC cells transfected with pCpGL-methylated miR-30d promoter. Summarized quantitative findings are shown as the mean ±SEM. Statistical significance was calculated using an unpaired two tailed Student's t-test, and P-values correspond to ***p ≤ 0. 001, ****p ≤ 0. 0001. n= 3 biological replicates.

5.6.3 TET3 demethylates and rescues miR-30d expression

To test whether TET3 is an upstream regulator of miR-30d, we analyzed the methylation status of miR-30d promoter in *Tet3*$^{fl/fl}$*; Cdh5*$^{Cre-}$ mice in comparison to *Tet3*$^{fl/fl}$*; Cdh5*$^{Cre+}$ mice. MeDIP qRT-PCR of genomic DNA isolated from the mice heart tissue showed significantly elevated methylation levels of miR-30d promoter in *Tet3* knockout mice compared to control (Figure 25-A). We next aimed to explore whether TET3 overexpression can rescue miR-30d expression *in vitro*. As such, we treated MCECs with TGF-β1 followed by overexpression of TET3 at day 2 of TGF-β1 treatment. qRT-PCR analysis revealed loss of miR-30d expression in TGF-β1 treated cells transfected with an empty vector. Furthermore, overexpression of TET3 in TGF-β1 treated cells resulted in a significant increase and rescue of miR-30d expression (Figure 25-B). These results were in line with MeDIP qRT-PCR assay which showed increased methylation level in TGF-β1 treated cells. TET3 overexpression in TGF-β1 treated cells showed significantly reduced in promoter methylation levels (Figure 25-C). Altogether, these results show that TET3 induction can rescue miR-30d expression via promoter demethylation in fibrotic conditions.

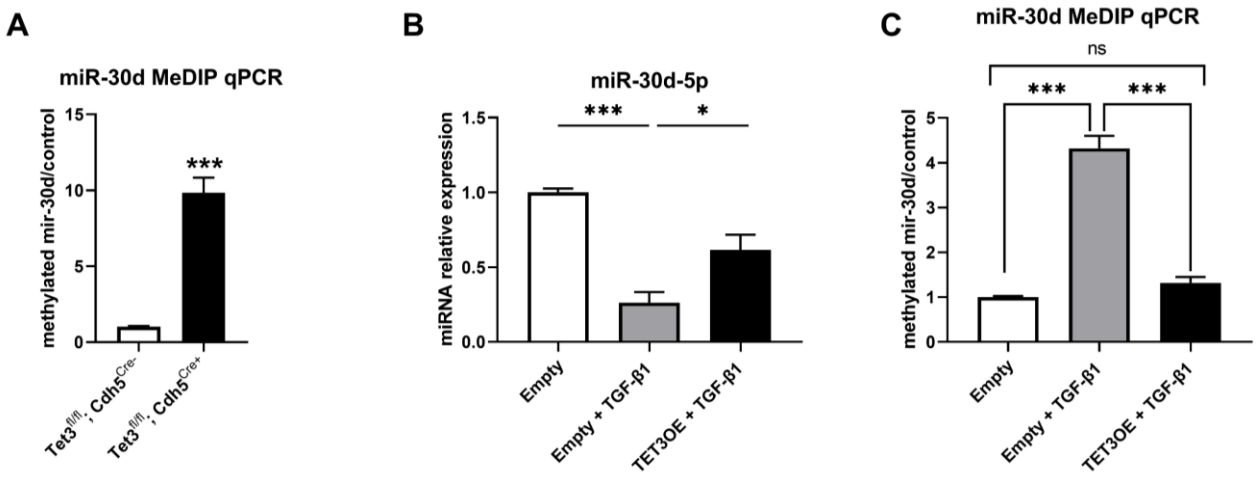

Figure 25: TET3 is an upstream regulator of miR-30d-5p. (A) MeDIP-qRT-PCR analysis of gDNA from heart tissue isolated from *Tet3$^{fl/fl}$; Cdh5^{Cre-}* mice in comparison to *Tet3$^{fl/fl}$; Cdh5^{Cre+}* mice. **(B)** qRT-PCR data showing the miR-30d expression levels in empty control vector-transfected and pCMV6-Tet3-transfected MCECs. TET3 overexpression (OE) resulted in rescue of miR-30d levels in TGF-β1 treated endothelial cells **(C)** MeDIP-qRT-PCR analysis of gDNA from MCECs. TGF-β1 treated cell transfected with empty control vector showed significantly higher methylation levels of miR-30d promoter in comparison with untreated cells. Transfection pCMV6-Tet3-vector resulted in the reduction of miR-30d promoter methylation. MeDIP results were calculated relative to input. Summarized quantitative findings are shown as the mean ±SEM. Statistical significance was calculated using an unpaired two tailed Student's t-test (A) and one-way ANOVA followed by Tukey multiple comparison test (B-C), and P-values correspond to *p ≤ 0. 05, ***p ≤ 0. 001. n= 3 biological replicates.

6 Gm*15749* forms an R-loop structure which recruits GADD45g and TET3 to demethylate the *Rasal1* promoter

6.1 lncRNA *Gm15749* regulates *Rasal1* expression

We have previously shown that the fibrosis suppressor gene *Rasal1* is downregulated in both kidney and cardiac fibrosis due to promoter methylation (Bechtel et al., 2010; Tampe et al., 2014, 2015; Xu et al., 2015, 2016). Moreover, recent unpublished data from our lab identified a lncRNA termed *Gm15749* which is located at the promoter region of the *Rasal1* mouse gene (Xu et al., 2017) (Figure 26-A). To further identify its mechanistic role, we first analyzed its transcript expression levels in comparison to *Rasal1*. qRT-PCR analysis of mouse cardiac fibroblasts revealed a significantly higher expression of *Gm15749* in comparison to *Rasal1* in normal conditions (Figure 26-B). Treatment of the cells with TGF-β1 to mimic fibrotic conditions showed significant down-regulation of both *Rasal1* and *Gm15749* mRNA levels at days 1,2 and 6 following treatment (Figure 26-C-D). Interestingly, Gm15479 downregulation was much more pronounced than *Rasal1* following treatment. As such, we hypothesized a possible protective role of the lncRNA by modulating the expression of *Rasal1*. We have previously demonstrated that *Rasal1* downregulation is reversible at earlier timepoints, but becomes irreversible once the *Rasal1* promoter is later methylated (Bechtel et al., 2010). And since *Gm15749* levels are lower, meaning the decrease of *Gm15749* transcript expression precedes *Rasal1* downregulation., we tested whether Gm15479 expression changes modulates *Rasal1* expression. As such, we utilized the shRNA silencing technique to knockdown *Gm15479*. Knockdown of *Gm15479* in mouse cardiac fibroblasts resulted in a significant decrease of *Rasal1* expression at the mRNA level (Figure 26-E) as well as at the protein level (not shown). Furthermore, MeDIP analysis revealed that the knockdown of *Gm15749* leading to *Rasal1* downregulation was due to the promoter methylation of *Rasal1* (Figure 26-F).

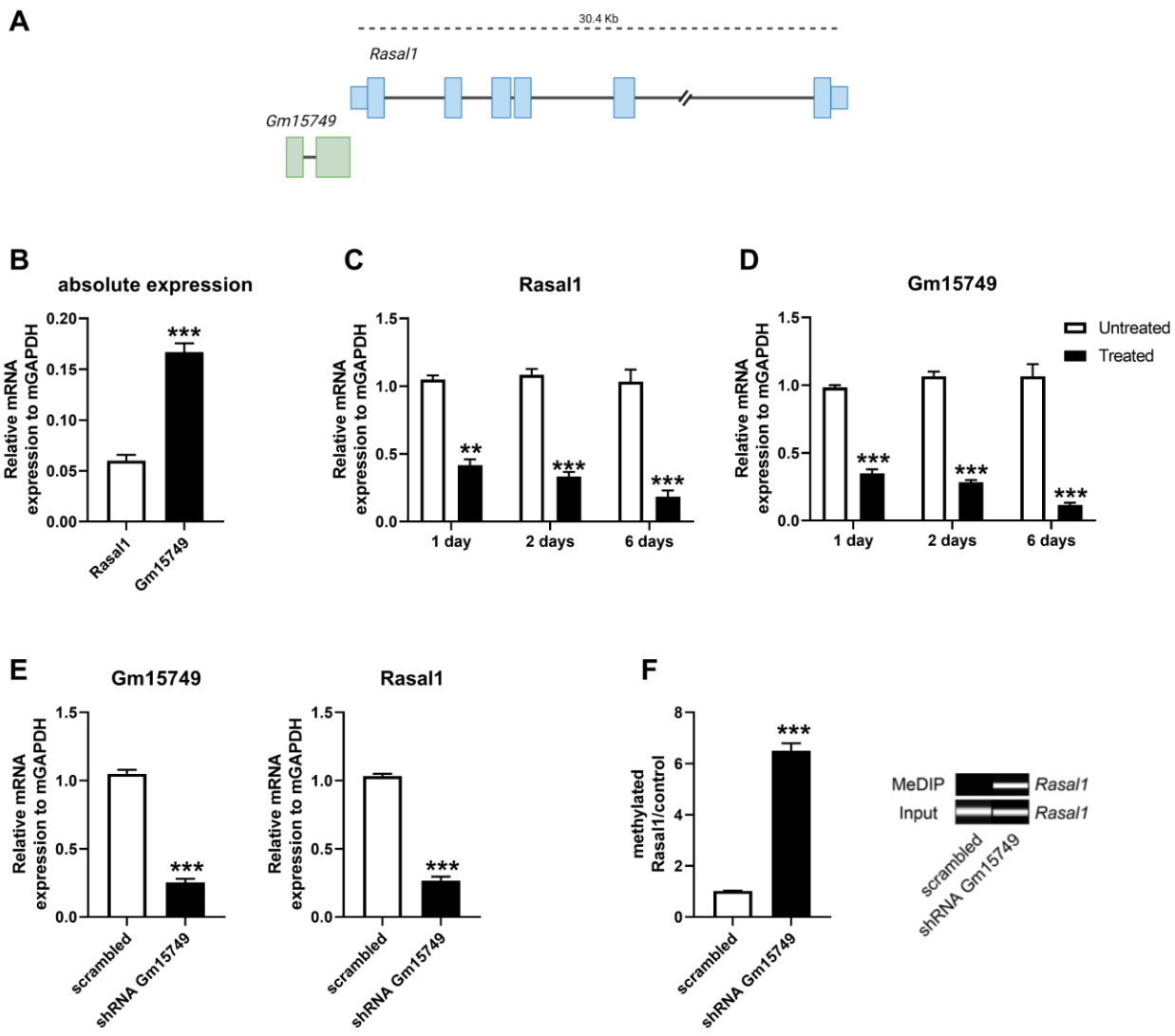

Figure 26: Summary of previous unpublished data. *Gm15749* lncRNA protects *Rasal1* promoter hypermethylation. (A) Schematic representation of *Rasal1* gene and *Gm15749* transcript location. **(B)** qRT-PCR of the absolute expression of *Rasal1* and *Gm15749*. **(C-D**) qRT-PCR of the relative mRNA expression of *Rasal1* and *Gm15749* following TGF-β1 treatment in MCFs. **(E)** qRT-PCR of the relative mRNA expression of *Rasal1* and *Gm15749* upon shRNA knockdown of *Gm15749* in MCFs. **(F) (Left)** MeDIP-qRT-PCR analysis of gDNA from MCFs transfected with either scrambled or shRNA Gm15749 knockdown construct. **(Right)** agarose gel of PCR products from MeDIP analysis of Rasal1 methylation. PCR products of control input DNA and immunoprecipitated DNA (5mC DNA) of MCFs transfected with either scrambled or shRNA Gm15749 knockdown construct.

6.2 *Gm15749* forms an R-loop at the *Rasal1* promoter

We have previously shown a positive association between *Gm15749* and *Rasal1* mRNA, which suggested that the expression of *Rasal1* is functionally connected to the transcription of

Gm15749. Specifically, we have shown that *Gm15749* activates *Rasal1* transcription by inducing its promoter's demethylation (unpublished data). *Gm15749* overlaps with the CpG island around the transcription start site of the *Rasal1* promoter (Figure 27-A). Previous reports show the formation of R-loops (DNA/RNA hybrids) by lncRNAs to aid the recruitment of demethylation proteins to specific promoters (Arab et al., 2019). Thus, we aimed to evaluate the presence of R-loops at the *Rasal1* promoter region. In this context, we immunoprecipitated mouse cardiac fibroblasts lysates with s9.6 antibody (a well-established R-loop binding antibody) and could detect an enrichment of R-loops at the 5'end of *Rasal1* (amplicon 2) promoter region (Figure 27-B). Treatment of cells with RnaseH1, which degrades RNA within DNA-RNA hybrids, resulted in significantly reduced levels of R-loops at the *Rasal1* promoter (Figure 27-B). To mimic fibrotic conditions *in vitro,* we treated MCFs with TGF-β1 for four days and observed significant loss of R-loop formation at the *Rasal1* promoter region (Figure 27-C). Next, we performed shRNA mediated *Gm15749* knockdown in MCFs to observe whether R-loops form in the absence of *Gm15749*. 48 hours post transfection, we showed sufficient depletion of *Gm15749* in cells transfected with the shRNA construct compared to scrambled control (Figure 27-D). Also, DRIP qRT-PCR analysis showed that shRNA transfected cells had significantly reduced levels of R-loops formed at the *Rasal1* promoter region compared to scrambled control transfected cells (Figure 27-E). These findings indicate that the lncRNA *Gm15749* forms an R-loop at the *Rasal1* promoter as a possible protective mechanism against methylation.

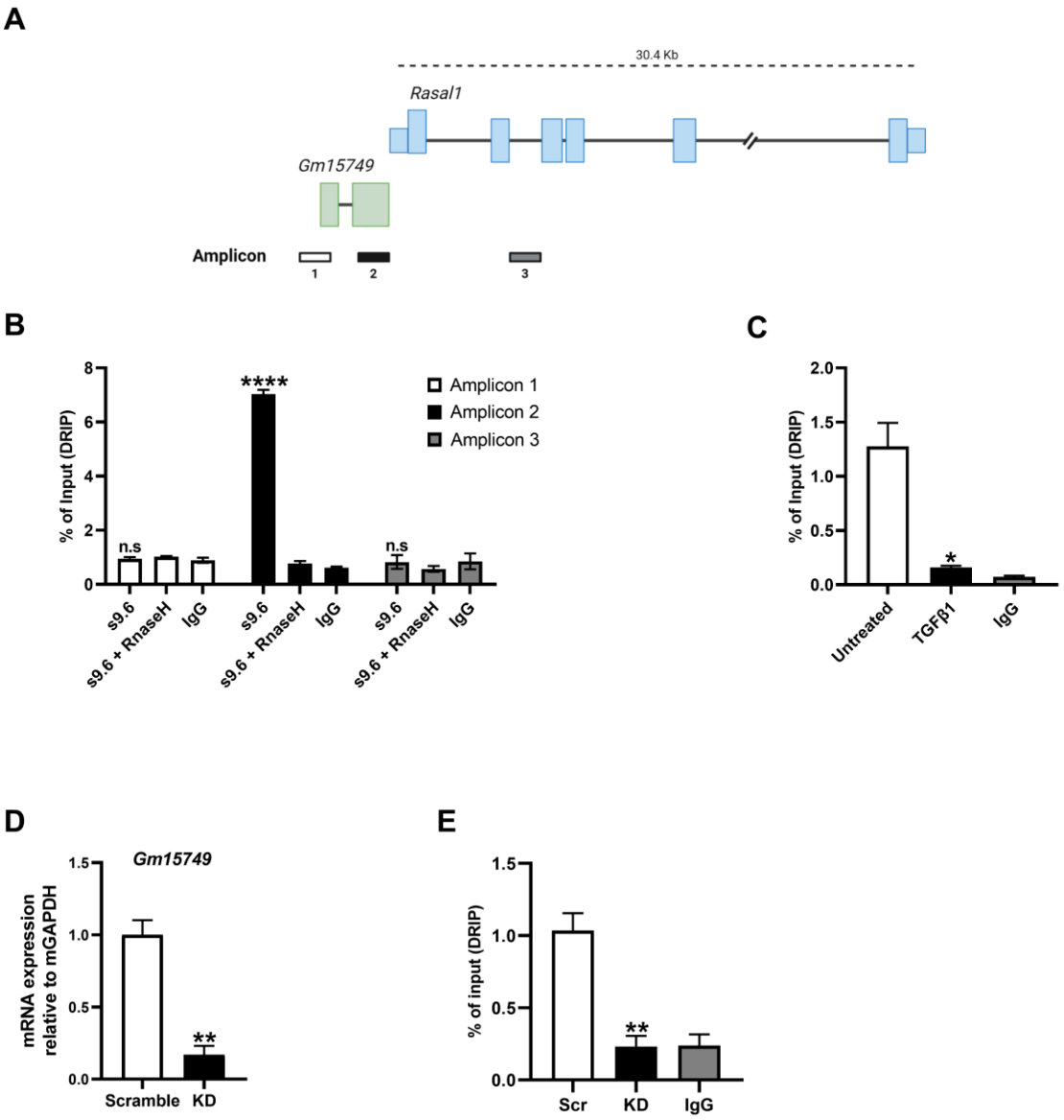

Figure 27: *Gm15749* forms and R-loop at the *Rasal1* promoter (A) The schematic illustrates the *Rasal1* gene and *Gm15749* transcript location and the position of the amplicons designed to detect R-loops. **(B)** DRIP qRT-PCR analysis at *Rasal1* promoter in MCF cells either treated or untreated with RnaseH and IgG pulldown control. **(C)** DRIP qRT-PCR analysis showing reduced R-loops upon treatment of MCFs with 4 days of TGFβ1. **(D)** qRT-PCR analysis confirming successful knockdown of *Gm15749* transcript upon shRNA transfection in comparison with scramble control. **(E)** DRIP qRT-PCR analysis showing reduced R-loops upon transfection of MCFs with shRNA targeting *Gm15749.* **(B-E)** Summarized quantitative findings are shown as mean ± SEM. Statistical significance was calculated using an unpaired two-tailed Student's t-test, and P-values correspond to ****P<0.0001, **P<0.01, *P<0.05, n.s not significant. n= 3 biological replicates.

6.3 *Gadd45g* is downregulated due to promoter methylation in aortic stenosis

Previous research has established that GADD45 proteins, which are stress response proteins involved in DNA repair, genomic stability, and apoptosis, also play a role in active DNA demethylation (Kienhöfer et al., 2015; X. Li et al., 2019; Z. Li et al., 2015; Niehrs & Schäfer, 2012). In an attempt to identify genes which regulated during the progression to heart failure, our working group identified *Gadd45g* (Growth arrest and DNA damage gamma) as a candidate gene which is downregulated and methylated in aortic stenosis patients (Figure 28-A). The study involved analyzing the transcriptome and methylome differential expression to identify genes which are silenced during the progression to aortic stenosis (AS). As such, heart tissue samples were retrieved from three groups of patients including: non-failing controls (group A), patients with AS presenting with preserved ejection fraction (group B), and patients with AS presenting with reduced ejection fraction (group C). Whole transcriptome analysis along with MeDIP sequencing was performed and the three different groups were compared by principal component analysis (PCA). A total of 2133 genes were downregulated at the RNA level in comparison to group A and 34 genes showed increased methylation levels. Overlapping both data sets results in 5 candidate genes which were both downregulated at the RNA level and had increased methylation levels in aortic stenosis patients (Figure 28- A). To further confirm that the reduction of *Gadd45g* is as a result of promoter methylation, we utilized a luciferase reporter assay as described before (section 4.6.4). *In vitro* methylation of the *Gadd45g* promoter significantly reduced the luciferase activity 48 hours post transfection in MCFs in comparison to unmethylated *Gadd45g* promoter (Figure 28-B). Therefore, these findings prove that the downregulation of *Gadd45g* observed in pathological conditions is due to promoter hypermethylation.

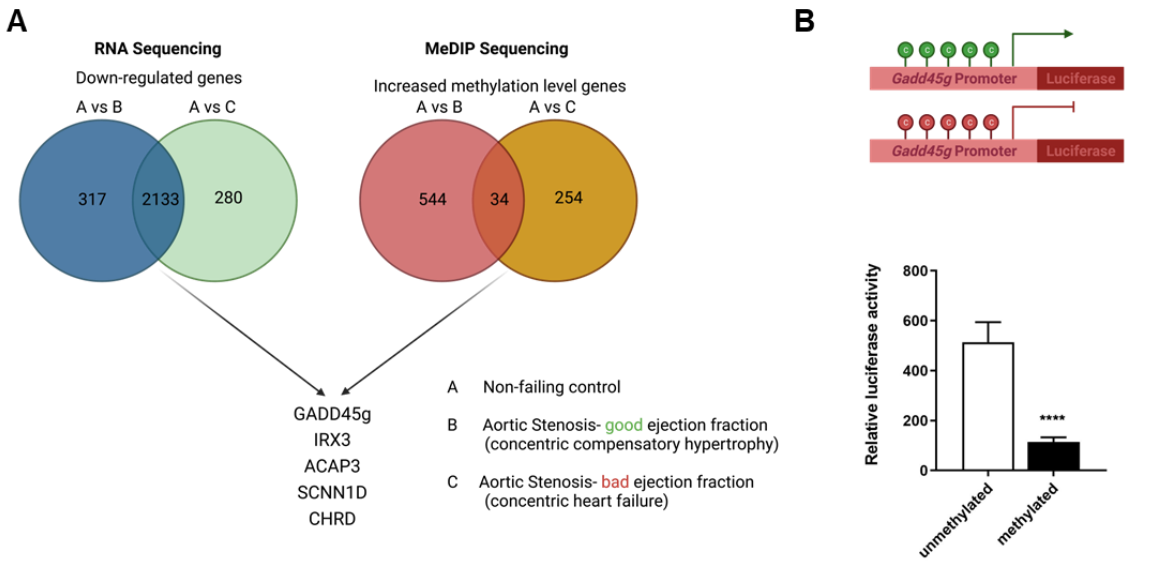

Figure 28: *Gadd45g* is downregulated in aortic stenosis. (A) Venn diagram summarizing the overlap between differentially expressed genes from RNASeq (left circle) and MeDIPSeq (right circle). 3 groups were compared to overlap downregulated genes with genes with increased methylation levels among groups A, B, and C.**(B)** Luciferase promoter methylation assay showing d significant reduction in luciferase activity in MCFs transfected with pCpGL-methylated miR-30d promoter in comparison to unmethylated promoter. Summarized quantitative findings are shown as mean ± SEM. Statistical significance was calculated using an unpaired two tailed Student's t-test and P-values correspond to ****P<0.0001, n= 3 biolog0ical replicates.

6.4 GADD45G is downregulated in a cardiac hypertrophy mouse model

In order to unravel key proteins involved in the demethylation process, we opted to evaluate the expression of GADD45 family of proteins in fibrotic conditions based on previous literature supporting their function in active DNA demethylation (Z. Li et al., 2015; Niehrs & Schäfer, 2012) along with the supporting data from the aortic stenosis study. For this purpose, 10–12-week-old C57BL/6N mice were implanted with osmotic minipumps infusing angiotensin II at a concentration of 1.5 mg/kg/d for 28 days. Mice treated with angiotensin II showed a significantly higher collagen deposition and overall fibrosis in comparison to vehicle mice (Figure 29-A-B). Immunofluorescence assessment revealed the presence of GADD45G in fibroblasts in control hearts and confirmed the loss of GADD45G expression upon angiotensin II treatment (Figure 29-C). Furthermore, mice treated with ATII showed clear reduction of *Gadd45g* mRNA levels but not *Gadd45a* or *Gadd45b* (Figure 29-D). Alterations in the expression of *Gadd45g* were also evaluated in TGF-β1-treated mouse cardiac fibroblasts as an *in vitro* model. Four days of TGF-β treatment is associated with significantly reduced

Gadd45g mRNA expression (Figure 29, E-F). Thus, the results indicated that GADD45g is downregulated in fibrotic conditions following TGF-β1 treatment in mouse cardiac fibroblasts and angiotensin II treatment in mice.

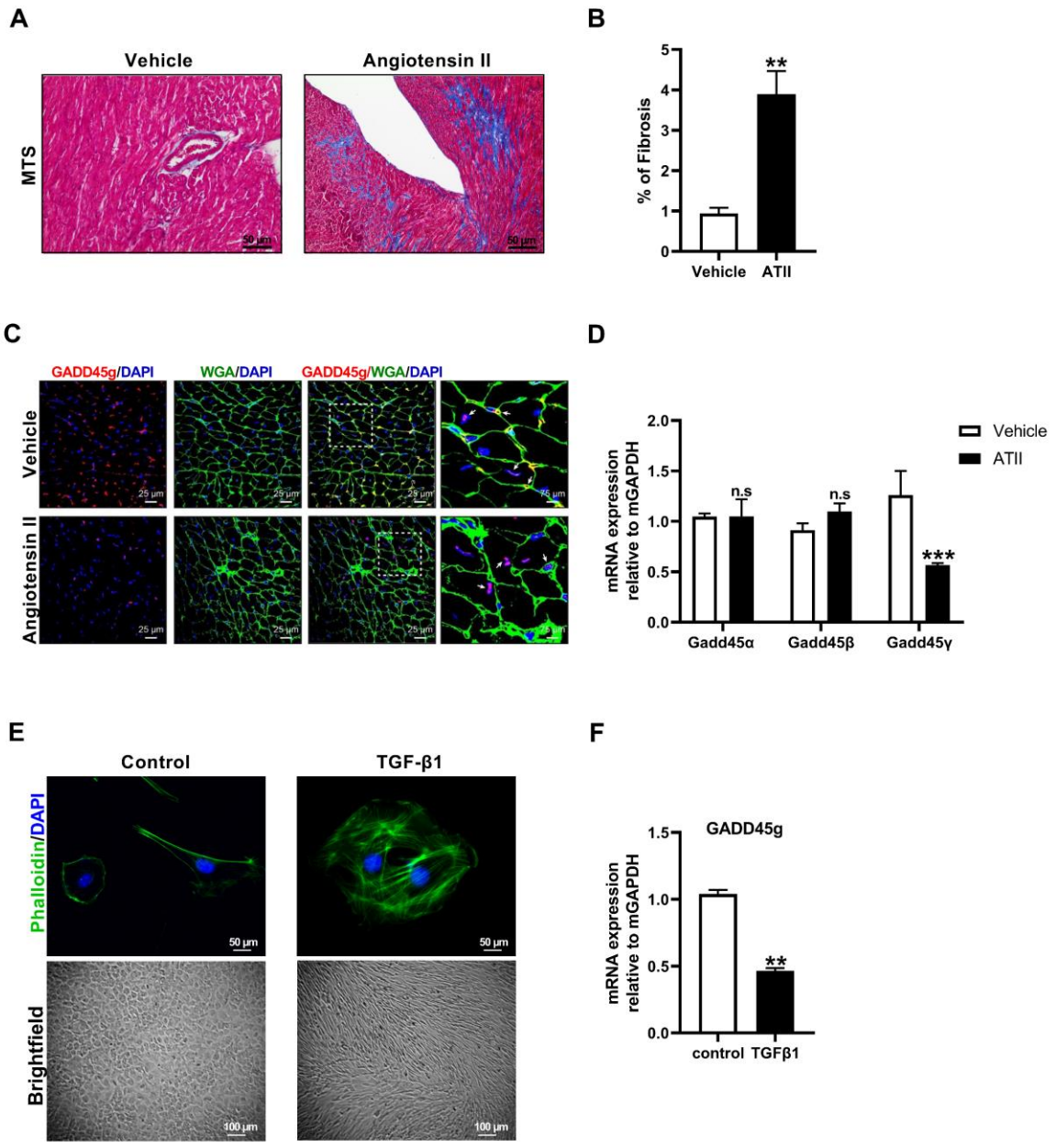

Figure 29: Reduced GADD45G protein and mRNA levels in fibrotic conditions. 10–12-week-old mice were subjected to either angiotensin II or PBS minipump implantation. The mice were sacrificed after 4 weeks, and heart tissue sections were used to confirm fibrosis. **(A)** Masson Trichrome staining (MTS) showing increased collagen deposition (in blue) upon angiotensin II treatment. **(B)** Graph of quantification of the overall fibrotic area shows significantly more fibrosis in angiotensin II-treated

mice **(C)** Immunofluorescence images of heart sections stained with GADD5G antibody and WGA to label the cell membrane. **(D)** qRT-PCR analysis of *Gadd45* mRNA levels shows significant downregulation of *Gadd45g* only upon angiotensin II treatment in comparison with PBS treated mice. **(E)** Phalloidin staining of *in vitro* TGFβ1 treated MCF shows activation of fibroblasts as seen by increased actin filament formation. **(F)** qRT-PCR analysis revealing significant downregulation of *Gadd45g* upon treatment of MCF cells with TGFβ1. (B, D, F) Summarized quantitative findings are shown as mean ± SEM. Statistical significance was calculated using an unpaired two tailed Student's t-test and P-values correspond to **P<0.01, ***P<0.001, n.s not significant. n= 3 biological replicates.

6.5 GADD45G is recruited by *Gm15749* to the *Rasal1* promoter

Since GADD45 proteins have been shown to have RNA binding characteristics and are associated with chromatin (Carrier et al., 1999; Sytnikova et al., 2011), we hypothesized that *Gm15749* recruits and guides GADD45 to the *Rasal1* promoter. To test our hypothesis, we performed a ChIP assay, which showed GADD45G enrichment at the *Rasal1* promoter, but not in the IgG control pull down as detected by qRT-PCR. Interestingly, treatment of cells with RnaseH, which degrades R-loops, revealed loss of GADD45G occupancy at the *Rasal1* promoter (Figure 30-A). To monitor the interaction of *Gm15749* and GADD45G *in vitro*, we immunoprecipitated GADD45G from MCF cells using RNA immunoprecipitation assay (RIP) and revealed by qRT-PCR specific binding of GADD45G with *Gm15749* (Figure 30-B). Furthermore, we performed an RNA electrophoretic mobility shift assay (RNA-EMSA) to confirm the physical interaction between *Gm15749* and GADD45G *in vitro*. RNA-EMSA showed a shift upon incubation of the reaction with biotin labelled *Gm15749* and recombinant GADD45G protein in a dose-dependent manner, indicating their direct interaction. This shift in the gel was further reduced upon competition with the unlabeled *Gm15749* confirming that the interaction is specific (Figure 30-C).

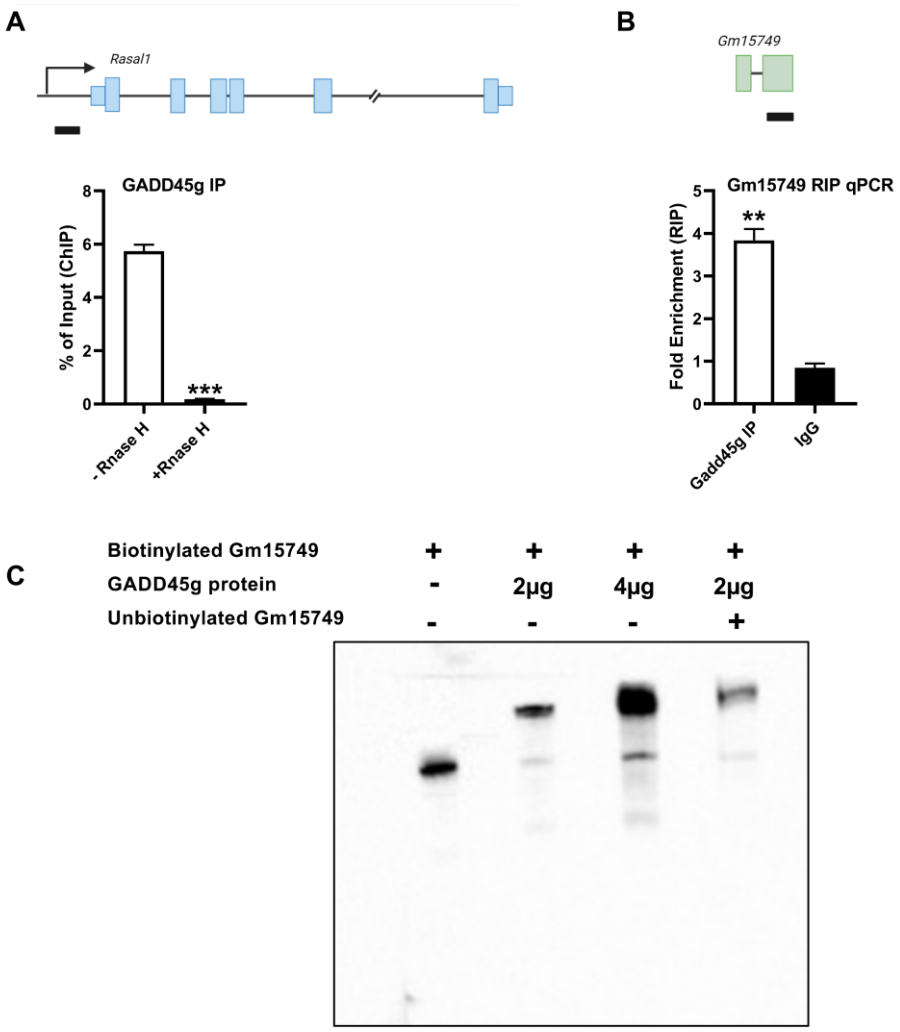

Figure 30: GADD45g is recruited to the *Rasal1* promoter (A) The schematic shows the position of the amplicon (in black) to detect binding of GADD45g to the *Rasal1* promoter. ChIP qRT-PCR indicates occupancy of GADD45g at the *Rasal1* promoter which is lost upon treatment of MCF cells with RNaseH. **(B)** RIP-qRT-PCR monitoring interaction of GADD45G and *Gm15749*. **(C)** RNA-EMSA showing binding of Gm15479 to GADD45G. Biotin-labelled *Gm15749* was incubated with different concentrations recombinant GADD45G to show dose dependent binding. Competitive EMSA in the fourth lane showing reduced shift in the assay upon incubation of the reaction with unbiotinylated *Gm15749*. **(A, B)** Summarized quantitative findings are shown as mean ± SEM. Statistical significance was calculated using an unpaired two tailed Student's t-test, and P-values correspond to ***P<0.001, **P<0.01. n= 3 biological replicates

6.6 TET3 physically interacts with GADD45G

We have previously shown that the aberrant *Rasal1* methylation can be specifically reversed by TET3-mediated hydroxymethylation specifically (Tampe et al., 2014; Xu et al., 2018). We have also identified TET3 binding to the CXXC motif of the *Rasal1* promoter. Several reports

have highlighted the importance of the cooperation of TET enzymes and GADD45 proteins as a prerequisite of the demethylation of a number of genes in the mouse brain (Guo et al., 2011; Ma et al., 2009). As such, we hypothesized that both GADD45G and TET3 interact together to initiate site specific demethylation especially that they are both recruited to the *Rasal1* promoter. This hypothesis is further supported by previous reports that show an interaction of GADD45a with TET1 at the TCF21 promoter to direct site-specific demethylation (Kienhöfer et al., 2015). To test our hypothesis, we performed a co-immunoprecipitation assay (Co-IP) in mouse cardiac fibroblasts, which showed direct physical interaction of GADD45G and TET3 as compared to IgG control (Figure 31-A). Moreover, co-immunofluorescence of TET3 and GADD45G in mouse cardiac fibroblasts revealed their colocalization in the nucleus (Figure 31-B). This data suggests that TET3 and GADD45G are recruited to the *Rasal1* promoter region and interact together to initiate the protective demethylation process.

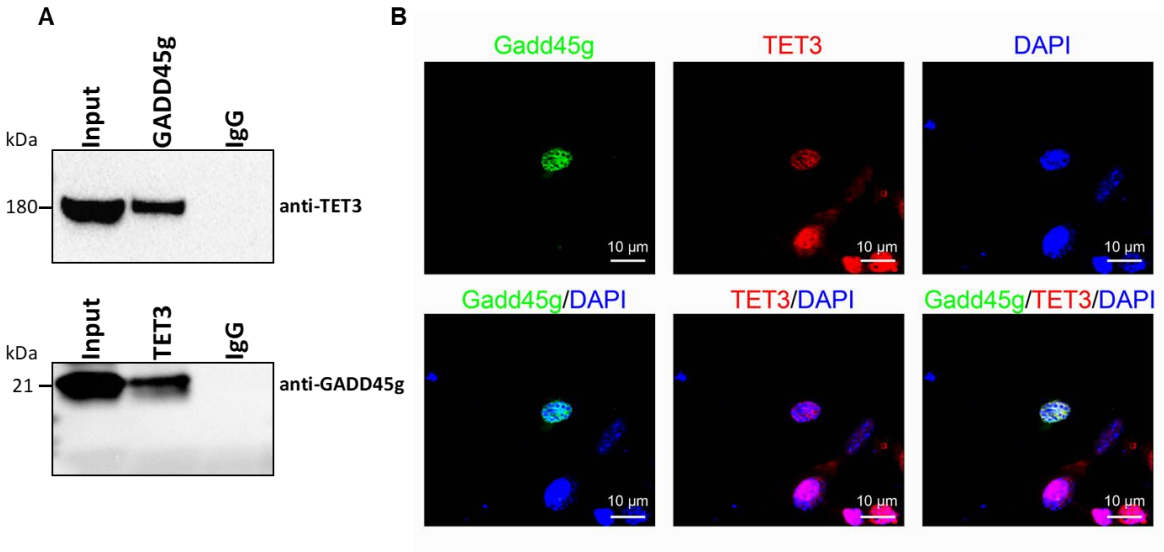

Figure 31: **GADD45G physically interacts with TET3. (A)** Representative immunoblotting for co-immunoprecipitation of GADD45G and TET3 in MCFs confirming their interaction. **(B)** Co-immunofluorescence staining of GADD45G (green) and TET3 (red) in MCF cells revealing their colocalization in the nucleus as seen by the overlay with the nuclear staining DAPI (blue). Scale bar represents 10 µm.

7 Discussion

7.1 Endothelial TET3 regulates EndMT and cardiac remodeling

The present study investigated the effect of the endothelial-specific deletion of *Tet3* in a mouse model on cardiac function and remodeling. Endothelial cells, being among the most abundant cells in the heart, are crucial players in normal cardiac physiology as well as pathology (Gogiraju et al., 2019). The contribution of endothelial cells to the fibrotic process by EndMT has been described in cardiovascular diseases such as pressure overload, pulmonary hypertension and atherosclerosis (P. Y. Chen et al., 2015; Zahid et al., 2020; Zeisberg, Tarnavski, et al., 2007), in addition to kidney and pulmonary fibrosis and cancer (Hashimoto et al., 2010; Zeisberg et al., 2008; Zeisberg, Potenta, et al., 2007). However, the molecular signatures required to drive EndMT are not yet fully understood. Furthermore, EndMT, which was originally described as a developmental process, is also a cellular differentiation process which requires extensive differential gene expression to result in the mesenchymal phenotype. Since the diseases that are associated with EndMT are also regulated by epigenetic modifications, EndMT itself could be controlled by epigenetics (Hulshoff et al., 2018). We have previously reported that TET3 can rescue *Rasal1* expression by promoter hydroxymethylation resulting in the reversal of EndMT and subsequent attenuation of fibrosis (Tampe et al., 2014, 2015; Xu et al., 2015). Yet, exactly how TET3 can modulate EndMT is poorly understood, especially since there are more than 9000 genes targeted by *Tet3* (Bian & Yu, 2014). Therefore, we generated an endothelial-cell specific *Tet3* knockout mouse model, which to the best of our knowledge is the first of its kind, to further understand the contribution of *Tet3* to EndMT.

7.1.1 Deletion of *Tet3* in endothelial cells

Prior to the generation of an endothelial-cell specific *Tet3* knockout mouse model, we performed a number of experiments to validate the "floxing" strategy from the purchased transgenic mouse line (C57BL/6JSmoc-Tet3$^{tm1.1Smoc}$), which possesses loxP sites flanking exon 4 of the *Tet3* gene. We performed extensive set of experiments including genotyping PCR, long range PCR, Sanger sequencing, and *in vitro* Cre recombination to validate the correct location of loxP sequences flanking exon 4 and efficient site-specific recombination

upon addition of Cre recombinase (Figure 9-10). Prior to breeding the floxed mice with a Cre-recombinase expressing mouse line, we developed a simple *in vitro* model by utilizing isolated cardiac fibroblasts from *Tet3*$^{fl/fl}$ mice transduced with AAV-expressing Cre recombinase virus and evaluated Cre recombination efficiency (Figure 11). This was based on several reports, which confirmed the feasibility of using viral systems as an "easy to use Cre recombinase *in vitro* delivery system" (Sengupta et al., 2017). Upon transduction of *Tet3*$^{fl/fl}$ cardiac fibroblasts and subsequent DNA isolation and PCR amplification using primers designed to amplify the region flanked by loxP site, we were able to detect a smaller PCR product (~310 bp) corresponding to the successful Cre recombination and deletion of the sequence flanked by loxP sites. Notably, although we used the AAV-DJ serotype, which is known for its high transduction efficiency, we still detected a PCR product of ~1228bp which corresponded to a floxed allele that did not undergo Cre-mediated recombination. This can be explained by the fact that not all the cells were efficiently transduced with AAV-virus. This was further validated by utilizing AAV expressing GFP virus and observing only around 75% transduction efficiency (Green fluorescent cells where counted - data not shown). Altogether, these experiments were able to validate the *Tet3*$^{fl/fl}$ transgenic mouse line, which is capable of Cre-mediated site-specific recombination resulting in the deletion of the loxP sites flanking exon 4 of the *Tet3* gene, thereby creating null alleles.

Furthermore, to remove TET3 in endothelial cells, we utilized a commercially available and well- characterized endothelial-cell driven Cre recombinase mouse line (Alva et al., 2006). Although, *Cdh5* expression is mainly restricted to the endothelium, a subset of hematopoietic cells will also express Cre. However, in comparison with other endothelial-cell driven Cre transgenic mice, which have unspecific Cre expression in neurons, muscle, hematopoietic cells, and mesoderm, this strain retains almost exclusive endothelial expression (Gustafsson et al., 2001; Kisanuki et al., 2001; Motoike et al., 2003).

Tet3$^{fl/fl}$ mice were subsequently bred with *Cdh5*$^{Cre+}$ mice to generate an endothelial-cell specific *Tet3* knockout mouse line. Upon endothelial specific deletion of *Tet3*, we did not observe any loss of homozygous off-spring after birth. The offspring generated from the breeding were evaluated for deviations in the inheritance frequency. Both F1 and F2 generations showed the expected genotype distribution following Mendelian ratios (Figure

12). Moreover, we could successfully detect Cre recombinase expression in the isolated heart tissue of *Tet3*$^{fl/fl}$*; Cdh5*$^{Cre+}$ mice. To confirm specific deletion of TET3 in endothelial cells, we monitored both Tet3 mRNA and protein expression in the heart tissue of *Tet3*$^{fl/fl}$*; Cdh5*$^{Cre+}$ mice in comparison to *Tet3*$^{fl/fl}$*; Cdh5*$^{Cre-}$ mice. Histological analysis confirmed the reduction of TET3 protein levels in endothelial cells only and FACS analysis confirmed significant loss of *Tet3* mRNA expression in Cdh5(+) sorted endothelial cells in *Tet3*$^{fl/fl}$*; Cdh5*$^{Cre+}$ compared to *Tet3*$^{fl/fl}$*; Cdh5*$^{Cre-}$ mice. As such, both *in vitro* and *in vivo* experiments done could validate the generation of a transgenic mouse line in which *Tet3* was efficiently deleted in endothelial cells.

7.1.2 Relevance of the observed phenotype

In order to elucidate the effect of the loss of *Tet3* in endothelial cells, we evaluated the observed macroscopic phenotype as well as cardiac function in knockout mice in comparison to control. *Tet3* knockout mice displayed enlarged heart size which was evident from the macroscopic view and cross-sectional area and a larger left ventricle mass compared to control mice (Figure 15). To rule out the bias from measuring left ventricular mass alone due to differences in body weight, we compared the heart weight to body weight ratio (HW/BW) and could also reveal an increased ratio (HW/BW) in *Tet3* knockout mice compared to control (Figure 15).

To determine the impact of the increased left ventricular size, we evaluated cardiac function by echo analysis. *Tet3* knockout mice showed reduced systolic function compared to control mice with reduction in both ejection fraction and fraction area shortening (Figure 16). Interestingly, male *Tet3* knockout mice had a worse systolic function compared to female knockout mice. This may be due to several factors, which have been previously reported and provided evidence for a possible protection against cardiac hypertrophy in baseline and challenge conditions in female mice compared to male mice (Gabel et al., 2005; Zhao et al., 2019) . Furthermore, we evaluated the relative wall thickness to differentiate the type of cardiac remodeling. *Tet3* knockout mice showed elevated posterior wall thickness and septum thickness, which resulted in a significantly higher relative wall thickness in comparison to control mice (Figure 17). This was indicative of a concentric type of remodeling upon *Tet3* knockout in endothelial cells. There are no reports, which have previously evaluated the loss

of *Tet3* in endothelial cells on cardiac function. However, a recent study which investigated the role of TET2 in cardiac remodeling by using a *Cdh5-CreERT2/TET2*$^{fl/fl}$ transgenic mice revealed a systolic dysfunction in *Tet2* endothelial knockout mice depicted by reduced ejection fraction and increased left ventricular inner systolic diameter (Wenxin Kou et al., 2022). Nevertheless, the investigators could only report a cardiac phenotype upon challenging of the mice with transverse aortic constriction and not at baseline conditions. This suggests that the phenotype we observe in *Tet3* endothelial knockout mice at baseline conditions is more aggravated in comparison to *Tet2* endothelial knockout mice. Taken together, these findings validate the contribution of TET enzymes to normal cardiac function and highlight the need to further investigate the mechanism behind this protective effect in the heart. One must also take into consideration the background of the mouse strain used in the experiments and its impact on cardiac function. C56BL/6J mice, which have been used here, were reported to respond better to pressure overload challenge (TAC- transverse aortic constriction) and have higher survival rates than C56BL/6N mice (Garcia-Menendez et al., 2013; Mekada & Yoshiki, 2021; Zhao et al., 2019) This could also explain why some echo parameters where not significantly different in knockout mice compared to control mice and why female knockout mice had a milder phenotype. Since the mouse model used results in the loss of TET3 in all endothelial cells and is not exclusive for cardiac endothelial cells, we cannot rule out the contribution of other organs to the observed phenotype. Further studies investigating the effect of *Tet3* knockout in endothelial cells on other organs will be performed in the future.

We have previously reported that by inducing *Tet3* expression via BMP7, *Rasal1* expression can be rescued resulting in reduced EndMT and cardiac fibrosis. (Xu et al., 2015). As such, we assessed the degree of cardiac fibrosis in knockout mice and could observe a significantly higher overall fibrosis compared to control mice (Figure 18). Additionally, we detected a much more pronounced perivascular fibrosis with increased collagen deposition around capillaries and vessels using immunofluorescence staining (Figure 18). These findings showed that deficiency of TET3 in endothelial cells contributes the fibrosis progression in the heart. This can possibly be due to a contribution of endothelial cells to the fibroblast population upon EndMT due to loss of TET3. Exactly how TET3 regulates EndMT was then further examined.

7.1.3 Relevance of TET3 in EndMT

Based on the previous results, which showed elevated fibrosis levels in *Tet3* knockout mice, we sought to evaluate the expression of EndMT markers especially since we observed more intense collagen deposition around endothelial cells. Our results revealed significantly upregulated EndMT marker expression along with increased α-SMA expression in the heart tissue of knockout mice compared to control (Figure 19). These results were in accordance with the observed increase in α-SMA protein levels in the immunofluorescence staining of *Tet3* knockout mice heart sections (Figure 18). Interestingly, we observed a substantially higher *Snail* upregulation compared to the other EndMT markers (*Slug* and *Twist*) and hypothesized that *Tet3* could be an upstream regulator of *Snail* expression. These findings were in line with previous studies, which also reported a significant increase in *Snail* expression upon *Tet3* knockout in melanoma and ovarian cancer contributing to EMT (Gong et al., 2017; Ye et al., 2016) . To detect further molecular alterations in *Tet3* knockout mice, it would be crucial to perform unbiased RNA sequencing analysis and unveil differential transcriptome expression upon *Tet3* knockout. Also, advanced single-cell RNA sequencing could provide a high-resolution transcriptome analysis of the endothelial cells which are undergoing EndMT and give further proof of our proposed hypothesis. This, coupled with the spatial transcriptomics can reveal spatiotemporal gene expression patterns at a single-cell resolution.

7.1.4 miR-30d a novel downstream target of TET3

In order to unravel the mechanism behind the drastic upregulation of *Snail* expression in *Tet3* knockout mice, we searched the literature to identify possible targets that can inhibit *Snail* expression. Looking into EMT studies in cancer, we identified a miRNA termed miR-30d, which binds to the 3'UTR of *Snail* and inhibits its expression and which is associated with better prognosis (Xu et al., 2021; Ye et al., 2015, 2016). We found reduced miR-30d expression levels upon *Tet3* knockout in endothelial cells (Figure 20). miR-30d has been recently described in cardiac research as a novel cardioprotective miRNA, capable of reversing pathological cardiac hypertrophy and regulating cardiac remodeling (Holley et al., 2021; J. Li et al., 2021, 2022; Xiao et al., 2017). To further investigate the role of miR-30d in pathological hypertrophy, we found significantly reduced miR-30d and *Tet3* expression in angiotensin II

treated mice in comparison to control mice (Figure 21). This finding is in accordance with a recent study, which also reported reduced miR-30d expression in angiotensin II treated mice as well as in other cardiac hypertrophy models such as TAC and isoproterenol infusion suggesting that it might play a role in modulating cardiac hypertrophy (J. Li et al., 2022). We could also detect significantly reduced miR-30d and *Tet3* expression in fibrotic conditions *in vitro* (Figure 22). In line with our findings, two studies investigated miR-30d expression upon TGF-β1 exposure, and also revealed lower expression in human umbilical vein endothelial cells (HUVEC) and ovarian cancer cells in fibrotic conditions (Ciavarella et al., 2021; Ye et al., 2016). However, there has been no report correlating miR-30d expression with EndMT in the fibrotic conditions in the heart yet. Furthermore, the bioinformatic analysis carried out by TargetScan identified *Snail* among the predicted targets of miR-30d-5p. We were able to demonstrate that miR-30d-5p directly binds to the 3'UTR of *Snail* and reduces its expression *in vitro* (Figure 23). These results indicated that miR-30d is a negative regulator of EndMT by targeting *Snail*.

7.1.5 Rescue of miR-30d by TET3 as a possible therapeutic approach

TET enzymes work by mediating the hydroxymethylation of cytosine residues at active genomic regions resulting in rescuing target gene expression. Since miR-30d expression was significantly reduced in $Tet3^{fl/fl}$; $Cdh5^{Cre+}$ mice as well in fibrotic conditions, we wanted to explore whether the promoter of miR-30d is methylated leading to the observed reduction of miR-30d. This hypothesis is supported by several studies, which reported that miRNAs can be epigenetically regulated by promoter hypermethylation via DNMT enzymes similar to genes (Aure et al., 2013; Piya et al., 2021; Zare et al., 2018). For example, hypermethylation of miR-145 mediated by DNMT1 is associated with increased inflammation and atherosclerosis progression (Zhong et al., 2018). In fact, the study showed that this pathological process can be reversed by *Tet2* overexpression which elevated miR-145 expression. Furthermore, promoter methylation of miR-30 family precursor genes was reported in head and neck squamous carcinoma, breast cancer, and pancreatic cancer (Aure et al., 2013; Azmi et al., 2019; Saleh et al., 2019).

To test whether miR-30d expression is regulated by promoter methylation, we identified the promoter region of miR-30d with high GC content located upstream of the sequence of the precursor miR-30d gene. We revealed significant increase in the methylation of miR-30d in TGF-β1 treated MCECs as well as in *Tet3* knockout mice. We also determined that the reduction of miR-30d expression was mediated by methylation (Figure 24-25). To date, only one study in ovarian cancer proposed that promoter methylation silences miR-30d (Ye et al., 2016)., However, there has been no report about reduced expression of miR-30d due to aberrant promoter methylation in correlation with EndMT in the heart. To further identify how miR-30d is regulated by promoter methylation, it would be important to identify which DNMT enzyme is associated with the addition of the methylation mark both in TGF-β1 treated MCECs and endothelial *Tet3* knockout mice. Moreover, a genome wide DNA methylation profiling would provide unbiased evidence regarding our hypothesis, and also reveal differential DNA methylation patterns across several genes and non-coding RNAs in the knockout mouse model.

Based on our previous findings, we hypothesized that TET3 could be an upstream regulator of miR-30d, since miR-30d is reduced due to promoter hypermethylation in endothelial *Tet3* knockout mice. We showed that induction of TET3 resulted in the demethylation of miR-30d promoter and subsequent restoration of miR-30d expression in fibrotic conditions (Figure 25) To further corroborate our hypothesis, we browsed the ChIP-Atlas and performed unbiased analysis using the mouse TET3 ChIP sequencing database from embryonic stem cells (Figure 31). Interestingly, we could identify TET3 enrichment at the identified promoter region of miR-30d. It has been previously reported that TET3 is tethered to the transcription start sites of target genes via the CXXC domain binding to 5'- CACGTG-3' motif, also known as the E-box motif (Jin et al., 2016; Ravichandran et al., 2022). ChIP seq revealed that enriched TET3 peaks at the promoter region of miR-30d were found in association with the binding motif of TET3 5'-CACGTG-3' sequence.

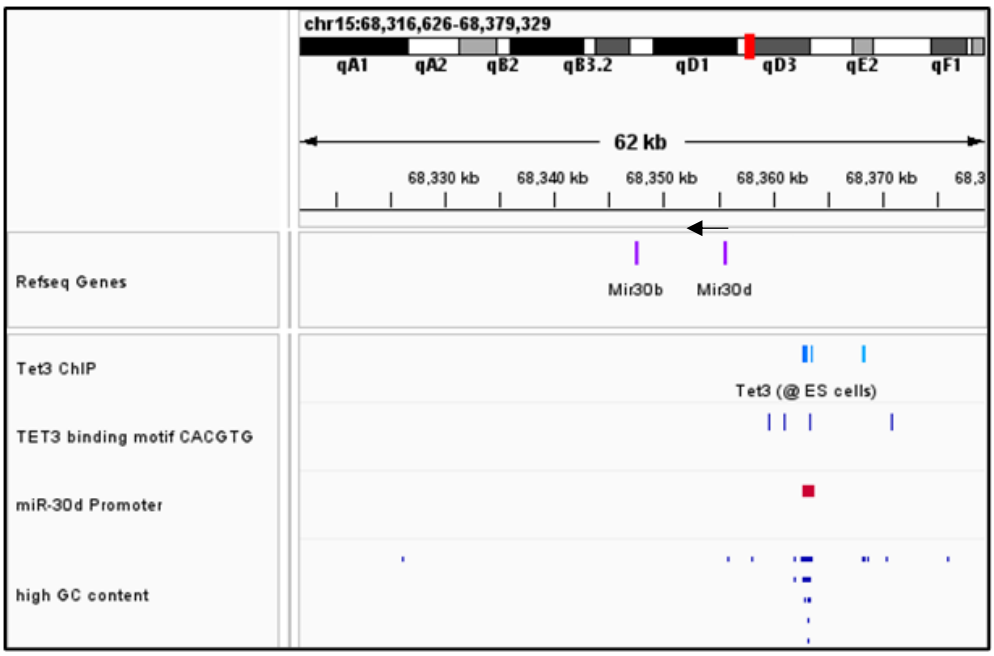

Figure 32: ChIP seq reveals binding of TET3 to miR-30d promoter. ChIP-atlas peak browser (http://chip-atlas.org/) data showing TET3 ChIP seq peaks in embryonic stem cells. TET3 is enriched at the promoter region of miR-30d precursor promoter sequence Lane 1 represents the mouse GRCm38/mm10 reference genome. (Black arrow designates transcription direction). Lane 2 represents TET3 ChIP peaks at the selected region. Lane 3 represents the TET3 binding motif sequence 5'-CACGTG-3'. Lane 4 represents the predicted miR-30d promoter sequence. Lane 5 shows the regions with high GC content.

In summary, we provide evidence for the first time that the loss of TET3 in endothelial cells is associated with a worsened cardiac phenotype. Specifically, endothelial Tet3 knockout mice had an enlarged left ventricle accompanied by worsened systolic function and increased deposition of collagen around the vessels. By examining the molecular mechanisms underlying the observed phenotype, we found that the EndMT marker *Snail* was markedly elevated. Therefore, we sought to identify a downstream molecule that can inhibit *Snail* expression under normal conditions. We identified that miR-30d binds to the 3'-UTR of Snail and reduces its expression thereby controlling EndMT. In addition, we found that loss of TET3 is associated with promoter hypermethylation and silencing of miR-30d (Figure 32). These findings suggest a novel possible anti-fibrotic therapeutic mechanism mediated by TET3, which hydroxymethylates and rescues miR-30d expression.

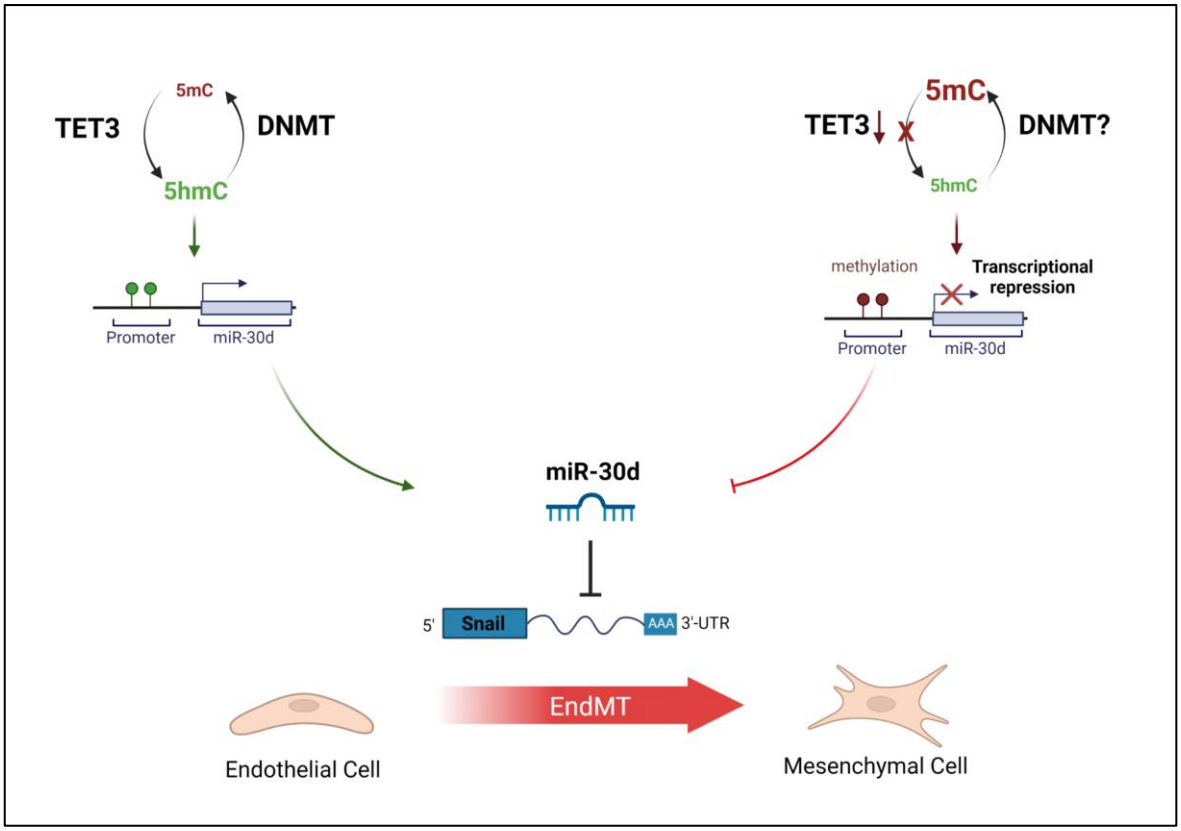

Figure 33: TET3 regulates EndMT by demethylating miR-30d, which inhibits expression of *Snail*. Under physiologic conditions, cytosine bases within the pri-miR-30d CpG island promoter are unmethylated, and miR-30d is open for transcription. miR-30d then binds to the 3'-UTR of *Snail*, resulting in its inhibition and the subsequent restriction of EndMT. Upon loss of TET3, the protective inhibitory effect of miR-30d is compromised owing to promoter methylation, resulting in the progression of EndMT via the activation of *Snail*.

7.2 Relevance of *Gm15479* in directing the hydroxy-methylating effect of TET3

Although TET3's demethylating role is well characterized, not much is known about how it is recruited to mediate site-specific demethylation. To answer this question, we utilized the known fibrosis suppressor gene *Rasal1* to identify the mechanism behind the signaling and recruitment of the demethylation complex. We previously identified that promoter methylation of *Rasal1* is associated with fibroblast activation and contributes to kidney and cardiac fibrosis. In addition, we have previously shown that *Rasal1* hypermethylation can be reversed through TET3-mediated hydroxymethylation specifically (Tampe et al., 2014; Xu et al., 2015, 2018) . As such, we further studied this model gene to decipher the requirements for reversing the methylation mark and restoration of *Rasal1* expression.

7.2.1 *Gm15749* serves as a label for DNA demethylation

We have previously identified a lncRNA termed *Gm15749,* which is located at the promoter region of mouse *Rasal1*. Unpublished data from our lab revealed the protective role of *Gm15749* by blocking DNMT1, thereby inhibiting the methylation of the *Rasal1* promoter. Moreover, in an *in vitro* model of fibrosis, we show a reduced expression of *Gm15749* which was more pronounced than decreased *Rasal1* expression. We further revealed that loss of *Gm15749* is associated with the reduction of *Rasal1* expression at both RNA and protein levels due to promoter methylation (Figure 26) (Xu et al., 2017).

7.2.2 R-loop formation is a prerequisite to site-specific demethylation

Emerging research is focusing on understanding the mechanism by which the demethylation proteins are recruited to specific sites. For example, Arab et al., show that the lncRNA TARID forms an R-loop structure at the TCF21 promoter and recruits GADD45A specifically which then interacts with TET1 to initiate the demethylation process. R-loops have recently gained more attention for their roles in regulating cellular processes including DNA damage and gene regulation (Arab et al., 2019). R-loops are prominent at regions that harbor CpG islands and commonly accumulate at promoter regions in a sequence specific manner, indicating that these structures are vital players in gene regulation (García-Muse & Aguilera, 2019; Niehrs & Luke, 2020). In line with these findings, we showed that the lncRNA *Gm15749* forms an R-loop at the *Rasal1* promoter thereby initiating the recruitment of demethylation proteins. We further show that fibrotic conditions as well as loss of *Gm15749* is associated with a significant reduction of R-loop formation at the *Rasal1* promoter (Figure 27). These results are in line with previous studies, which reported the prominence of R-loop formation at transcription start sites of gene promoters (L. Chen et al., 2017; Ginno et al., 2012). Not much has been reported about the effect of TGF-β or fibrosis on R-loop formation, as such, it would be interesting to unveil the changes in regulatory R-loop formation during disease states. To further validate the formation of R-loops at the *Rasal1* promoter, we browsed the R-loop DB database for DRIP-seq R-loop profiling experiments and could also observe enrichment of R-loops at the *Rasal1* promoter in 3T3 (embryonic fibroblasts) cell line (Sanz et al., 2016) (Figure 34). Although knockdown experiments of *Gm15749* using the shRNA technology

revealed reduced R-loop formation (detected in the nucleus), we are aware that shRNA-knockdown occurs in the cytoplasm. So, to validate our findings, a knockout at the genomic level using a *Gm15749* knockout cell line will be used in the future.

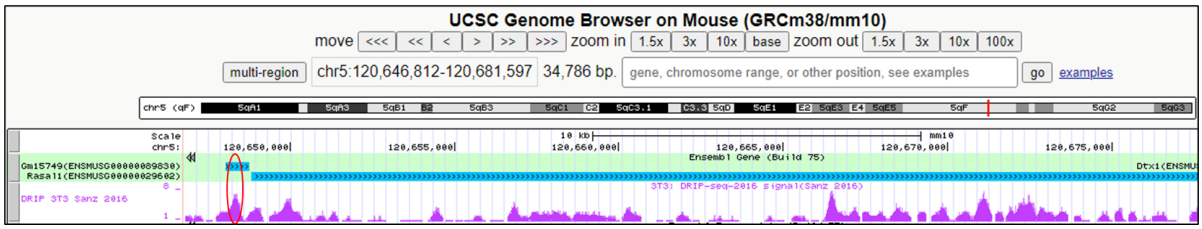

Figure 34: DRIP seq reveals enrichment of R-loops at the *Rasal1* promoter in 3T3 cell line. Screenshot from UCSC genome browser revealing DRIP-seq read density (in purple) at the *Rasal1* and *Gm15749* locus (in blue). R-loops in embryonic fibroblasts are enriched at the *Rasal1* promoter region (red circle) where the *Gm15749* amplicon is located. (Sanz et al., 2016).

7.2.3 *Gm15749* mediated demethylation requires GADD45G and TET3

Unpublished data revealed that overexpression of *Gm15749* is associated with decreased methylation of *Rasal1*. As such, we hypothesized that the R-loop forming *Gm15749* can recruit demethylation enzymes to the *Rasal1* promoter. In a genome-wide methylome and transcriptome analysis of heart tissue from aortic stenosis, we identified GADD45G as one of few genes, which is reduced and hypermethylated in patients progressing to heart failure (Figure 28) and confirmed this both *in vitro* and *in vivo* experimental fibrotic conditions (Figure 29). From literature, we found that the active demethylation protein family GADD45 have RNA binding properties and are known to interact with TDG to mediate the removal of 5fC and 5caC (Z. Li et al., 2015). Moreover. GADD45A has been reported to interact with and recruit TET1 to the TCF21 promoter (Arab et al., 2014; Kienhöfer et al., 2015).

Indeed, in analogy to these reports, we could detect binding of GADD45G at the *Rasal1* promoter in MCFs by direct interaction with the R-loop forming *Gm15479* exclusively (Figure 30). It is important to note that the contribution of GADD45G to the demethylation of fibrosis related genes has never been reported before. In the heart, GADD45G has been reported to have a negative pro-apoptotic effect on cardiomyocytes (Lucas et al., 2015). Although GADD45 proteins have been mainly associated with DNA damage processes, recent evidence supports the need to explore their active site-specific DNA demethylation function and role in the regulation of gene expression in physiological and pathological conditions.

In summary, in an attempt to understand how TET3 is specifically recruited to gene promoters, we studied the well-characterized fibrosis suppressor gene *Rasal1*. Demethylation of *Rasal1* is restricted to a few CpG nucleotides which is characteristic of site-specific demethylation. The ability of *Gm15749* to bind to *Rasal1* and act as a scaffold by forming an R-loop, which guides the demethylation proteins TET3 and GADD45G to the promoter region has led to the identification of a novel role of regulatory R-loops at distinct gene promoters (Figure 35). Given the results from this study and previously published work (Arab et al., 2014, 2019; Kienhöfer et al., 2015), a recent study further supports our hypothesis by showing that 5hmC marks and R-loops overlap at transcriptionally active genes. Specifically, the investigators show that TET enzymes favor the formation of R-loops in both mouse embryonic stem cells and fibroblasts (Sabino et al., 2022). RNA-guided DNA demethylation may not be limited to *Gm15749*-orchestrated recruitment of GADD45G and TET3 to the *Rasal1* promoter, but also to understanding global epigenetic changes occurring during fibrosis and tumorigenesis.

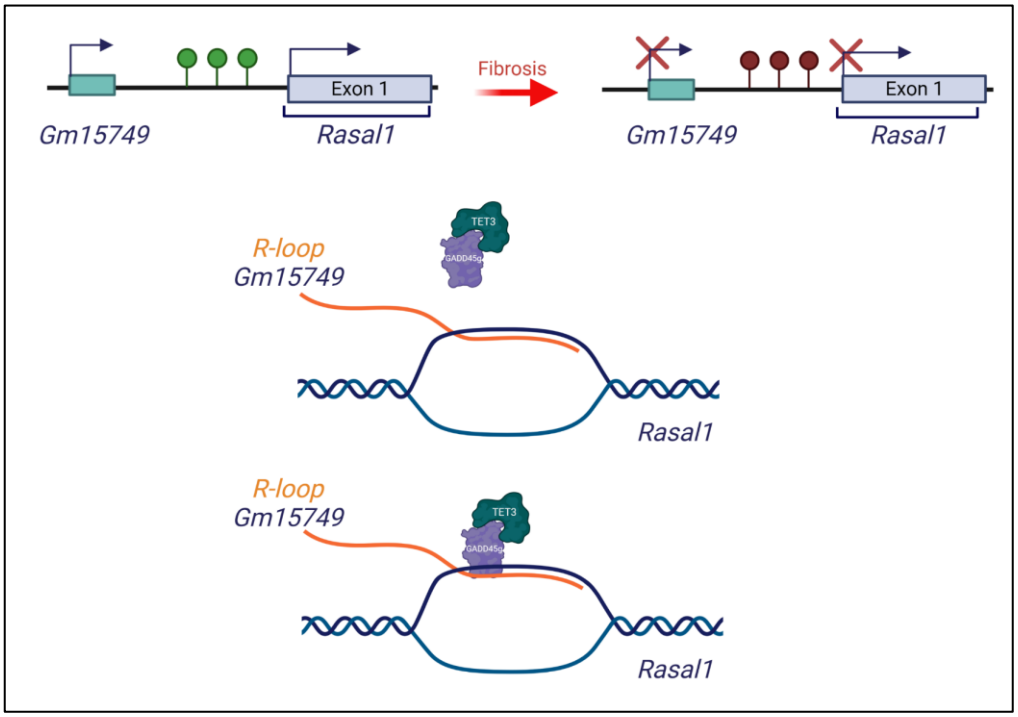

Figure 35: *Gm15749* forms an R-loop and recruits TET3 and GADD45g to the *Rasal1* promoter. Under normal conditions, *Gm15749*, which is located at the promoter *Rasal1* forms an R-loop and signals the recruitment of GADD45G and TET3 specifically to the *Rasal1* promoter to mediate site-specific demethylation. In fibrotic conditions, *Gm15749*, TET3, and GADD45G expression is reduced resulting in the inability of the demethylation complex to form leading to the loss of protection and silencing of *Rasal1*.

8 Conclusion and outlook

In this study, we have identified several different antifibrotic mechanisms mediated by TET3, adding to previous work of the lab, which showed an effect of TET3 on DNA damage repair. Because previous studies have shown that the antihypertensive drug hydralazine induces TET3 and attenuates kidney and cardiac fibrosis in mouse models *in vivo* (Tampe et al., 2015, 2017) , there is an ongoing clinical study, which tests the antifibrotic effect of low-dose hydralazine in patients with aortic stenosis undergoing TAVI. In order to assess whether upregulation of TET3 per se is more beneficial as opposed to regulating its downstream targets, further studies are necessary to decipher the best option. Since TET3 has more than 9000 direct target genes (Bian & Yu, 2014), it is important to understand if potential adverse off-target effects might decrease the antifibrotic effect of a TET3-inducing therapy. Another option is to directly utilize the downstream target such as miR-30d as an antifibrotic therapy of choice. As such, it is crucial to evaluate the beneficial effect from either option using relevant models to judge and determine the optimal therapeutic approach.

As miRNAs can be easily manipulated, they are promising therapeutic targets for a variety of diseases. Taking into consideration the previously published evidence on the cardioprotective roles of miR-30d, together with the current data presented in this thesis, miR-30d poses as a target to reverse pathological cardiac hypertrophy (J. Li et al., 2021, 2022). Nanocarrier-based-miR-30d delivery would be a feasible option to consider, as RNA-based therapeutics have recently gained more attention as the next-generation medicine by biopharmaceutical companies and researchers (Lundstrom, 2018). Ensuring the stability and efficiency of delivery of miRNAs to the heart is the main concern for the translation of such therapeutic approaches. Moreover, it is important to gain more information from the current clinical trials about the absorption, excretion, distribution, and metabolism of miRNAs to further optimize their therapeutic efficiency.

References

Abplanalp, W. T., Fischer, A., John, D., Zeiher, A. M., Gosgnach, W., Darville, H., Montgomery, R., Pestano, L., Allée, G., Paty, I., Fougerousse, F., & Dimmeler, S. (2020). Efficiency and Target Derepression of Anti-miR-92a: Results of a First in Human Study. *Nucleic Acid Therapeutics*, *30*(6). https://doi.org/10.1089/nat.2020.0871

Aisagbonhi, O., Rai, M., Ryzhov, S., Atria, N., Feoktistov, I., & Hatzopoulos, A. K. (2011). Experimental myocardial infarction triggers canonical Wnt signaling and endothelial-to-mesenchymal transition. *DMM Disease Models and Mechanisms*, *4*(4). https://doi.org/10.1242/dmm.006510

Alva, J. A., Zovein, A. C., Monvoisin, A., Murphy, T., Salazar, A., Harvey, N. L., Carmeliet, P., & Iruela-Arispe, M. L. (2006). VE-cadherin-cre-recombinase transgenic mouse: A tool for lineage analysis and gene deletion in endothelial cells. *Developmental Dynamics*, *235*(3). https://doi.org/10.1002/dvdy.20643

Ambros, V. (2004). The functions of animal microRNAs. In *Nature* (Vol. 431, Issue 7006). https://doi.org/10.1038/nature02871

Antunes, C., da Silva, J. D., Guerra-Gomes, S., Alves, N. D., Ferreira, F., Loureiro-Campos, E., Branco, M. R., Sousa, N., Reik, W., Pinto, L., & Marques, C. J. (2021). Tet3 ablation in adult brain neurons increases anxiety-like behavior and regulates cognitive function in mice. *Molecular Psychiatry*, *26*(5). https://doi.org/10.1038/s41380-020-0695-7

Arab, K., Karaulanov, E., Musheev, M., Trnka, P., Schäfer, A., Grummt, I., & Niehrs, C. (2019). GADD45A binds R-loops and recruits TET1 to CpG island promoters. In *Nature Genetics* (Vol. 51, Issue 2). https://doi.org/10.1038/s41588-018-0306-6

Arab, K., Park, Y. J., Lindroth, A. M., Schäfer, A., Oakes, C., Weichenhan, D., Lukanova, A., Lundin, E., Risch, A., Meister, M., Dienemann, H., Dyckhoff, G., Herold-Mende, C., Grummt, I., Niehrs, C., & Plass, C. (2014). Long noncoding RNA TARID directs demethylation and activation of the tumor suppressor TCF21 via GADD45A. *Molecular Cell*, *55*(4). https://doi.org/10.1016/j.molcel.2014.06.031

Aure, M. R., Leivonen, S. K., Fleischer, T., Zhu, Q., Overgaard, J., Alsner, J., Tramm, T., Louhimo, R., Alnæs, G. I. G., Perälä, M., Busato, F., Touleimat, N., Tost, J., Børresen-Dale, A. L., Hautaniemi, S., Troyanskaya, O. G., Lingjærde, O. C., Sahlberg, K. K., &

Kristensen, V. N. (2013). Individual and combined effects of DNA methylation and copy number alterations on miRNA expression in breast tumors. *Genome Biology*, *14*(11). https://doi.org/10.1186/gb-2013-14-11-r126

Azmi, A. S., Li, Y., Aboukameel, A., Muqbil, I., Philip, P. A., & Mohammad, R. M. (2019). DNA-methylation-caused downregulation of miR-30 contributes to the high expression of XPO1 and the aggressive growth of tumors in pancreatic ductal adenocarcinoma. *Cancers*, *11*(8). https://doi.org/10.3390/cancers11081101

Baccarelli, A., Rienstra, M., & Benjamin, E. J. (2010). Cardiovascular epigenetics: Basic concepts and results from animal and human studies. *Circulation: Cardiovascular Genetics*, *3*(6). https://doi.org/10.1161/CIRCGENETICS.110.958744

Bannister, A. J., & Kouzarides, T. (2011). Regulation of chromatin by histone modifications. In *Cell Research* (Vol. 21, Issue 3). https://doi.org/10.1038/cr.2011.22

Barski, A., Cuddapah, S., Cui, K., Roh, T. Y., Schones, D. E., Wang, Z., Wei, G., Chepelev, I., & Zhao, K. (2007). High-Resolution Profiling of Histone Methylations in the Human Genome. *Cell*, *129*(4). https://doi.org/10.1016/j.cell.2007.05.009

Bartel, D. P. (2004). MicroRNAs: Genomics, Biogenesis, Mechanism, and Function. In *Cell* (Vol. 116, Issue 2). https://doi.org/10.1016/S0092-8674(04)00045-5

Bassenge, E. (1996). Endothelial function in different organs. *Progress in Cardiovascular Diseases*, *39*(3). https://doi.org/10.1016/S0033-0620(96)80002-8

Bassenge, E., & Heusch, G. (1990). Endothelial and neuro-humoral control of coronary blood flow in health and disease. In *Reviews of physiology, biochemistry and pharmacology* (Vol. 116). https://doi.org/10.1007/3540528806_4

Bechtel, W., McGoohan, S., Zeisberg, E. M., Müller, G. A., Kalbacher, H., Salant, D. J., Müller, C. A., Kalluri, R., & Zeisberg, M. (2010). Methylation determines fibroblast activation and fibrogenesis in the kidney. *Nature Medicine*, *16*(5). https://doi.org/10.1038/nm.2135

Beckedorff, F. C., Ayupe, A. C., Crocci-Souza, R., Amaral, M. S., Nakaya, H. I., Soltys, D. T., Menck, C. F. M., Reis, E. M., & Verjovski-Almeida, S. (2013). The Intronic Long Noncoding RNA ANRASSF1 Recruits PRC2 to the RASSF1A Promoter, Reducing the Expression of RASSF1A and Increasing Cell Proliferation. *PLoS Genetics*, *9*(8). https://doi.org/10.1371/journal.pgen.1003705

Bernstein, B. E., Kamal, M., Lindblad-Toh, K., Bekiranov, S., Bailey, D. K., Huebert, D. J., McMahon, S., Karlsson, E. K., Kulbokas, E. J., Gingeras, T. R., Schreiber, S. L., & Lander, E. S. (2005). Genomic maps and comparative analysis of histone modifications in human and mouse. *Cell*, *120*(2). https://doi.org/10.1016/j.cell.2005.01.001

Bian, C., & Yu, X. (2014). PGC7 suppresses TET3 for protecting DNA methylation. *Nucleic Acids Research*, *42*(5). https://doi.org/10.1093/nar/gkt1261

Boque-Sastre, R., Soler, M., Oliveira-Mateos, C., Portela, A., Moutinho, C., Sayols, S., Villanueva, A., Esteller, M., & Guil, S. (2015). Head-to-head antisense transcription and R-loop formation promotes transcriptional activation. *Proceedings of the National Academy of Sciences of the United States of America*, *112*(18). https://doi.org/10.1073/pnas.1421197112

Carrier, F., Georgel, P. T., Pourquier, P., Blake, M., Kontny, H. U., Antinore, M. J., Gariboldi, M., Myers, T. G., Weinstein, J. N., Pommier, Y., & Fornace, A. J. (1999). Gadd45, a p53-Responsive Stress Protein, Modifies DNA Accessibility on Damaged Chromatin. *Molecular and Cellular Biology*, *19*(3). https://doi.org/10.1128/mcb.19.3.1673

Chen, L., Chen, J. Y., Zhang, X., Gu, Y., Xiao, R., Shao, C., Tang, P., Qian, H., Luo, D., Li, H., Zhou, Y., Zhang, D. E., & Fu, X. D. (2017). R-ChIP Using Inactive RNase H Reveals Dynamic Coupling of R-loops with Transcriptional Pausing at Gene Promoters. *Molecular Cell*, *68*(4). https://doi.org/10.1016/j.molcel.2017.10.008

Chen, P. Y., Qin, L., Baeyens, N., Li, G., Afolabi, T., Budatha, M., Tellides, G., Schwartz, M. A., & Simons, M. (2015). Endothelial-to-mesenchymal transition drives atherosclerosis progression. *Journal of Clinical Investigation*, *125*(12). https://doi.org/10.1172/JCI82719

Ciavarella, C., Motta, I., Vasuri, F., Fittipaldi, S., Valente, S., Pollutri, D., Ricci, F., Gargiulo, M., & Pasquinelli, G. (2021). Involvement of mir-30a-5p and mir-30d in endothelial to mesenchymal transition and early osteogenic commitment under inflammatory stress in huvec. *Biomolecules*, *11*(2). https://doi.org/10.3390/biom11020226

Colpaert, R. M. W., & Calore, M. (2019). MicroRNAs in cardiac diseases. In *Cells* (Vol. 8, Issue 7). https://doi.org/10.3390/cells8070737

Croft, J. B., Giles, W. H., Pollard, R. A., Keenan, N. L., Casper, M. L., & Anda, R. F. (1999). Heart failure survival among older adults in the United States: A poor prognosis for an emerging epidemic in the Medicare population. *Archives of Internal Medicine*, *159*(5). https://doi.org/10.1001/archinte.159.5.505

Crossley, M. P., Bocek, M., & Cimprich, K. A. (2019). R-Loops as Cellular Regulators and Genomic Threats. In *Molecular Cell* (Vol. 73, Issue 3). https://doi.org/10.1016/j.molcel.2019.01.024

Cui, K., & Bian, X. (2021). The microRNA cluster miR-30b/-30d prevents tumor cell switch from an epithelial to a mesenchymal-like phenotype in GBC. *Molecular Therapy - Methods and Clinical Development*, *20*. https://doi.org/10.1016/j.omtm.2020.11.019

Curradi, M., Izzo, A., Badaracco, G., & Landsberger, N. (2002). Molecular Mechanisms of Gene Silencing Mediated by DNA Methylation. *Molecular and Cellular Biology*, *22*(9). https://doi.org/10.1128/mcb.22.9.3157-3173.2002

Das, P. M., & Singal, R. (2004). DNA Methylation and Cancer. *Journal of Clinical Oncology*, *22*(22), 4632–4642. https://doi.org/10.1200/JCO.2004.07.151

Davies, P. F. (1995). Flow-mediated endothelial mechanotransduction. In *Physiological Reviews* (Vol. 75, Issue 3). https://doi.org/10.1152/physrev.1995.75.3.519

Dawlaty, M. M., Breiling, A., Le, T., Raddatz, G., Barrasa, M. I., Cheng, A. W., Gao, Q., Powell, B. E., Li, Z., Xu, M., Faull, K. F., Lyko, F., & Jaenisch, R. (2013). Combined Deficiency of Tet1 and Tet2 Causes Epigenetic Abnormalities but Is Compatible with Postnatal Development. *Developmental Cell*, *24*(3). https://doi.org/10.1016/j.devcel.2012.12.015

Dawlaty, M. M., Ganz, K., Powell, B. E., Hu, Y. C., Markoulaki, S., Cheng, A. W., Gao, Q., Kim, J., Choi, S. W., Page, D. C., & Jaenisch, R. (2011). Tet1 is dispensable for maintaining pluripotency and its loss is compatible with embryonic and postnatal development. *Cell Stem Cell*, *9*(2). https://doi.org/10.1016/j.stem.2011.07.010

Dees, C., Chakraborty, D., & Distler, J. H. W. (2021). Cellular and molecular mechanisms in fibrosis. *Experimental Dermatology*, *30*(1). https://doi.org/10.1111/exd.14193

Dickerson, S. K., Market, E., Besmer, E., & Papavasiliou, F. N. (2003). AID mediates hypermutation by deaminating single stranded DNA. *Journal of Experimental Medicine*, *197*(10). https://doi.org/10.1084/jem.20030481

Egger, G., Liang, G., Aparicio, A., & Jones, P. A. (2004). Epigenetics in human disease and prospects for epigenetic therapy. In *Nature* (Vol. 429, Issue 6990). https://doi.org/10.1038/nature02625

Ernst, J., Kheradpour, P., Mikkelsen, T. S., Shoresh, N., Ward, L. D., Epstein, C. B., Zhang, X., Wang, L., Issner, R., Coyne, M., Ku, M., Durham, T., Kellis, M., & Bernstein, B. E. (2011). Mapping and analysis of chromatin state dynamics in nine human cell types. *Nature*, *473*(7345). https://doi.org/10.1038/nature09906

Fan, D., Takawale, A., Lee, J., & Kassiri, Z. (2012). Cardiac fibroblasts, fibrosis and extracellular matrix remodeling in heart disease. In *Fibrogenesis and Tissue Repair* (Vol. 5, Issue 1). https://doi.org/10.1186/1755-1536-5-15

Fang, S., Li, J., Xiao, Y., Lee, M., Guo, L., Han, W., Li, T., Hill, M. C., Hong, T., Mo, W., Xu, R., Zhang, P., Wang, F., Chang, J., Zhou, Y., Sun, D., Martin, J. F., & Huang, Y. (2019). Tet inactivation disrupts YY1 binding and long-range chromatin interactions during embryonic heart development. *Nature Communications*, *10*(1). https://doi.org/10.1038/s41467-019-12325-z

Friso, S., Pizzolo, F., Choi, S. W., Guarini, P., Castagna, A., Ravagnani, V., Carletto, A., Pattini, P., Corrocher, R., & Olivieri, O. (2008). Epigenetic control of 11 beta-hydroxysteroid dehydrogenase 2 gene promoter is related to human hypertension. *Atherosclerosis*, *199*(2). https://doi.org/10.1016/j.atherosclerosis.2007.11.029

Gabel, S. A., Walker, V. R., London, R. E., Steenbergen, C., Korach, K. S., & Murphy, E. (2005). Estrogen receptor beta mediates gender differences in ischemia/reperfusion injury. *Journal of Molecular and Cellular Cardiology*, *38*(2). https://doi.org/10.1016/j.yjmcc.2004.11.013

Gan, W., Guan, Z., Liu, J., Gui, T., Shen, K., Manley, J. L., & Li, X. (2011). R-loop-mediated genomic instability is caused by impairment of replication fork progression. *Genes and Development*, *25*(19). https://doi.org/10.1101/gad.17010011

Garcia-Menendez, L., Karamanlidis, G., Kolwicz, S., & Tian, R. (2013). Substrain specific response to cardiac pressure overload in C57BL/6 mice. *American Journal of Physiology - Heart and Circulatory Physiology*, *305*(3). https://doi.org/10.1152/ajpheart.00088.2013

García-Muse, T., & Aguilera, A. (2019). R Loops: From Physiological to Pathological Roles. In *Cell* (Vol. 179, Issue 3). https://doi.org/10.1016/j.cell.2019.08.055

Gheorghe, A., Griffiths, U., Murphy, A., Legido-Quigley, H., Lamptey, P., & Perel, P. (2018). The economic burden of cardiovascular disease and hypertension in low- and middle-income countries: A systematic review. In *BMC Public Health* (Vol. 18, Issue 1). https://doi.org/10.1186/s12889-018-5806-x

Gibbons, H. R., Shaginurova, G., Kim, L. C., Chapman, N., Spurlock, C. F., & Aune, T. M. (2018). Divergent lncRNA GATA3-AS1 Regulates GATA3 Transcription in T-Helper 2 Cells. *Frontiers in Immunology*, *9*. https://doi.org/10.3389/fimmu.2018.02512

GIMBRONE, M. A. (1987). Vascular Endothelium: Nature's Blood-Compatible Container. *Annals of the New York Academy of Sciences*, *516*(1). https://doi.org/10.1111/j.1749-6632.1987.tb33025.x

Ginno, P. A., Lott, P. L., Christensen, H. C., Korf, I., & Chédin, F. (2012). R-Loop Formation Is a Distinctive Characteristic of Unmethylated Human CpG Island Promoters. *Molecular Cell*, *45*(6). https://doi.org/10.1016/j.molcel.2012.01.017

Gogiraju, R., Bochenek, M. L., & Schäfer, K. (2019). Angiogenic Endothelial Cell Signaling in Cardiac Hypertrophy and Heart Failure. In *Frontiers in Cardiovascular Medicine* (Vol. 6). https://doi.org/10.3389/fcvm.2019.00020

Gong, F., Guo, Y., Niu, Y., Jin, J., Zhang, X., Shi, X., Zhang, L., Li, R., Chen, L., & Ma, R. Z. (2017). Epigenetic silencing of TET2 and TET3 induces an EMT-like process in melanoma. *Oncotarget*, *8*(1). https://doi.org/10.18632/oncotarget.13324

Goumans, M. J., Liu, Z., & ten Dijke, P. (2009). TGF-β signaling in vascular biology and dysfunction. In *Cell Research* (Vol. 19, Issue 1). https://doi.org/10.1038/cr.2008.326

Greco, C. M., Kunderfranco, P., Rubino, M., Larcher, V., Carullo, P., Anselmo, A., Kurz, K., Carell, T., Angius, A., Latronico, M. V. G., Papait, R., & Condorelli, G. (2016). DNA hydroxymethylation controls cardiomyocyte gene expression in development and hypertrophy. *Nature Communications*, *7*. https://doi.org/10.1038/ncomms12418

Gu, T. P., Guo, F., Yang, H., Wu, H. P., Xu, G. F., Liu, W., Xie, Z. G., Shi, L., He, X., Jin, S. G., Iqbal, K., Shi, Y. G., Deng, Z., Szabó, P. E., Pfeifer, G. P., Li, J., & Xu, G. L. (2011). The role of Tet3 DNA dioxygenase in epigenetic reprogramming by oocytes. *Nature*, *477*(7366). https://doi.org/10.1038/nature10443

Guo, J. U., Su, Y., Zhong, C., Ming, G. L., & Song, H. (2011). Hydroxylation of 5-methylcytosine by TET1 promotes active DNA demethylation in the adult brain. *Cell*, *145*(3). https://doi.org/10.1016/j.cell.2011.03.022

Gustafsson, E., Brakebusch, C., Hietanen, K., & Fässler, R. (2001). Tie-1-directed expression of Cre recombinase in endothelial cells of embryoid bodies and transgenic mice. *Journal of Cell Science*, *114*(4). https://doi.org/10.1242/jcs.114.4.671

Hall, C., Gehmlich, K., Denning, C., & Pavlovic, D. (2021). Complex relationship between cardiac fibroblasts and cardiomyocytes in health and disease. *Journal of the American Heart Association*, *10*(5). https://doi.org/10.1161/JAHA.120.019338

Han, P., Hang, C. T., Yang, J., & Chang, C. P. (2011). Chromatin remodeling in cardiovascular development and physiology. In *Circulation Research* (Vol. 108, Issue 3). https://doi.org/10.1161/CIRCRESAHA.110.224287

Hashimoto, N., Phan, S. H., Imaizumi, K., Matsuo, M., Nakashima, H., Kawabe, T., Shimokata, K., & Hasegawa, Y. (2010). Endothelial-mesenchymal transition in bleomycin-induced pulmonary fibrosis. *American Journal of Respiratory Cell and Molecular Biology*, *43*(2). https://doi.org/10.1165/rcmb.2009-0031OC

Hinderer, S., & Schenke-Layland, K. (2019). Cardiac fibrosis – A short review of causes and therapeutic strategies. In *Advanced Drug Delivery Reviews* (Vol. 146). https://doi.org/10.1016/j.addr.2019.05.011

Hinkel, R., Penzkofer, D., Zühlke, S., Fischer, A., Husada, W., Xu, Q. F., Baloch, E., van Rooij, E., Zeiher, A. M., Kupatt, C., & Dimmeler, S. (2013). Inhibition of microRNA-92a protects against ischemia/reperfusion injury in a large-animal model. *Circulation*, *128*(10). https://doi.org/10.1161/CIRCULATIONAHA.113.001904

Holley, A. S., Holley, A. S., Danielson, K. M., Harding, S. A., & Larsen, P. D. (2021). Value of miR-30d and miR-146a as Prognostic Biomarkers for Heart Failure Development Post Myocardial Infarction. *Journal of Integrative Cardiology Open Access*. https://doi.org/10.31487/j.jicoa.2021.01.01

Holmes, J. W., Borg, T. K., & Covell, J. W. (2005). Structure and mechanics of healing myocardial infarcts. In *Annual Review of Biomedical Engineering* (Vol. 7). https://doi.org/10.1146/annurev.bioeng.7.060804.100453

Hsieh, P. C. H., Davis, M. E., Lisowski, L. K., & Lee, R. T. (2006). Endothelial-cardiomyocyte interactions in cardiac development and repair. In *Annual Review of Physiology* (Vol. 68). https://doi.org/10.1146/annurev.physiol.68.040104.124629

Hu, L., Lu, J., Cheng, J., Rao, Q., Li, Z., Hou, H., Lou, Z., Zhang, L., Li, W., Gong, W., Liu, M., Sun, C., Yin, X., Li, J., Tan, X., Wang, P., Wang, Y., Fang, D., Cui, Q., … Xu, Y. (2015). Structural insight into substrate preference for TET-mediated oxidation. *Nature*, *527*(7576). https://doi.org/10.1038/nature15713

Hu, Z., Zhang, A., Storz, G., Gottesman, S., & Leppla, S. H. (2006). An antibody-based microarray assay for small RNA detection. *Nucleic Acids Research*, *34*(7). https://doi.org/10.1093/nar/gkl142

Hulshoff, M. S., Xu, X., Krenning, G., & Zeisberg, E. M. (2018). Epigenetic Regulation of Endothelial-to-Mesenchymal Transition in Chronic Heart Disease. *Arteriosclerosis, Thrombosis, and Vascular Biology*, *38*(9). https://doi.org/10.1161/atvbaha.118.311276

Huntzinger, E., & Izaurralde, E. (2011). Gene silencing by microRNAs: Contributions of translational repression and mRNA decay. In *Nature Reviews Genetics* (Vol. 12, Issue 2). https://doi.org/10.1038/nrg2936

Jin, S. G., Zhang, Z. M., Dunwell, T. L., Harter, M. R., Wu, X., Johnson, J., Li, Z., Liu, J., Szabó, P. E., Lu, Q., Xu, G. liang, Song, J., & Pfeifer, G. P. (2016). Tet3 Reads 5-Carboxylcytosine through Its CXXC Domain and Is a Potential Guardian against Neurodegeneration. *Cell Reports*, *14*(3). https://doi.org/10.1016/j.celrep.2015.12.044

Jr, E. L. Powers., & Waddington, C. H. (1943). Organisers and Genes. *American Midland Naturalist*, *30*(3). https://doi.org/10.2307/2421224

Junqueira, L. C. U., Bignolas, G., & Brentani, R. R. (1979). Picrosirius staining plus polarization microscopy, a specific method for collagen detection in tissue sections. *The Histochemical Journal*, *11*(4). https://doi.org/10.1007/BF01002772

Kang, J., Lienhard, M., Pastor, W. A., Chawla, A., Novotny, M., Tsagaratou, A., Lasken, R. S., Thompson, E. C., Azim Surani, M., Koralov, S. B., Kalantry, S., Chavez, L., & Rao, A. (2015). Simultaneous deletion of the methylcytosine oxidases Tet1 and Tet3 increases transcriptome variability in early embryogenesis. *Proceedings of the National Academy of Sciences of the United States of America*, *112*(31). https://doi.org/10.1073/pnas.1510510112

Khyzha, N., Alizada, A., Wilson, M. D., & Fish, J. E. (2017). Epigenetics of Atherosclerosis: Emerging Mechanisms and Methods. In *Trends in Molecular Medicine* (Vol. 23, Issue 4). https://doi.org/10.1016/j.molmed.2017.02.004

Kienhöfer, S., Musheev, M. U., Stapf, U., Helm, M., Schomacher, L., Niehrs, C., & Schäfer, A. (2015). GADD45a physically and functionally interacts with TET1. *Differentiation*, *90*(1–3). https://doi.org/10.1016/j.diff.2015.10.003

Kisanuki, Y. Y., Hammer, R. E., Miyazaki, J. ichi, Williams, S. C., Richardson, J. A., & Yanagisawa, M. (2001). Tie2-Cre transgenic mice: A new model for endothelial cell-lineage analysis in vivo. *Developmental Biology*, *230*(2). https://doi.org/10.1006/dbio.2000.0106

Klug, M., & Rehli, M. (2006). Functional analysis of promoter CpG methylation using a CpG-free luciferase reporter vector. *Epigenetics*, *1*(3). https://doi.org/10.4161/epi.1.3.3327

Kornberg, R. D. (1974). Chromatin structure: A repeating unit of histones and DNA. *Science*, *184*(4139). https://doi.org/10.1126/science.184.4139.868

Kriaucionis, S., & Heintz, N. (2009). The nuclear DNA base 5-hydroxymethylcytosine is present in purkinje neurons and the brain. *Science*, *324*(5929). https://doi.org/10.1126/science.1169786

Krüger-Genge, A., Blocki, A., Franke, R. P., & Jung, F. (2019). Vascular endothelial cell biology: An update. In *International Journal of Molecular Sciences* (Vol. 20, Issue 18). https://doi.org/10.3390/ijms20184411

Kumar Rath, S. (2020). *TET3 IMPACTS CARDIAC FIBROSIS PARTIALLY VIA REGULATION OF DNA DAMAGE RESPONSE* [Georg-August-University Göttingen]. https://doi.org/10.53846/goediss-7851

Lagendijk, A. K., Szabó, A., Merks, R. M. H., & Bakkers, J. (2013). Hyaluronan: A critical regulator of endothelial-to-mesenchymal transition during cardiac valve formation. In *Trends in Cardiovascular Medicine* (Vol. 23, Issue 5). https://doi.org/10.1016/j.tcm.2012.10.002

Lemonnier, F., Couronné, L., Parrens, M., Jaïs, J. P., Travert, M., Lamant, L., Tournillac, O., Rousset, T., Fabiani, B., Cairns, R. A., Mak, T., Bastard, C., Bernard, O. A., de Leval, L., & Gaulard, P. (2012). Recurrent TET2 mutations in peripheral T-cell lymphomas

correlate with TFH-like features and adverse clinical parameters. *Blood*, *120*(7). https://doi.org/10.1182/blood-2012-02-408542

Li, J., Salvador, A. M., Li, G., Valkov, N., Ziegler, O., Yeri, A., Yang Xiao, C., Meechoovet, B., Alsop, E., Rodosthenous, R. S., Kundu, P., Huan, T., Levy, D., Tigges, J., Pico, A. R., Ghiran, I., Silverman, M. G., Meng, X., Kitchen, R., … Das, S. (2021). Mir-30d Regulates Cardiac Remodeling by Intracellular and Paracrine Signaling. *Circulation Research*, *128*(1). https://doi.org/10.1161/CIRCRESAHA.120.317244

Li, J., Sha, Z., Zhu, X., Xu, W., Yuan, W., Yang, T., Jin, B., Yan, Y., Chen, R., Wang, S., Yao, J., Xu, J., Wang, Z., Li, G., Das, S., Yang, L., & Xiao, J. (2022). Targeting miR-30d reverses pathological cardiac hypertrophy. *EBioMedicine*, *81*, 104108. https://doi.org/10.1016/j.ebiom.2022.104108

Li, X., Marshall, P. R., Leighton, L. J., Zajaczkowski, E. L., Wang, Z., Madugalle, S. U., Yin, J., Bredy, T. W., & Wei, W. (2019). The DNA repair-associated protein gadd45γ regulates the temporal coding of immediate early gene expression within the prelimbic prefrontal cortex and is required for the consolidation of associative fear memory. *Journal of Neuroscience*, *39*(6). https://doi.org/10.1523/JNEUROSCI.2024-18.2018

Li, Z., Gu, T. P., Weber, A. R., Shen, J. Z., Li, B. Z., Xie, Z. G., Yin, R., Guo, F., Liu, X., Tang, F., Wang, H., Schär, P., & Xu, G. L. (2015). Gadd45a promotes DNA demethylation through TDG. *Nucleic Acids Research*, *43*(8). https://doi.org/10.1093/nar/gkv283

Litviňuková, M., Talavera-López, C., Maatz, H., Reichart, D., Worth, C. L., Lindberg, E. L., Kanda, M., Polanski, K., Heinig, M., Lee, M., Nadelmann, E. R., Roberts, K., Tuck, L., Fasouli, E. S., DeLaughter, D. M., McDonough, B., Wakimoto, H., Gorham, J. M., Samari, S., … Teichmann, S. A. (2020). Cells of the adult human heart. *Nature*, *588*(7838). https://doi.org/10.1038/s41586-020-2797-4

Lloyd-Jones, D., Adams, R., Carnethon, M., de Simone, G., Ferguson, T. B., Flegal, K., Ford, E., Furie, K., Go, A., Greenlund, K., Haase, N., Hailpern, S., Ho, M., Howard, V., Kissela, B., Kittner, S., Lackland, D., Lisabeth, L., Marelli, A., … Hong, Y. (2009). Heart disease and stroke statistics - 2009 update. A report from the American heart association statistics committee and stroke statistics subcommittee. In *Circulation* (Vol. 119, Issue 3). https://doi.org/10.1161/CIRCULATIONAHA.108.191259

Lucas, A., Mialet-Perez, J., Daviaud, D., Parini, A., Marber, M. S., & Sicard, P. (2015). Gadd45γ regulates cardiomyocyte death and post-myocardial infarction left ventricular remodelling. *Cardiovascular Research*, *108*(2). https://doi.org/10.1093/cvr/cvv219

Lundstrom, K. (2018). Latest development on RNA-based drugs and vaccines. In *Future Science OA* (Vol. 4, Issue 5). https://doi.org/10.4155/fsoa-2017-0151

Ma, D. K., Jang, M. H., Guo, J. U., Kitabatake, Y., Chang, M. L., Pow-anpongkul, N., Flavell, R. A., Lu, B., Ming, G. L., & Song, H. (2009). Neuronal activity-induced Gadd45b promotes epigenetic DNA demethylation and adult neurogenesis. *Science*, *323*(5917). https://doi.org/10.1126/science.1166859

Markwald, R. R., Fitzharris, T. P., & Smith, W. N. A. (1975). Structural analysis of endocardial cytodifferentiation. *Developmental Biology*, *42*(1). https://doi.org/10.1016/0012-1606(75)90321-8

Marti, C. N., Gheorghiade, M., Kalogeropoulos, A. P., Georgiopoulou, V. v., Quyyumi, A. A., & Butler, J. (2012). Endothelial dysfunction, arterial stiffness, and heart failure. In *Journal of the American College of Cardiology* (Vol. 60, Issue 16). https://doi.org/10.1016/j.jacc.2011.11.082

Mattick, J. S. (2004). RNA regulation: A new genetics? In *Nature Reviews Genetics* (Vol. 5, Issue 4). https://doi.org/10.1038/nrg1321

McGhee, J. D., & Felsenfeld, G. (1980). Nucleosome structure. In *Annual review of biochemistry* (Vol. 49). https://doi.org/10.1146/annurev.bi.49.070180.005343

Mekada, K., & Yoshiki, A. (2021). Substrains matter in phenotyping of c57bl/6 mice. In *Experimental Animals* (Vol. 70, Issue 2). https://doi.org/10.1538/expanim.20-0158

Melman, Y. F., Shah, R., Danielson, K., Xiao, J., Simonson, B., Barth, A., Chakir, K., Lewis, G. D., Lavender, Z., Truong, Q. A., Kleber, A., Das, R., Rosenzweig, A., Wang, Y., Kass, D. A., Singh, J. P., & Das, S. (2015). Circulating microRNA-30d is associated with response to cardiac resynchronization therapy in heart failure and regulates cardiomyocyte apoptosis: A translational pilot study. In *Circulation* (Vol. 131, Issue 25). https://doi.org/10.1161/CIRCULATIONAHA.114.013220

Moran-Crusio, K., Reavie, L., Shih, A., Abdel-Wahab, O., Ndiaye-Lobry, D., Lobry, C., Figueroa, M. E., Vasanthakumar, A., Patel, J., Zhao, X., Perna, F., Pandey, S., Madzo, J., Song, C., Dai, Q., He, C., Ibrahim, S., Beran, M., Zavadil, J., … Levine, R. L. (2011). Tet2

Loss Leads to Increased Hematopoietic Stem Cell Self-Renewal and Myeloid Transformation. *Cancer Cell*, *20*(1). https://doi.org/10.1016/j.ccr.2011.06.001

Motoike, T., Markham, D. W., Rossant, J., & Sato, T. N. (2003). Evidence for novel fate of Flk1+ progenitor: Contribution to muscle lineage. *Genesis*, *35*(3). https://doi.org/10.1002/gene.10175

Niehrs, C., & Luke, B. (2020). Regulatory R-loops as facilitators of gene expression and genome stability. In *Nature Reviews Molecular Cell Biology* (Vol. 21, Issue 3). https://doi.org/10.1038/s41580-019-0206-3

Niehrs, C., & Schäfer, A. (2012). Active DNA demethylation by Gadd45 and DNA repair. In *Trends in Cell Biology* (Vol. 22, Issue 4). https://doi.org/10.1016/j.tcb.2012.01.002

Odejide, O., Weigert, O., Lane, A. A., Toscano, D., Lunning, M. A., Kopp, N., Kim, S., van Bodegom, D., Bolla, S., Schatz, J. H., Teruya-Feldstein, J., Hochberg, E., Louissaint, A., Dorfman, D., Stevenson, K., Rodig, S. J., Piccaluga, P. P., Jacobsen, E., Pileri, S. A., … Weinstock, D. M. (2014). A targeted mutational landscape of angioimmunoblastic T-cell lymphoma. *Blood*, *123*(9). https://doi.org/10.1182/blood-2013-10-531509

Papait, R., Greco, C., Kunderfranco, P., Latronico, M. V. G., & Condorelli, G. (2013). Epigenetics: A new mechanism of regulation of heart failure? In *Basic Research in Cardiology* (Vol. 108, Issue 4). https://doi.org/10.1007/s00395-013-0361-1

Pardali, E., Sanchez-Duffhues, G., Gomez-Puerto, M. C., & ten Dijke, P. (2017). TGF-β-induced endothelial-mesenchymal transition in fibrotic diseases. In *International Journal of Molecular Sciences* (Vol. 18, Issue 10). https://doi.org/10.3390/ijms18102157

Pastor, W. A., Aravind, L., & Rao, A. (2013). TETonic shift: Biological roles of TET proteins in DNA demethylation and transcription. In *Nature Reviews Molecular Cell Biology* (Vol. 14, Issue 6). https://doi.org/10.1038/nrm3589

Pinto, A. R., Ilinykh, A., Ivey, M. J., Kuwabara, J. T., D'antoni, M. L., Debuque, R., Chandran, A., Wang, L., Arora, K., Rosenthal, N. A., & Tallquist, M. D. (2016). Revisiting cardiac cellular composition. *Circulation Research*, *118*(3). https://doi.org/10.1161/CIRCRESAHA.115.307778

Piya, S., Lopes-Caitar, V. S., Kim, W., Pantalone, V., Krishnan, H. B., & Hewezi, T. (2021). Title: Hypermethylation of miRNA Genes During Nodule Development. *Frontiers in Molecular Biosciences*, *8*. https://doi.org/10.3389/fmolb.2021.616623

Puls, M., Beuthner, B. E., Topci, R., Vogelgesang, A., Bleckmann, A., Sitte, M., Lange, T., Backhaus, S. J., Schuster, A., Seidler, T., Kutschka, I., Toischer, K., Zeisberg, E. M., Jacobshagen, C., & Hasenfuß, G. (2020). Impact of myocardial fibrosis on left ventricular remodelling, recovery, and outcome after transcatheter aortic valve implantation in different haemodynamic subtypes of severe aortic stenosis. *European Heart Journal*, *41*(20). https://doi.org/10.1093/eurheartj/ehaa033

Quivoron, C., Couronné, L., della Valle, V., Lopez, C. K., Plo, I., Wagner-Ballon, O., do Cruzeiro, M., Delhommeau, F., Arnulf, B., Stern, M. H., Godley, L., Opolon, P., Tilly, H., Solary, E., Duffourd, Y., Dessen, P., Merle-Beral, H., Nguyen-Khac, F., Fontenay, M., … Bernard, O. A. (2011). TET2 Inactivation Results in Pleiotropic Hematopoietic Abnormalities in Mouse and Is a Recurrent Event during Human Lymphomagenesis. *Cancer Cell*, *20*(1). https://doi.org/10.1016/j.ccr.2011.06.003

Rana, T. M. (2007). Illuminating the silence: Understanding the structure and function of small RNAs. In *Nature Reviews Molecular Cell Biology* (Vol. 8, Issue 1). https://doi.org/10.1038/nrm2085

Rau, C. D., & Vondriska, T. M. (2017). DNA Methylation and Human Heart Failure: Mechanisms or Prognostics. In *Circulation* (Vol. 136, Issue 16). https://doi.org/10.1161/CIRCULATIONAHA.117.029840

Ravichandran, M., Rafalski, D., Davies, C. I., Ortega-Recalde, O., Nan, X., Glanfield, C. R., Kotter, A., Misztal, K., Wang, A. H., Wojciechowski, M., Rażew, M., Mayyas, I. M., Kardailsky, O., Schwartz, U., Zembrzycki, K., Morison, I. M., Helm, M., Weichenhan, D., Jurkowska, R. Z., … Jurkowski, T. P. (2022). Pronounced sequence specificity of the TET enzyme catalytic domain guides its cellular function. *Science Advances*, *8*(36). https://doi.org/10.1126/sciadv.abm2427

Ribeiro de Almeida, C., Dhir, S., Dhir, A., Moghaddam, A. E., Sattentau, Q., Meinhart, A., & Proudfoot, N. J. (2018). RNA Helicase DDX1 Converts RNA G-Quadruplex Structures into R-Loops to Promote IgH Class Switch Recombination. *Molecular Cell*, *70*(4). https://doi.org/10.1016/j.molcel.2018.04.001

Sabino, J. C., de Almeida, M. R., Abreu, P. L., Ferreira, A. M., Caldas, P., Domingues, M. M., Santos, N. C., Azzalin, C. M., Grosso, A. R., & de Almeida, S. F. (2022). Epigenetic reprogramming by TET enzymes impacts co-transcriptional R-loops. *ELife*, *11*. https://doi.org/10.7554/ELIFE.69476

Saleh, A. D., Cheng, H., Martin, S. E., Si, H., Ormanoglu, P., Carlson, S., Clavijo, P. E., Yang, X., Das, R., Cornelius, S., Couper, J., Chepeha, D., Danilova, L., Harris, T. M., Prystowsky, M. B., Childs, G. J., Smith, R. v., Gordon Robertson, A., Jones, S. J. M., … van Waes, C. (2019). Integrated genomic and functional microRNA analysis identifies miR-30-5p as a tumor suppressor and potential therapeutic nanomedicine in head and neck cancer. *Clinical Cancer Research*, *25*(9). https://doi.org/10.1158/1078-0432.CCR-18-0716

Sandoo, A., Veldhuijzen van Zanten, J. J. C. S., Metsios, G. S., Carroll, D., & Kitas, G. D. (2015). The Endothelium and Its Role in Regulating Vascular Tone. *The Open Cardiovascular Medicine Journal*, *4*(1). https://doi.org/10.2174/1874192401004010302

Sanz, L. A., Hartono, S. R., Lim, Y. W., Steyaert, S., Rajpurkar, A., Ginno, P. A., Xu, X., & Chédin, F. (2016). Prevalent, Dynamic, and Conserved R-Loop Structures Associate with Specific Epigenomic Signatures in Mammals. *Molecular Cell*, *63*(1). https://doi.org/10.1016/j.molcel.2016.05.032

Schüle, K. M., Leichsenring, M., Andreani, T., Vastolo, V., Mallick, M., Musheev, M. U., Karaulanov, E., & Niehrs, C. (2019). GADD45 promotes locus-specific DNA demethylation and 2C cycling in embryonic stem cells. *Genes and Development*, *33*(13–14). https://doi.org/10.1101/gad.325696.119

Schulz, W. A., Steinhoff, C., & Florl, A. R. (2006). Methylation of endogenous human retroelements in health and disease. In *Current Topics in Microbiology and Immunology* (Vol. 310). https://doi.org/10.1007/3-540-31181-5_11

Sengupta, R., Mendenhall, A., Sarkar, N., Mukherjee, C., Afshari, A., Huang, J., & Lu, B. (2017). Viral Cre-LoxP tools aid genome engineering in mammalian cells. *Journal of Biological Engineering*, *11*(1). https://doi.org/10.1186/s13036-017-0087-y

Shikama, N., Lutz, W., Kretzschmar, R., Sauter, N., Roth, J. F., Marino, S., Wittwer, J., Scheidweiler, A., & Eckner, R. (2003). Essential function of p300 acetyltransferase

activity in heart, lung and small intestine formation. *EMBO Journal*, *22*(19). https://doi.org/10.1093/emboj/cdg502

Silva, A. C., Pereira, C., Fonseca, A. C. R. G., Pinto-do-Ó, P., & Nascimento, D. S. (2021). Bearing My Heart: The Role of Extracellular Matrix on Cardiac Development, Homeostasis, and Injury Response. In *Frontiers in Cell and Developmental Biology* (Vol. 8). https://doi.org/10.3389/fcell.2020.621644

Sohail, A., Klapacz, J., Samaranayake, M., Ullah, A., & Bhagwat, A. S. (2003). Human activation-induced cytidine deaminase causes transcription-dependent, strand-biased C to U deaminations. *Nucleic Acids Research*, *31*(12). https://doi.org/10.1093/nar/gkg464

Souders, C. A., Bowers, S. L. K., & Baudino, T. A. (2009). Cardiac fibroblast: The renaissance cell. In *Circulation Research* (Vol. 105, Issue 12). https://doi.org/10.1161/CIRCRESAHA.109.209809

Struhl, K. (2007). Transcriptional noise and the fidelity of initiation by RNA polymerase II. In *Nature Structural and Molecular Biology* (Vol. 14, Issue 2). https://doi.org/10.1038/nsmb0207-103

Sun, H., Yang, X., Zhu, J., Lv, T., Chen, Y., Chen, G., Zhong, L., Li, Y., Huang, X., Huang, G., & Tian, J. (2010). Inhibition of p300-HAT results in a reduced histone acetylation and down-regulation of gene expression in cardiac myocytes. *Life Sciences*, *87*(23–26). https://doi.org/10.1016/j.lfs.2010.10.009

Sytnikova, Y. A., Kubarenko, A. v., Schäfer, A., Weber, A. N. R., & Niehrs, C. (2011). Gadd45a is an RNA binding protein and is localized in nuclear speckles. *PLoS ONE*, *6*(1). https://doi.org/10.1371/journal.pone.0014500

Tahiliani, M., Koh, K. P., Shen, Y., Pastor, W. A., Bandukwala, H., Brudno, Y., Agarwal, S., Iyer, L. M., Liu, D. R., Aravind, L., & Rao, A. (2009). Conversion of 5-methylcytosine to 5-hydroxymethylcytosine in mammalian DNA by MLL partner TET1. *Science*, *324*(5929). https://doi.org/10.1126/science.1170116

Takaya, T., Kawamura, T., Morimoto, T., Ono, K., Kita, T., Shimatsu, A., & Hasegawa, K. (2008). Identification of p300-targeted acetylated residues in GATA4 during hypertrophic responses in cardiac myocytes. *Journal of Biological Chemistry*, *283*(15). https://doi.org/10.1074/jbc.M707391200

Tampe, B., Steinle, U., Tampe, D., Carstens, J. L., Korsten, P., Zeisberg, E. M., Müller, G. A., Kalluri, R., & Zeisberg, M. (2017). Low-dose hydralazine prevents fibrosis in a murine model of acute kidney injury–to–chronic kidney disease progression. *Kidney International*, *91*(1). https://doi.org/10.1016/j.kint.2016.07.042

Tampe, B., Tampe, D., Müller, C. A., Sugimoto, H., LeBleu, V., Xu, X., Müller, G. A., Zeisberg, E. M., Kalluri, R., & Zeisberg, M. (2014). Tet3-mediated hydroxymethylation of epigenetically silenced genes contributes to bone morphogenic protein 7-induced reversal of kidney fibrosis. *Journal of the American Society of Nephrology*, *25*(5). https://doi.org/10.1681/ASN.2013070723

Tampe, B., Tampe, D., Zeisberg, E. M., Müller, G. A., Bechtel-Walz, W., Koziolek, M., Kalluri, R., & Zeisberg, M. (2015). Induction of Tet3-dependent Epigenetic Remodeling by Low-dose Hydralazine Attenuates Progression of Chronic Kidney Disease. *EBioMedicine*, *2*(1). https://doi.org/10.1016/j.ebiom.2014.11.005

Tan, L., & Shi, Y. G. (2012). Tet family proteins and 5-hydroxymethylcytosine in development and disease. *Development*, *139*(11). https://doi.org/10.1242/dev.070771

Thomas, M., White, R. L., & Davis, R. W. (1976). Hybridization of RNA to double stranded DNA: Formation of R loops. *Proceedings of the National Academy of Sciences of the United States of America*, *73*(7). https://doi.org/10.1073/pnas.73.7.2294

Thul, P. J., Akesson, L., Wiking, M., Mahdessian, D., Geladaki, A., Ait Blal, H., Alm, T., Asplund, A., Björk, L., Breckels, L. M., Bäckström, A., Danielsson, F., Fagerberg, L., Fall, J., Gatto, L., Gnann, C., Hober, S., Hjelmare, M., Johansson, F., … Lundberg, E. (2017). A subcellular map of the human proteome. *Science*, *356*(6340). https://doi.org/10.1126/science.aal3321

Tombor, L. S., John, D., Glaser, S. F., Luxán, G., Forte, E., Furtado, M., Rosenthal, N., Baumgarten, N., Schulz, M. H., Wittig, J., Rogg, E. M., Manavski, Y., Fischer, A., Muhly-Reinholz, M., Klee, K., Looso, M., Selignow, C., Acker, T., Bibli, S. I., … Dimmeler, S. (2021). Single cell sequencing reveals endothelial plasticity with transient mesenchymal activation after myocardial infarction. *Nature Communications*, *12*(1). https://doi.org/10.1038/s41467-021-20905-1

Trivedi, C. M., Zhu, W., Wang, Q., Jia, C., Kee, H. J., Li, L., Hannenhalli, S., & Epstein, J. A. (2010). Hopx and Hdac2 interact to modulate Gata4 acetylation and embryonic

cardiac myocyte proliferation. *Developmental Cell*, *19*(3). https://doi.org/10.1016/j.devcel.2010.08.012

Tucker, N. R., Chaffin, M., Fleming, S. J., Hall, A. W., Parsons, V. A., Bedi, K. C., Akkad, A. D., Herndon, C. N., Arduini, A., Papangeli, I., Roselli, C., Aguet, F., Choi, S. H., Ardlie, K. G., Babadi, M., Margulies, K. B., Stegmann, C. M., & Ellinor, P. T. (2020). Transcriptional and Cellular Diversity of the Human Heart. *Circulation*, *142*(5). https://doi.org/10.1161/CIRCULATIONAHA.119.045401

Varadi, K., Michelfelder, S., Korff, T., Hecker, M., Trepel, M., Katus, H. A., Kleinschmidt, J. A., & Müller, O. J. (2012). Novel random peptide libraries displayed on AAV serotype 9 for selection of endothelial cell-directed gene transfer vectors. *Gene Therapy*, *19*(8). https://doi.org/10.1038/gt.2011.143

Waddington, C. H. (1942). Canalization of development and the inheritance of acquired characters. *Nature*, *150*(3811). https://doi.org/10.1038/150563a0

Waddington, C. H. (2011). The epigenotype. Endeavour 1942; 1:18-20. *Reprinted in International Journal of Epidemiology*, *41*(1).

Webber, M., Jackson, S. P., Moon, J. C., & Captur, G. (2020). Myocardial Fibrosis in Heart Failure: Anti-Fibrotic Therapies and the Role of Cardiovascular Magnetic Resonance in Drug Trials. In *Cardiology and Therapy* (Vol. 9, Issue 2). https://doi.org/10.1007/s40119-020-00199-y

Weber, K. T. (2004). Fibrosis in hypertensive heart disease: Focus on cardiac fibroblasts. In *Journal of Hypertension* (Vol. 22, Issue 1). https://doi.org/10.1097/00004872-200401000-00011

Wenxin Kou, Yefei Shi, Bo Li, Yanxi Zeng, Ming Zhai, Shuangjie You, Qing Yu, Shiyu Gong, Jianhui Zhuang, Yifan Zhao, Weixia Jian, Yawei Xu, & Wenhui Peng. (2022). Endothelial TET2 Regulates Cardiac Remodeling by Modifying Endothelial-to-Mesenchymal Transition. *Biorxiv*. https://doi.org/doi.org/10.1101/2022.06.15.496224

Woodcock, E. A., & Matkovich, S. J. (2005). Cardiomyocytes structure, function and associated pathologies. In *International Journal of Biochemistry and Cell Biology* (Vol. 37, Issue 9). https://doi.org/10.1016/j.biocel.2005.04.011

World Health Organization (WHO). (2020). WHO reveals leading causes of death and disability worldwide: 2000-2019. *World Health Organization (WHO)*, *1*.

Wu, X., & Zhang, Y. (2017). TET-mediated active DNA demethylation: Mechanism, function and beyond. In *Nature Reviews Genetics* (Vol. 18, Issue 9). https://doi.org/10.1038/nrg.2017.33

Wynn, T. A. (2004). Fibrotic disease and the TH1/TH2 paradigm. In *Nature Reviews Immunology* (Vol. 4, Issue 8). https://doi.org/10.1038/nri1412

Xiao, J., Gao, R., Bei, Y., Zhou, Q., Zhou, Y., Zhang, H., Jin, M., Wei, S., Wang, K., Xu, X., Yao, W., Xu, D., Zhou, F., Jiang, J., Li, X., & Das, S. (2017). Circulating miR-30d Predicts Survival in Patients with Acute Heart Failure. *Cellular Physiology and Biochemistry*, *41*(3). https://doi.org/10.1159/000459899

Xu, X., Tan, X., Hulshoff, M., Hasenfuss, G., Zeisberg, M., & Zeisberg, E. (2017). 5042The role of long non coding RNA in gene-specific promoter methylation during cardiac fibrogenesis. *European Heart Journal*, *38*(suppl_1). https://doi.org/10.1093/eurheartj/ehx493.5042

Xu, X., Tan, X., Hulshoff, M. S., Wilhelmi, T., Zeisberg, M., & Zeisberg, E. M. (2016). Hypoxia-induced endothelial-mesenchymal transition is associated with RASAL1 promoter hypermethylation in human coronary endothelial cells. *FEBS Letters*, *590*(8). https://doi.org/10.1002/1873-3468.12158

Xu, X., Tan, X., Tampe, B., Nyamsuren, G., Liu, X., Maier, L. S., Sossalla, S., Kalluri, R., Zeisberg, M., Hasenfuss, G., & Zeisberg, E. M. (2015). Epigenetic balance of aberrant Rasal1 promoter methylation and hydroxymethylation regulates cardiac fibrosis. *Cardiovascular Research*, *105*(3). https://doi.org/10.1093/cvr/cvv015

Xu, X., Tan, X., Tampe, B., Wilhelmi, T., Hulshoff, M. S., Saito, S., Moser, T., Kalluri, R., Hasenfuss, G., Zeisberg, E. M., & Zeisberg, M. (2018). High-fidelity CRISPR/Cas9- based gene-specific hydroxymethylation rescues gene expression and attenuates renal fibrosis. *Nature Communications*, *9*(1). https://doi.org/10.1038/s41467-018-05766-5

Xu, X., Zong, K., Wang, X., Dou, D., Lv, P., Zhang, Z., & Li, H. (2021). miR-30d suppresses proliferation and invasiveness of pancreatic cancer by targeting the SOX4/PI3K-AKT axis and predicts poor outcome. *Cell Death and Disease*, *12*(4). https://doi.org/10.1038/s41419-021-03576-0

Yancy, C. W., Jessup, M., Bozkurt, B., Butler, J., Casey, D. E., Drazner, M. H., Fonarow, G. C., Geraci, S. A., Horwich, T., Januzzi, J. L., Johnson, M. R., Kasper, E. K., Levy, W.

C., Masoudi, F. A., McBride, P. E., McMurray, J. J. V., Mitchell, J. E., Peterson, P. N., Riegel, B., … Wilkoff, B. L. (2013). 2013 ACCF/AHA guideline for the management of heart failure: Executive summary: A report of the American college of cardiology foundation/American Heart Association task force on practice guidelines. *Circulation*, *128*(16). https://doi.org/10.1161/CIR.0b013e31829e8807

Yang, S. J., Yang, S. Y., Wang, D. D., Chen, X., Shen, H. Y., Zhang, X. H., Zhong, S. L., Tang, J. H., & Zhao, J. H. (2017). The miR-30 family: Versatile players in breast cancer. In *Tumor Biology* (Vol. 39, Issue 3). https://doi.org/10.1177/1010428317692204

Ye, Z., Li, J., Han, X., Hou, H., Chen, H., Zheng, X., Lu, J., Wang, L., Chen, W., Li, X., & Zhao, L. (2016). TET3 inhibits TGF-β1-induced epithelial-mesenchymal transition by demethylating miR-30d precursor gene in ovarian cancer cells. *Journal of Experimental and Clinical Cancer Research*, *35*(1). https://doi.org/10.1186/s13046-016-0350-y

Ye, Z., Zhao, L., Li, J., Chen, W., & Li, X. (2015). MiR-30d Blocked Transforming Growth Factor β1-Induced Epithelial-Mesenchymal Transition by Targeting Snail in Ovarian Cancer Cells. *International Journal of Gynecological Cancer*, *25*(9). https://doi.org/10.1097/IGC.0000000000000546

Zahid, K. R., Raza, U., Chen, J., Raj, U. J., & Gou, D. (2020). Pathobiology of pulmonary artery hypertension: Role of long non-coding RNAs. In *Cardiovascular Research* (Vol. 116, Issue 12). https://doi.org/10.1093/cvr/cvaa050

Zare, M., Bastami, M., Solali, S., & Alivand, M. R. (2018). Aberrant miRNA promoter methylation and EMT-involving miRNAs in breast cancer metastasis: Diagnosis and therapeutic implications. In *Journal of Cellular Physiology* (Vol. 233, Issue 5). https://doi.org/10.1002/jcp.26116

Zeisberg, E. M., Potenta, S. E., Sugimoto, H., Zeisberg, M., & Kalluri, R. (2008). Fibroblasts in kidney fibrosis emerge via endothelial-to-mesenchymal transition. *Journal of the American Society of Nephrology*, *19*(12). https://doi.org/10.1681/ASN.2008050513

Zeisberg, E. M., Potenta, S., Xie, L., Zeisberg, M., & Kalluri, R. (2007). Discovery of endothelial to mesenchymal transition as a source for carcinoma-associated fibroblasts. *Cancer Research*, *67*(21). https://doi.org/10.1158/0008-5472.CAN-07-3127

Zeisberg, E. M., Tarnavski, O., Zeisberg, M., Dorfman, A. L., McMullen, J. R., Gustafsson, E., Chandraker, A., Yuan, X., Pu, W. T., Roberts, A. B., Neilson, E. G., Sayegh, M. H., Izumo, S., & Kalluri, R. (2007). Endothelial-to-mesenchymal transition contributes to cardiac fibrosis. *Nature Medicine*, *13*(8). https://doi.org/10.1038/nm1613

Zhang, B., Niu, W., Dong, H. Y., Liu, M. L., Luo, Y., & Li, Z. C. (2018). Hypoxia induces endothelial-mesenchymal transition in pulmonary vascular remodeling. *International Journal of Molecular Medicine*, *42*(1). https://doi.org/10.3892/ijmm.2018.3584

Zhao, L., Mulligan, M. K., & Nowak, T. S. (2019). Substrain- and sex-dependent differences in stroke vulnerability in C57BL/6 mice. *Journal of Cerebral Blood Flow and Metabolism*, *39*(3). https://doi.org/10.1177/0271678X17746174

Zhong, W., Li, B., Xu, Y., Yang, P., Chen, R., Wang, Z., Shao, C., Song, J., & Yan, J. (2018). Hypermethylation of the Micro-RNA 145 Promoter Is the Key Regulator for NLRP3 Inflammasome-Induced Activation and Plaque Formation. *JACC: Basic to Translational Science*, *3*(5). https://doi.org/10.1016/j.jacbts.2018.06.004

Zhou, P., & Pu, W. T. (2016). Recounting cardiac cellular composition. In *Circulation Research* (Vol. 118, Issue 3). https://doi.org/10.1161/CIRCRESAHA.116.308139

Zhu, B., Chen, H., Zhang, X., Pan, Y., Jing, R., Shen, L., Wang, X., Ju, S., Jin, C., & Cong, H. (2018). Serum miR-30d as a novel biomarker for multiple myeloma and its antitumor role in U266 cells through the targeting of the MTDH/PI3K/Akt signaling pathway. *International Journal of Oncology*, *53*(5). https://doi.org/10.3892/ijo.2018.4532

Zhuang, J., Luan, P., Li, H., Wang, K., Zhang, P., Xu, Y., & Peng, W. (2017). The yin-yang dynamics of DNA methylation is the key regulator for smooth muscle cell phenotype switch and vascular remodeling. *Arteriosclerosis, Thrombosis, and Vascular Biology*, *37*(1). https://doi.org/10.1161/ATVBAHA.116.307923

Zuchi, C., Tritto, I., Carluccio, E., Mattei, C., Cattadori, G., & Ambrosio, G. (2020). Role of endothelial dysfunction in heart failure. In *Heart Failure Reviews* (Vol. 25, Issue 1). https://doi.org/10.1007/s10741-019-09881-3